UNIVERSITÀ DEGLI STUDI FIRENZE

DOTTORATO DI RICERCA IN SCIENZE CHIMICHE

CICLO XXXII

COORDINATORE Prof. PIERO BAGLIONI

ELECTRODEPOSITION AND CHARACTERIZATION OF THIN FILMS

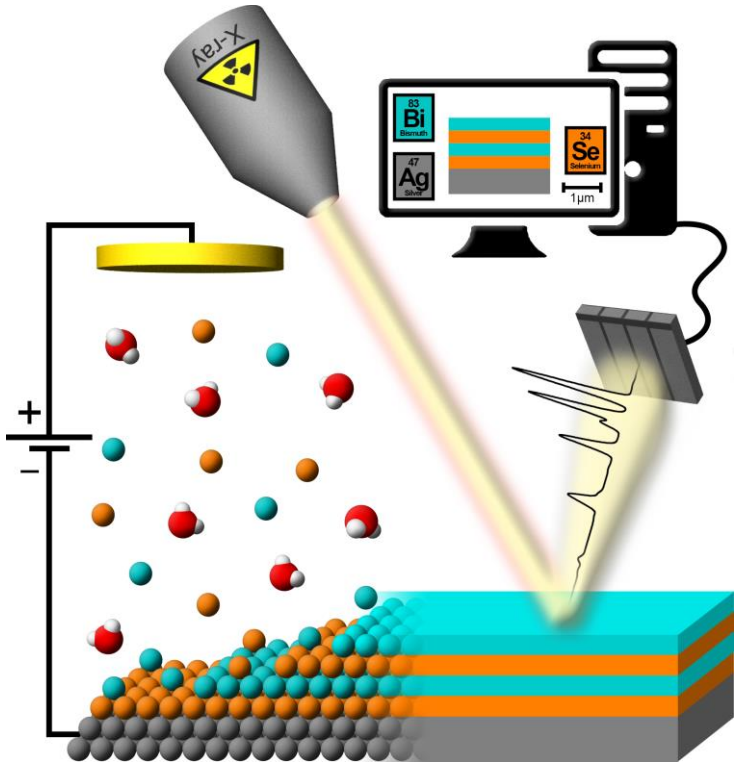

Dottorando
Dr. Walter Giurlani

Tutore
Prof. Massimo Innocenti

Co-Tutore
Dr. Alessandro Lavacchi

UNIVERSITÀ
DEGLI STUDI
FIRENZE

DOTTORATO DI RICERCA IN SCIENZE CHIMICHE

CICLO XXXII

COORDINATORE Prof. PIERO BAGLIONI

ELECTRODEPOSITION AND CHARACTERIZATION OF THIN FILMS

Settore Scientifico Disciplinare CHIM/01

Dottorando
Dr. Walter Giurlani

_____
(firma)

Tutore
Prof. Massimo Innocenti

_____
(firma)

Co-Tutore
Dr. Alessandro Lavacchi

_____
(firma)

Coordinatore
Prof. Piero Baglioni

_____
(firma)

Anni 2016/2019

Science is nothing but a rigorous game made of wonder and imagination.

Table of Contents

Preface

Abstract

During this PhD thesis I researched the conditions to obtain a controlled electrodeposition of bismuth metal and bismuth selenide and the standardless determination of the thickness of electrodeposited thin films by means of a quantification method based on Monte Carlo simulations.

The first part of this thesis was dedicated to the development of a new quantification method for the thickness determination of electroplated samples since the high variability of alloys makes impossible to use specific standards with a consequent lowering of the accuracy. The specimens were prepared with materials and features that made this study focused on the application in the electroplating sector. For this reason, films of varying thicknesses of nickel, palladium and gold have been deposited on copper and brass substrates. The study was conducted using EDS and XRF techniques and the results were compared with measurements of weight, SEM and XRF (current quantification method). Certified samples were also used as a comparison. The proposed method consists in constructing a calibration curve using simulated standards obtained from Monte Carlo algorithm in which the single electrons, or photons, interact with the substrate. The intensities are then normalized with respect to the pure elements (the only required standards to be measured) to minimize possible instrumental deviations; the calibration curve is used to derive the thickness of the samples. Taking into account that the current XRF quantification technique predicts an error of about 5 %, the results were encouraging for both techniques. In fact, a deviation from the expected values of about 9 % was obtained with

EDS using DTSA-II software (consistent with results obtained with measured standards) while one of only about 4 % was obtained with XRF using XMI-MSIM software. The two different techniques are complementary and allow to analyse very different ranges of thicknesses. Beyond the accuracy, this procedure does not require standards of known thickness: therefore, its advantages consist in being very low-cost and it would allow to virtually analyse any type of coating having only available bulk samples of the pure elements to be identified.

Regarding the electrodeposition processes, I have investigated the conditions for bismuth and bismuth selenide deposition since these materials have numerous properties that make them attractive for their use in technological devices. Currently, the films of these materials are obtained through vapour phase techniques to have good control over the deposition but the use of techniques in liquid phase, at ambient temperature and pressure, could considerably reduce the production costs. I found the conditions for an underpotential deposition to control the deposition of monolayer fractions on monocrystalline silver electrode. In this way both single layer and multilayer samples of bismuth and bismuth selenide were prepared. In addition to synthesise these compounds I tried to measure their thickness with the previously developed standardless method to obtain a better characterization of the deposits.

Scientific production

Published Papers

- Giurlani, W.; Innocenti, M.; Lavacchi, A. X-ray Microanalysis of Precious Metal Thin Films: Thickness and Composition Determination. *Coatings* **2018**, *8*, 84, doi:10.3390/coatings8020084.
- Giurlani, W.; Giaccherini, A.; Salvietti, E.; Passaponti, M.; Comparini, A.; Morandi, V.; Liscio, F.; Cavallini, M.; Innocenti, M. Selective Electrodesorption Based Atomic Layer Deposition (SEBALD) of Bismuth under morphological control. *Electrochem. Soc. Interface* **2018**, *27*, 77-81, doi:10.1149/2.F08182if.
- Giurlani, W.; Zangari, G.; Gambinossi, F.; Passaponti, M.; Salvietti, E.; Di Benedetto, F.; Caporali, S.; Innocenti, M. Electroplating for Decorative Applications: Recent Trends in Research and Development. *Coatings* **2018**, *8*, 260, doi:10.3390/coatings8080260.
- Giurlani, W.; Giaccherini, A.; Calisi, N.; Zangari, G.; Salvietti, E.; Passaponti, M.; Caporali, S.; Innocenti, M. Investigations on the Electrochemical Atomic Layer Growth of Bi_2Se_3 and the Surface Limited Deposition of Bismuth at Silver Electrode. *Materials (Basel).* **2018**, *11*, 1426, doi:10.3390/ma11081426.
- Giurlani, W.; Berretti, E.; Innocenti, M.; Lavacchi, A. Coating Thickness Determination Using X-ray Fluorescence Spectroscopy: Monte Carlo Simulations as an Alternative to the Use of Standards. *Coatings* **2019**, *9*, 79, doi:10.3390/coatings9020079.
- Innocenti, M.; Giurlani, W.; Passaponti, M.; De Luca, A.; Salvietti, E. Electrodeposition and innovative characterization of precious metal

alloys for the Galvanic and Jewel industry. *Substantia* **2019**, *3*, 29 – 37, doi:10.13128/Substantia-602.

- Giurlani, W.; Dell'Aquila, V.; Vizza, M.; Calisi, N.; Lavacchi, A.; Irrera, A.; Lo Faro, M. J.; Leonardi, A. A.; Morganti, D.; Innocenti, M, Electrodeposition of nanoparticles and continuous film of CdSe on n-Si(100). *Nanomaterials* **2019**, *9*, 1504, doi:10.3390/nano9101504.
- Giurlani, W.; Cavallini, M.; Picca, R. A.; Cioffi, N.; Passaponti, M.; Fontanesi, C.; Lavacchi, A.; Innocenti, M. Underpotential-Assisted Electrodeposition of Highly Crystalline and Smooth Thin Film of Bismuth. *ChemElectroChem* **2020**, *7*, 299–305, doi:10.1002/celc.201901678.

Papers in Preparation

- Giurlani, W.; Berretti, E.; Lavacchi, A.; Innocenti, M. Film Thickness Determination of Multilayer Coatings using XRF Spectroscopy through a Standardless Monte Carlo Approach.

Papers not Included in this Thesis

The following papers are the results of collaborations and lateral studies that involved me over these three years; my contribution in them has been more or less considerable but always in the field of electrodeposition and characterization of thin films. I decided not to include them in this manuscript because they deviate from the red wire that links this work and the storytelling that I decided to impress to it.

- Giurlani, W.; Gambinossi, F.; Salvietti, E.; Passaponti, M.; Innocenti,

M. Color Measurements In Electroplating Industry: Implications For Product Quality Control. *ECS Trans.* **2017**, *80*, 757–766, doi:10.1149/08010.0757ecst.

- Salvietti, E.; Giurlani, W.; Foresti, M.; Passaponti, M.; Fabbri, L.; Marcantelli, P.; Caporali, S.; Martinuzzi, S.; Calisi, N.; Pedio, M.; Innocenti, M. On the Contrasting Effect Exerted by a Thin Layer of CdS against the Passivation of Silver Electrodes Coated with Thiols. *Surfaces* **2018**, *1*, 29–42, doi:10.3390/surfaces1010004.
- Vizza, M.; Giaccherini, A.; Giurlani, W.; Passaponti, M.; Cioffi, N.; Picca, R. A.; De Luca, A.; Fabbri, L.; Lavacchi, A.; Gambinossi, F:; Piciollo, E.; Salvietti, E.; Innocenti, M. Successes and Issues in the Growth of Moad and MoSe2 on Ag(111) by the E-ALD Method. *Metals (Basel).* **2019**, *9*, 122, doi:10.3390/met9020122.
- Passaponti, M.; Rosi, L.; Savastano, M.; Giurlani, W.; Miller, H. A.; Lavacchi, A.; Filippi, J.; Zangari, G.; Vizza, F.; Innocenti, M. Recycling of waste automobile tires: Transforming char in oxygen reduction reaction catalysts for alkaline fuel cells. *J. Power Sources* **2019**, *427*, 85–90, doi:10.1016/j.jpowsour.2019.04.067.
- Fontanesi, C.; Como, E. Da; Vanossi, D.; Montecchi, M.; Cannio, M.; Mondal, P. C.; Giurlani, W.; Innocenti, M.; Pasquali, L. Redox-Active Ferrocene grafted on H-Terminated Si(111): Electrochemical Characterization of the Charge Transport Mechanism and Dynamics. *Sci. Rep.* **2019**, *9*, 8735, doi:10.1038/s41598-019-45448-w.
- Giurlani, W.; Marcantelli, P.; Benelli, F.; Bottacci, D.; Gambinossi, F.; Passaponti, M.; De Luca, A.; Salvietti, E.; Innocenti, M. Corrosion Resistance Test of Electroplated Gold and Palladium Using Fast Electrochemical Analysis. **2019**, 9, 405, doi:10.3390/ciwc2019-06159.

- Berretti, E.; Giaccherini, A.; Montegrossi, G.; D'Acapito, F.; Di Benedetto, F.; Zafferoni, C.; Puri, A.; Lepore, G. O.; Miller, H.; Giurlani, W.; Innocenti, M.; Vizza, F.; Lavacchi, A. In-situ Quantification of Nanoparticles Oxidation: A Fixed Energy X-ray Absorption Approach. *Catalysts* **2019**, *9*, 659, doi:10.3390/catal9080659.
- Innocenti, M.; Passaponti, M.; Giurlani, W.; Giacomino, A.; Pasquali, L.; Giovanardi, R.; Fontanesi, C. Spin dependent electrochemistry: Focus on chiral vs achiral charge transmission through 2D SAMs adsorbed on gold. *J. Electroanal. Chem.* **2020**, *856*, 113705, doi:10.1016/j.jelechem.2019.113705.
- Innocenti, M.; Giaccherini, A.; Chelli, R.; Martinuzzi, S.; Giurlani, W.; Passaponti, M.; Lavacchi, A.; Fontanesi, C. Modelling of the Elementary Steps Involved in the Aluminum Electrochemical Deposition from Ionic Liquid Based Solution: The BMImCl / AlCl 3 System. *J. Electrochem. Soc.* **2020**, *167*, 013525, doi:10.1149/2.0252001JES.

List of Abbreviation

AFM	Atomic force microscopy
BSE	Backscattered electron
CV	Cyclic voltammetry
CPL	Cross polarized light
E-ALD	Electrochemical atomic layer deposition
EDS	Energy dispersive X-ray spectroscopy
EPMA	Electron probe microanalysis
FIB	Focussed ion beam
FP	Fundamental parameter
LSV	Linear sweep voltammetry
MC	Monte Carlo
ML	Monolayer
PR	Peak ratio
PVD	Physical vapour deposition
QL	Quintuple layer
SAM	Self-assembled monolayer
SEBALD	Selective electrodesorption-based atomic layer deposition
SEM	Scanning electron microscopy
SIMS	Secondary ion mass spectrometry
TI	Topological insulator
UPD	Underpotential deposition
WDS	Wavelength dispersive X-ray spectroscopy
XPS	X-ray photoemission spectroscopy

XRD	X-ray diffraction spectroscopy
XRF	X-ray fluorescence spectroscopy

1 Introduction

The use of films has become an ubiquitous practice in any industrial sector. Coatings are widespread used to obtain a synergistic action between the characteristics of the substrate and the covering material to improve the physical, chemical and aesthetic properties and to lower the costs of the final product. The composition of the films could be extremely vast: dielectrics (organic, such as polymers and self-assembled monolayers (SAM), or inorganic, like metal oxides), semiconductors and metals are all used in the form of films, obtaining a composite material with combined characteristics. Thin films are a sub-category defined by the IUPAC gold book as *"a film whose thickness is of the order of a characteristic scale or smaller"* [1,2]. This definition is quite generic, and a film can be thin or thick depending on the system under analysis or the analytical method. For example, although it may seem unusual, the Earth's crust, between 10 km and 70 km thick, is nothing but a thin film compared to the entire planet Earth, which has an average radius of 6370 km. To give an example more inherent to chemistry and materials science, a film can be thick compared to the electron mean free path, but thin with respect to the optical wavelength.

In this PhD thesis I focused my efforts on two main topics related to electrodeposition processes and to the determination of the thickness of electrodeposited thin films:

- Determination of film thickness using energy dispersive X-ray spectroscopy (EDS) and X-ray fluorescence spectroscopy (XRF) through a standardless method supported by Monte Carlo (MC) simulations.

- Bismuth and bismuth selenide thin film electrodeposition on a monocrystalline silver substrate.

Both topics have a high industrial and technological impact and their development has been evolved in parallel.

As far as electrodeposition is concerned, the thinnest film that can be deposited coincides with an atomic monolayer (ML), while the thicker layers could reach hundreds of microns in electroforming. In this work, I focused on the electrodeposition of bismuth and bismuth selenide films on a monocrystalline silver electrode. The films that I have deposited range from a single ML to a few tens of nanometres in thickness and for this reason they have been defined as thin. These composites do not have many large-scale applications yet but due to their peculiar chemico-physical properties they are excellent candidates for the development of new technologies and next-generation devices [3].

On the other hand, in everyday language the term "electrodeposition" is strongly linked to the galvanic industry. In 2015 this sector represented around 37 % of the total market share in the metal finishing business. The most commonly used galvanically deposited metals are zinc and zinc alloys (about 15 %), followed by nickel, copper, chromium, tin and precious metals (together about 22 %) [4]. According to a recent study published by Future Market Insights, the global electroplating market is expected to increase at an annual growth rate of 3.7 % in the 2016-2026 period, forecasting revenues of over US$ 21 billion within the end of 2026 [5]. A significant expansion will take place in the Asia-Pacific region, registering an annual growth rate of 4.6 % in the expected period. Anyway, the market for mature electroplating industries in North America and Western Europe will maintain the leadership.

For this application the determination of the thickness is fundamental both for the physico-chemical properties of the final product as well as the production costs. For this reason, an integral part of my research was based on the development of an innovative analytical approach for determining the thickness of metal films. The two main techniques I used for this scope were EDS and XRF. The first one allows to analyse an interaction volume ranging from few nanometres to hundreds [6,7], while the second one is used to measure thicknesses in the order of microns [8,9].

In addition to synthesise technologically relevant compounds and developing an innovative analysis technique for the galvanic sector, I tried to combine these results to obtain a better characterization of my deposits. The workflow scheme of this thesis is represented in Figure 1.1.

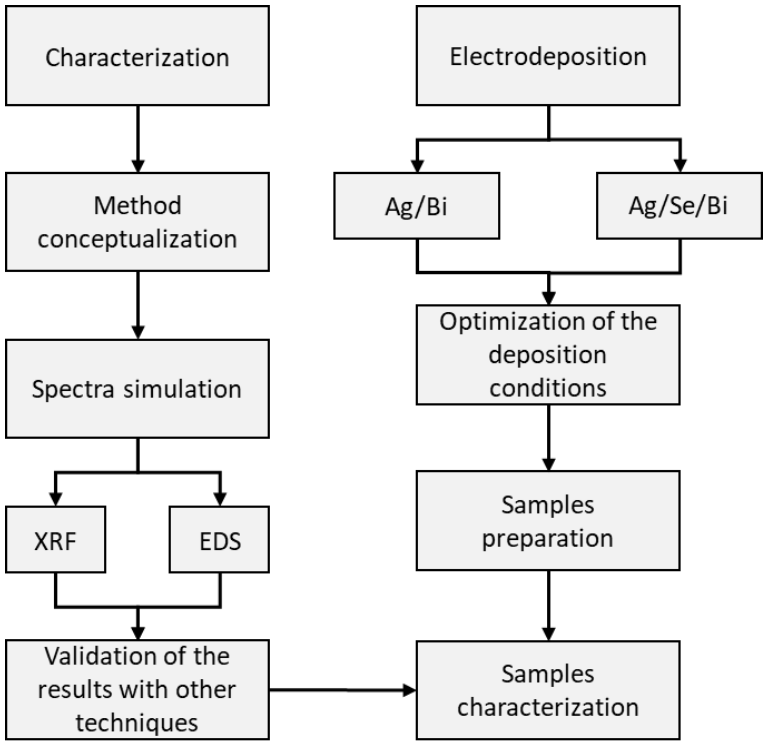

Figure 1.1 – Workflow scheme of this thesis.

1.1 Thickness Determination of Thin Films

The measurement of the thickness in composite materials is mandatory both to obtain the right characteristics in the final artefact as well as to keep the costs under control. Do consider, for example, a costume jewellery object made of brass and covered with gold: if the coating is too thin it will spoil rapidly due to mechanical abrasion and, because of diffusion in the alloy and not uniform deposition, it will undergo to corrosion more easily than expected; moreover, also the colour could be influenced if the film is really thin, resulting in a discrepancy between what the manufacturer guarantees and what it actually sells, with a consequent loss of money. On the other side, if

the coating is thicker than established the cost rises up because of the waste of precious material. Furthermore, if the thickness is too thick, due to tensile stress between the two materials, even the exfoliation of the top layer could occur.

According to the type, the composition and the thickness itself of the film and the substrate, various techniques could be employed to investigate the size of the layers, but all the methods could be classified in two different categories: destructive and non-destructive techniques.

A destructive technique is a method that alters the sample, generally by scratching it, at a macroscopic or microscopic level; therefore, the analysed piece cannot be put on the market and it must be destroyed instead. This means that we have to be sure about the conformity with sale of the unmeasured objects. On the other hand, a non-destructive technique permits to measure the sample without damaging it but, generally, if it belongs to the group of indirect measurements, requires some assumption and calculation to be performed to obtain a numerical value of the thickness.

The most common instrument used by industries is the XRF since it is fast, non-destructive and relatively simple to use, making it perfect for the quality control of the products. Commercial instruments can measure easily the thickness of almost every material (with some restriction for lighter elements), whether conductive or not, in the range from 10 nm to 100 μm [8,9]; nevertheless, depending on the materials under investigation and the instrumental settings, the limits of measurement could be extended from less than 1 nm [10] to a few centimetres [11]. The output of the instrument is a spectrum in which the position of the peaks corresponds to the spectroscopic emission of the elements present in the sample while the intensity is correlated

to the sample composition in the volume of interaction of the incident beam. No information about the thickness can be extracted *a priori* from the spectra since the sample is interpreted as homogeneous. Only with the right assumptions on the nature of the sample and the use of an adequate calibration curve, the thickness information can be deconvoluted: this complication could bring to high uncertainties or even wrong results. Other non-destructive techniques, more commonly used for research purposes, are ellipsometry [12] and X-ray reflectivity [13,14] that can detect thicknesses from tens of nanometres to some micrometres. Although it is not their main use also EDS [15,16] and X-ray Photoemission Spectroscopy (XPS) [17,18] could be employed to determinate the thickness information.

Conversely, the scanning electron microscopy (SEM) is without any doubt the most common destructive technique used for the determination of films thickness. The quantification procedure is quite straightforward: the sample is cut in half, polished and the cross section is analysed. By taking a photo of the cross sample with the appropriate magnification, it is possible to observe directly the coatings and to measure them using a ruler. The resolution of a SEM could be high enough to measure even a few nanometres, while the upper limit depends on the physical construction of the instrument, but typically is more than few micrometres. The main source of errors often comes from samples preparation. In principle SEM can analyse only conductive materials which are stable in high vacuum, but it is possible to measure also non-conductive materials if they are covered with carbon or gold. SEM is extremely common in research facilities and private laboratories of analysis but not so diffused in the industries that prefer to rely on external laboratories only in case of necessity, for examples in the presence of a dispute on the results provided by the XRF. This lack is due only in a small part to

the higher cost of the instrumentation, because the main limitation in the use of the SEM is the preparation of the sample before the analysis. In fact, in most of the cases, a protective layer must be applied on the sample before the cutting (which must be slowly performed under liquid cooling to prevent deformations) to avoid the detachment and the spread of the film in the following steps. Then, after the cutting procedure, the sample must be incorporated into a resin to make it have a flat surface without any tilts and to simplify the polishing procedures; moreover, it must be polished with abrasive pastes from coarse to fine dimension (in the order of the film thickness) to eliminate any scratches and to obtain a clear separation between the layers. The entire process can last from several hours to even some days to obtain a suitable surface, and these times are not compatible with industrial ones. A cheaper alternative consists in the Calo tester, known also as crater grinding method [19,20] which is also a normalized method [21]. It consists in placing a rotating steel ball on the sample with an abrasive liquid paste; a hole is dug due to abrasion revealing all the underlying layers in the range 0.1 – 50 μm. Depending to the ball size, the abrasion angle will be different, so that also small layers in thickness can be revealed using an optical microscope. This method is very robust but suffers of two main disadvantages: it is destructive (the hole is easily visible by eye) and there must be differences in colour between the materials of the different layers. Other methods for the determination of the thickness of coatings are profilometer [22] (or atomic force microscopy (AFM) profilometry [23]) employing a mask to leave the substrate partially uncovered or Secondary ion mass spectrometry (SIMS) [24,25] and XPS sputtering [26,27] but all these method are destructive, the results are not simple to interpret and unpractical from an industrial point of view.

For all these reasons, in this thesis I have explored the possibility to use a new approach for the quantification of the thickness of thin films. In particular I carried out an exploratory study to evaluate the possibility of obtaining better results, or at a lower cost, compared to the state of the art, but using the same tools and data collected and therefore a more effective data analysis, with a particular focus to the coatings of electroplating and fashion industry. The measurements were carried out via EDS and XRF, whose analytical validation is already established, using MC simulations to correlate the measure intensities of the samples with the thickness of the layers.

1.2 Bismuth and Bismuth Selenide

Over time bismuth, in the metal form, is increasingly being studied by the scientific community, which takes it in special consideration because of its peculiar chemical and physico-chemical properties. The applications of bismuth include many technological devices thanks to its several features: magnetoresistance [28–32], superconductivity [33], thermoelectrical [34,35], optical and electronic anisotropy [36–38], quantum effect [39–41], valleytronics and spintronics material [42,43], but even application in catalysis [44] and heavy metals analysis [45–47].

The preparation of bismuth thin films generally involves low pressure vapour phase depositions [48–52] and electrodeposition from solution on various substrates [53–56]. Electrodeposition is usually performed at room conditions, which makes it cheaper with respect to other techniques and more attractive for large-scale production; moreover, it can provide highly ordered and crystalline deposits [57–60]. Unfortunately, in the case of Bi, only few

works manage to obtain a reproducible deposit through electrochemical methods [61–63] but still obtaining an island-like or a thick film deposit instead of a continuous and uniform one, while most electronic applications require smooth deposits to maximise the charge transfers and the other performances.

On the other hand, also bismuth and antimony chalcogenides (where the chalcogenide is selenium or tellurium) exhibit excellent thermoelectric properties, achieving thermoelectric figure of merit (ZT) values of about 1 [64]. These materials commonly crystallise in a rhombohedral structure and exhibit semiconducting behaviour (band gap ~0.3 eV). Beyond thermoelectric behaviour, these materials show an insulating response in the bulk form while exhibiting metallic conductivity at grain boundaries or surfaces; in particular, surface states, are protected via time reversal symmetry, such that electron scattering does not occur. Recently, it has also been shown that the electrochemical growth of Bi_2Se_3 at low temperatures results in the formation of an orthorhombic structure with a higher band gap of about 1.1 eV [65,66]. Interestingly, in the context of light absorbers and solar cells, the same behaviour was also obtained by growing Bi_2Se_3 via the successive ionic layer adsorption and reaction (SILAR) method [67].

Bismuth selenide [68–71], as well as ultra-thin film of bismuth metal [72–74] exhibit topological insulator (TI) behaviour. A TI [3,75] is a material that behaves as an insulator in its interior but whose surface contains conducting states, meaning that electrons can only move along the surface of the material. However, having a conducting surface is not a unique feature to topological insulators, since ordinary band insulators can also support conductive surface states. What is special about topological insulators is that their surface states

are symmetry-protected by particle number conservation and time-reversal symmetry. The layered structure of the rhombohedral crystal of bismuth selenide, with van der Waals interactions between the layers, encourages synthetic opportunities for the direct growth of layered structures or two-dimensional material. The reference crystalline structure for bismuth selenide is the tetradymite mineral (Bi_2Te_2S) with a layered structure with Se1-Bi-Se2-Bi-Se1 units (Figure 1.2), commonly referred to as quintuple layers (QL) [76,77], that are bonded together by van der Waals forces. Each QL is chemically stable, leading to a van der Waals gap between QLs. This weak interlayer bonding allows TI layers to easily be exfoliated from bulk crystals. In a previous study, Zhang obtained relevant results in an acidic medium using a polycrystalline Pt electrode [78]; unfortunately, in the reported conditions a partial bulk deposition occurs, providing some uncontrolled 3D structures.

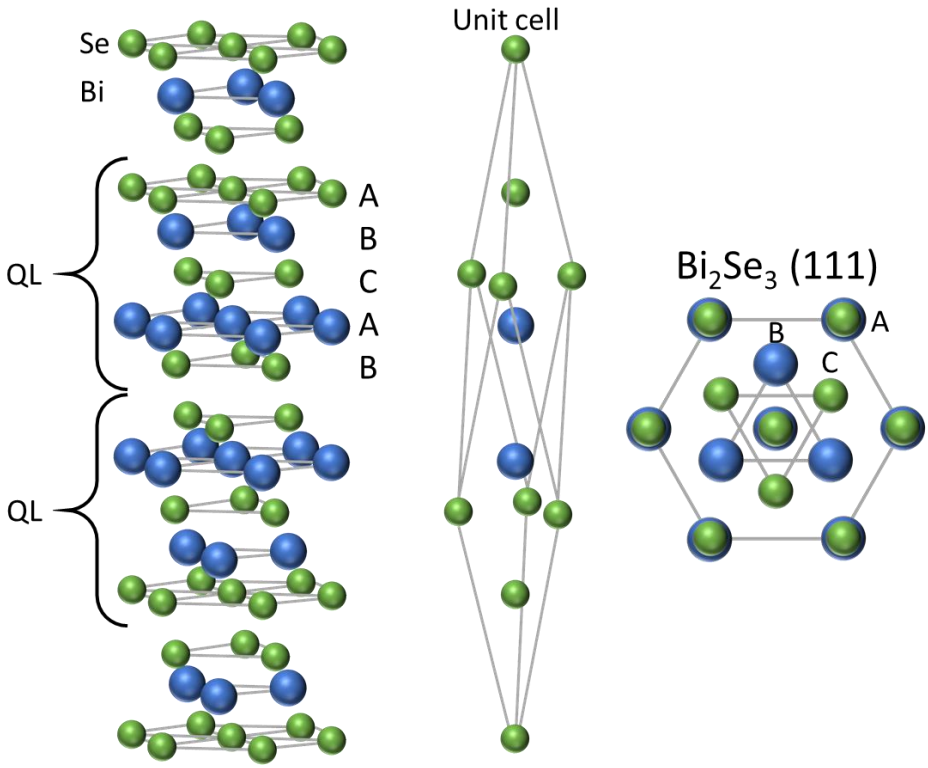

Figure 1.2 – Representation of the crystal structure of Bi_2Se_3 and the representation of QLs.

Both in the case of Bi and Bi_2Se_3 I investigated the possibility of exploiting the underpotential deposition (UPD) to overcome the drawbacks of low-pressure techniques and performed a low-cost electrodeposition with high control on both the amount as well as the morphology of the deposit. The UPD is limited by the surface and the deposit results smoother than that obtained through other approaches. Therefore, the UPD method allows to finely control the deposition and permits a crystalline growth minimizing the quantity of defects.

Initially, I investigated the behaviour of bismuth deposited directly on silver and on a ML of selenium on silver to form a single layer of the metal or

the chalcogenide on the silver substrate. Then I tried to increase the thickness of the deposit to obtain a 3D film. The multilayer deposition was performed by keeping in mind the requirements of highly ordered structure with defined composition. The preparation of multilayer Bi_2Se_3 film, was performed exploiting the electrochemical atomic layer deposition (E-ALD) [79–82] performing an alternate UPD of bismuth and selenium, as well as a charge controlled alternate deposition of the precursors. In the case of bare bismuth film, I initially explored the selective electrodesorption-based atomic layer deposition (SEBALD) technique [79,83–85] which consists in the discriminatory stripping of one element from a previously formed E-ALD deposit, Bi_2Se_3 in my case. In this way it is possible, in principle, to obtain a multilayer film of just one element but without undergoing the disorder of a bulk deposition performed by applying an overpotential with respect to the Nernst potential. Then I also evaluated the possibility to obtain the same results using a charge-controlled deposition of bismuth at various overpotentials on a previously deposited layer of UPD Bi.

2 Theory and Methods

2.1 Techniques for Innovative Thickness Analysis

2.1.1 Energy Dispersive X-ray Spectroscopy

The electron probe microanalysis (EPMA) was first developed in 1951 by Casting [86]. EPMA permits to analyse the composition of homogeneous materials in a region of few microns from the surface. The EPMA can be conducted using two different approaches: wavelength dispersive X-ray spectroscopy (WDS) [87] or energy dispersive X-ray spectroscopy (EDS) [88–92]. WDS is generally considered an excellent method for microanalysis because is more sensitive and has a higher resolution than EDS but it is more expensive and needs a dedicated device. EDS, on the other hand, can be conducted by simply coupling a detector to SEM, a widespread instrument in the academic and industrial sphere, especially since the recent spread of inexpensive benchtop instrument.

The investigation of supported films with microanalysis could open a new way of making coating analysis, even at industrial level. EDS is a technique that interpret every sample as homogeneous, since the output information is a spectrum. For this reason, there is no direct information on the thicknesses but the intensity of the peaks in the spectra are function of thickness. EDS is an attractive candidate because it enables fast, quantitative [93,94], non-destructive [95] and inexpensive analysis with the additional benefit of having a lateral resolution in the micron range [96]. In addition to that, the probe (electrons) is not very penetrating and for this reason it is possible (by adjusting the beam energy) to analyse ultra-films or only the top layer to obtain its composition [97–101].

The instrumentation consists in an EDS detector coupled with a SEM and can be schematically described as follows: an emitter consisting of a tungsten, or other material, filament heated above 1000 °C by means of the Joule effect, acts as source of electrons due to the thermoionic effect. The electron beam generated is accelerated by a potential difference of 0.3 - 30 kV and then passes through an electromagnetic collimator to be deflected, to generate the scan, and finally collimated towards the plate containing the sample under examination.

The electron bombardment excites the atoms in the sample knocking out the electrons from of the inner shells. Such state is unstable, and the resulting electron hole is immediately filled by a higher-energy electron from a higher atomic orbital. The energy difference is released in the form of an X-ray quantum. The resulting X-ray radiation is characteristic of the transition and the atom. For a single element, different transitions are allowed, depending on which shell the higher-energy electron comes from and which shell the hole has to be filled in. This results in X-ray quanta, which are marked with Kα, Kβ, Lα, etc. The energy of an X-ray lines (position of the lines in the spectrum) is an indicator of which element is under investigation. The intensity of the line depends on the concentration of the element within the sample. Furthermore, the electrons, slowing down in the electric field of the atomic nuclei, generate an X-ray braking radiation, called bremsstrahlung, which constitutes the continuous background of the EDS spectrum.

The EDS detector exploits the energy interaction between X-rays and a suitable material, generally represented by a silicon single crystal doped with lithium, coated at both ends with a gold conductive layer, at a temperature of -192 °C with liquid nitrogen. Other variants are the silicon drift detector and

high purity germanium detectors. The detector measures the energy of each incoming X-ray photon. When an X-ray photon is absorbed in the sensitive area of the detector, then electron-hole pairs are produced whose number is proportional to the energy of the photon, this cause the production of an electric current, which is then sensitively amplified. Statistical effects in the detector and electronic noise broaden the natural line width, for this reason the typical energy resolution of an EDS detector is 120-140 eV. The entire apparatus is kept under vacuum, approximately 10^{-4} - 10^{-6} mbar, generated by an ion pump, to increase the free average path of the electrons and avoid diffusion phenomena due to air-electron interactions.

The quantity commonly used in microanalysis is the K-ratio. The K-ratio *K* of the characteristic peak of the element *i* is defined as the ratio between the intensity of that peak measured in the unknown sample I^{unk} and in a standard with known composition I^{std}, ideally the pure element (Equation (2.1)). To eliminate as many physical and instrumental factors as possible, both the sample and the standard must be measured in the same operating conditions and with the same instrument.

$$K_i = \left(\frac{I_i^{unk}}{I_i^{std}}\right) \tag{2.1}$$

In first approximation the K-ratios are proportional to the mass concentration *C* of the analyte (Equation (2.2)).

$$C_i^{unk} \approx K_i C_i^{std} \tag{2.2}$$

For an appropriate quantification some phenomena and contributions must be taken into account: (i) the backscattering and stopping power of elements with different atomic numbers (Z); (ii) the self-absorption of the sample (A); (iii) the secondary fluorescence (F). For these reasons a correction

must be made. There are many correction algorithms: the most widespread and historical one is ZAF (Equation (2.3)). The correction involves an iterative process to obtain the optimal Z, A and F parameter and the real concentration of the analyte.

$$C_i^{unk} = K_i \frac{ZAF_i^{unk}}{ZAF_i^{std}} C_i^{std} \tag{2.3}$$

2.1.2 X-ray Fluorescence Spectroscopy

XRF is an analysis tool widely used for the elemental analysis and chemical analysis of materials. When materials are exposed to high-energy X-rays, ionization of their component atoms may take place exciting them and, like in the case of electrons excitement, the emitted photons are detected for analysis. Due to incident high-energy X-rays the inner shell (K, L, M, etc.) transition phenomena occurs within 100 fs producing a characteristic fluorescence radiation. Ionization consists of the ejection of one or more electrons from the atom and may occur if the atom is exposed to radiation with energy greater than its ionization energy. X-rays and gamma rays can be energetic enough to eject tightly held electrons from the inner orbitals of the atom. The removal of an electron in this way makes the electronic structure of the atom unstable, and electrons in higher orbitals "fall" into the lower orbital to fill the holes left behind. In falling, energy is released in the form of photons with an amount equal to the energy difference between the two orbitals involved. Thus, materials emit radiations of the characteristic energies of the present atoms. A variety of samples in different states, such as solids, powders, and liquids, can be analysed using this technique. It can also be used to measure the composition, thickness of coating and layers.

The photons that excite the sample are emitted by an X-ray tube. Inside the tube, under high vacuum, there is a filament heated up by an electric current to emit electrons. A high potential difference, 20 – 100 kV, is applied across the filament and an anode to accelerate the electrons. When the electrons hit the anode they are decelerated, which causes the emission of X-rays, called bremsstrahlung radiation. The energy and intensity of the emitted X-rays is uniform, and it is often called the continuum. A fraction of the electrons that hit the atoms of the anode will expel electrons from it, causing emission of characteristic radiation. The energy of this radiation is determined by the element in the anode. The X-rays emitted by the anode can leave the tube through a beryllium window. The energy of the X-rays emitted cannot be higher than the applied voltage and the X-rays with very low energies are not capable of passing through the Be window. The continuum of an X-ray tube depends on the applied accelerating potential, the electric current and on the material used for the anode. Then the emitted photons pass through a filter to limit the characteristics emission of the anode and in a collimator before hitting the sample. The characteristic photons of the sample are collected by a detector that uses the same working principle of EDS. Both the source photons as well the emitted ones could pass through an analysing crystal that act as monochromator differentiating between energy dispersive XRF without analysing crystal; wavelength dispersive XRF, in which the emitted photons are selected with a monochromator; monochromatic wavelength dispersive XRF, in which two optics are used: one for the source and one for the emitted photons. For reasons of cost and ease of use, energy dispersion instruments are the most used.

Deriving a coating's thickness from the X-ray spectrum requires an experimental calibration curve that employs standards; however, due to the

large dependence of the X-ray spectrum on the nature of the coating and the substrate, standards are not always available. The variability of thickness, layer composition, multilayer architectures, and substrate chemical nature create difficulties in producing certified standards. This issue is critical in industrial applications, indeed the determination of precious metal coatings in the fashion industry is a major one where the products are made with many coatings and substrates, with extreme variability in the system.

Nowadays, the most common approach is the use of the fundamental parameter (FP) method [8,102–104]. FP relies on theoretical equations that consider the composition and thickness of the sample to evaluate the XRF intensity. Practically, the FP method is combined with a few empirical standards to correct unpredicted deviations due to matrix effects [105,106]. With the FP method, it is possible to determine the film thickness of single and even multilayer samples if the structure and the composition are known exactly; nevertheless, the error correlated to the measurement is significant. Typical accuracy for single layer samples is ±5 %, while for multiple-layer samples this value grows to ±10 % for the upper layer and ±37 % for the first underlayer [107–109] due to inaccuracy in the method for complex samples. Additionally, very often the thickness and composition of the underlying layers in multilayer architectures are not exactly known and they are introduced in the measurement software using an initial estimation [110].

2.1.3 The Attenuation Length

In physics, the attenuation length or absorption length ε is defined as the distance into a material where the beam flux (transmittance T) has dropped to 1/e, or about 63 %, of its incident flux.

$$T = \frac{I_x}{I_0} = e^{-\frac{x}{\varepsilon}} \tag{2.4}$$

In general, ε is material and energy dependent. The attenuation length is an important parameter to consider evaluating which are the possible thickness that could be measured. Another quantity typically used is the attenuation coefficient (or absorption coefficient) is simply the inverse of the absorption length.

$$\mu = \frac{1}{\varepsilon} \tag{2.5}$$

The mass attenuation coefficient, μ/ρ is a basic quantity used in calculations of the penetration and the energy deposition by photons (X-ray, γ-ray, bremsstrahlung) in biological, shielding and other materials. A narrow beam of monoenergetic photons with an incident intensity I_0, penetrating a layer of material with mass thickness x and density ρ, emerges with intensity I_x given by the exponential attenuation law.

$$\frac{I_x}{I_0} = e^{-\frac{\mu}{\rho}x} \tag{2.6}$$

Equation (2.6) can be rewritten as

$$\frac{\mu}{\rho} = x^{-1} \ln\left(\frac{I_0}{I_x}\right) \tag{2.7}$$

From Equation (2.7) μ/ρ can be obtained from measured values of I_0, I_x and x. Values of many element and materials are tabulated [111–113].

2.2 History and Theory of Electrodeposition

2.2.1 Birth and Modern Research in Electroplating

The history of the electroplating dates back to the early XIX century [114] when, after the invention of the Alessandro Volta pile in the 1796, Luigi Valentino Brugnatelli performed in the 1805 the first deposition of gold, from an Au^{3+} solution, on a silver electrode [115,116]. Since then, many improvements have been made: in 1837 Moritz Hermann von Jacobi developed the electroforming of Cu [117]; the Elkington brothers, in the 1840s, filed the first patent for the electrodeposition of gold and silver from cyanide solution [118] and in the 1876 Birmingham became the first electroplating industrial centre. After seventy years, in the 1946 Abner Brenner developed the electroless deposition for the metallization of non-conductive surfaces like plastics [119]; then the development of cataphoresis, electropolymerization [120–123] and electroplating from ionic liquids [124–126] opened in the last decades the possibility to deposit paints, polymers and metals (like aluminium) which were impossible to deposit in water. But in terms of electroplating of metals from aqueous solution the current industrial procedures involve the deposition of alloys and multilayer deposition developed beginning from the 1950s [127–129]. The multilayer architecture has some benefits respect to the direct deposition of the last element on the substrate [130]: it prevents the direct electroless deposition due to redox replacement that will lead to an opaque finishing, it reduces the tensions due to the crystalline mismatches and prevents the diffusion of one metal into the other in a long-term period. The most common multilayer processes are schematized in Figure 2.1.

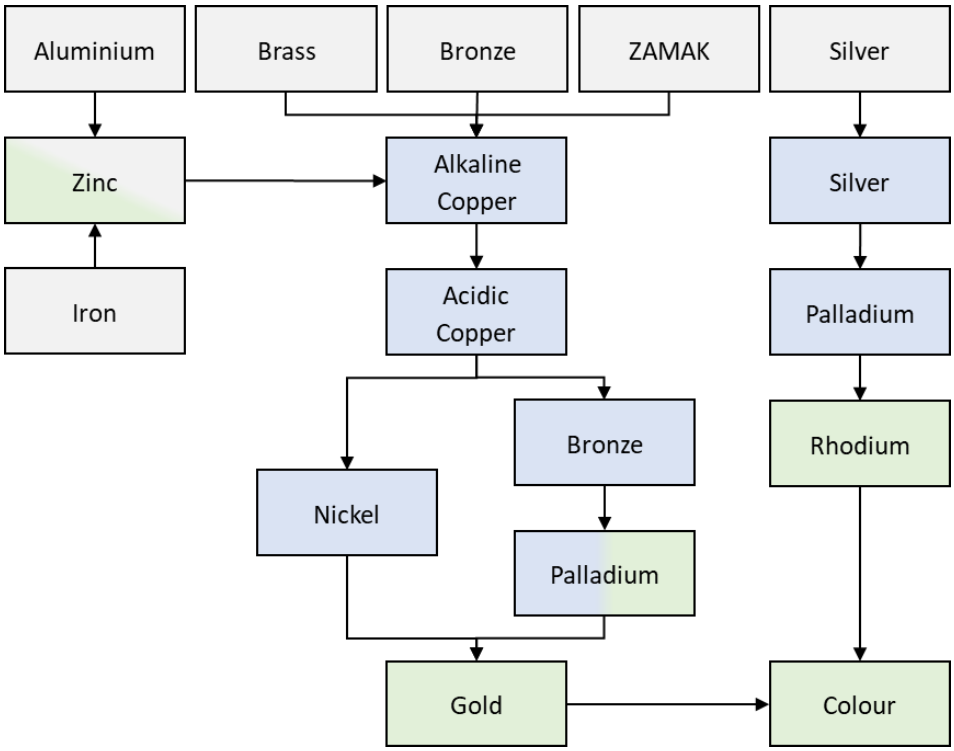

Figure 2.1 – General scheme of the most common industrial electroplating processes. The boxes' colour differentiates between the base metals (grey), intermediate depositions (blue), and the finishing layers (green).

The hottest topics currently in the research of industrial electrodeposition are the reduction of precious metal content from deposits (e.g., from 24 kt gold to 18 kt gold) [131–133] while maintaining good corrosion characteristics, mainly acting on the porosity and compactness of deposits, as well as the use of new alloy materials; the replacement of cyanide from many baths with non-toxic compounds [134]; the elimination of heavy metals which are more or less harmful, such as cadmium, nickel, and palladium [135]; new methods of the management and control of waste and waste water, alternative engineering processes [136–138], and the synthesis of new alloys.

2.2.2 Fundamentals of Electrodeposition

The experimental setup for electrodeposition simply requires a suitable vessel and two conducting electrodes (a working electrode (WE) where the film is deposited, and a counter electrode (CE) used to close the circuit) immersed in an electrolyte containing the metal ions to be deposited. In some cases, a third electrode (the reference electrode (RE)) is introduced to measure more precisely the potential at the electrodes (Figure 2.2), thus providing information on the processes occurring on the WE. The three-electrode setup is used almost exclusively in research and development, since it is extremely difficult to maintain the required condition of zero current and potential stability of the RE in industrial-sized vessels.

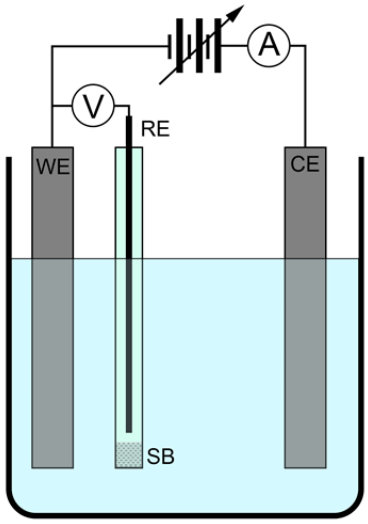

Figure 2.2 – Scheme of an electrochemical cell. WE: working electrode; RE: reference electrode; CE: counter electrode; SB: salt bridge.

The process is run by an external power source, under potential or current control. Both control methods can be used, with the choice being made based on the knowledge gained from three-electrode experiments. For example, a steep current change can be better controlled potentiostatically,

and vice versa. Various waveforms under potential or current control can also be used to tailor the composition and microstructure; multilayers, for example, can be grown by alternately switching the current or potential between two values, and composition at grain boundaries may be tailored by a short anodic pulse. Pulse plating, by using square, triangular, sinusoidal, or custom waveforms, is a versatile method to tailor the composition gradients, morphology and, therefore, also the properties, as discussed in various monographs [139–141]. Metal coatings can be formed by adding only one elemental species (i.e., Cu or Ni) as metallic salts, while alloy coatings can be produced, under well-defined conditions, by having more than one elemental species in the solution.

In electrodeposition the rate of reduction of metal ions determines the current that flows through the cell and the total charge passed yields to overall coating mass and thickness.

$$Me^{z+} + ze^{-} \rightarrow Me \tag{2.8}$$

The formula that relates the amount of deposited mass to the passed charge for the reduction process in Equation (2.8) can be derived from the Faraday's law. If M is the mass of the coating, A_{mol} is the molar mass of the element, Q is the total charge, z is the number of electrons exchanged, and F is the Faraday constant, corresponding to the charge of one mole of electrons, F = 96,485 C/mol = 26.8 A·h/mol, the formula is:

$$M = \frac{A_{\mathrm{mol}} Q}{zF} \tag{2.9}$$

For electrodeposited coatings the knowledge of the thickness with respect to the passed charge is important; in this case the Faraday expression can be modified to give:

$$D = \frac{A_{\mathrm{mol}} j t}{zF\rho} \tag{2.10}$$

Where D is the film thickness, j is the current density (current per unit area), t is the time of deposition, and ρ is the density of the film. Note that the density of an electroplated coating may be different from that of a bulk metal due to the possible presence of vacancies and micro-voids. It should also be noted that Equations (2.8), (2.9) and (2.10) are valid only if no other processes besides Equation (2.8) are occurring.

Equation (2.8) is at equilibrium when the rate of metal reduction in the electrolyte equals that of metal dissolution. Under such conditions the electrode potential E_{eq} is determined by the Nernst equation, which reads:

$$E_{\mathrm{eq}} = E^{\circ} + \frac{RT}{zF}\ln(C_{Me^{z+}}) \tag{2.11}$$

Where E° is the equilibrium potential under standard conditions, R is the gas constant, T is the absolute temperature, ln stands for the natural logarithm, and $C_{Me^{z+}}$ is the concentration of the metal ions in moles per liter.

In order for electrodeposition to occur, the applied potential must be more negative than the equilibrium potential, thus resulting in the reduction/deposition process being faster than the opposite dissolution process. The driving force for metal deposition is, therefore, the difference between the applied potential V_{app} and E_{eq}. This quantity is referred to as the overvoltage:

$$\eta = V_{\mathrm{app}} - E_{\mathrm{eq}} \tag{2.12}$$

The electrodeposition process consists of several elementary consecutive steps: at equilibrium the ions are bound to water molecules or to other molecular species that bind the metal ion, decreasing its effective ability to be

reduced. Metal ions are transported initially in the bulk electrolyte by fluid convection (Figure 2.3). When these ions are at a distance of 0.05 - 3 mm from the electrode (the hydrodynamic layer) the convection process slows down and the ions start to move only due to diffusion (the diffusion layer, 1 - 100 μm) under a gradient of concentration generated by the ongoing reduction of metal ions. These ions are first adsorbed at the electrode surface and are reduced by electrons from the electrode. Note that the electrode/electrolyte interface forms a double layer of charges that generates a large electric field (~10^9 V/m). The process of metal reduction is strongly affected by the presence of this electric field.

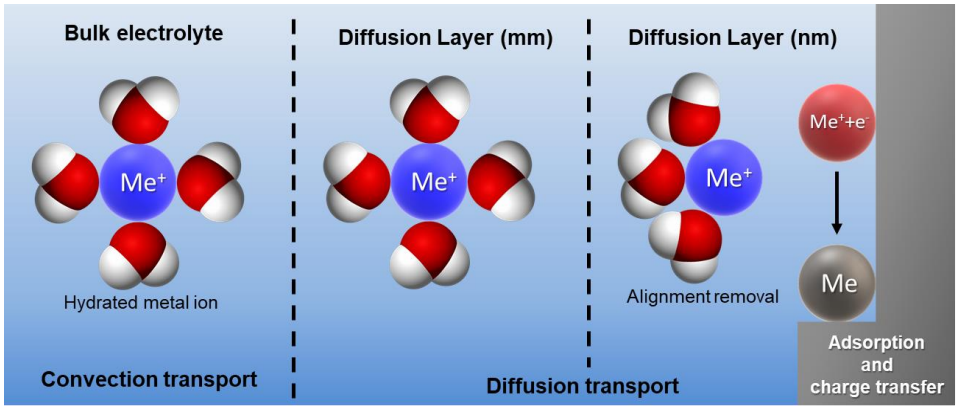

Figure 2.3 - Scheme of transport regimes as a function of the distance from the electrode.

The rate of metal reduction sufficiently far from the equilibrium condition is described by the following expression:

$$J_{\text{kin}} = j_0 \, \mathrm{e}^{-\frac{z\alpha F(V_{\text{app}} - E_{\text{eq}})}{RT}} \tag{2.13}$$

Where j_0 describes the dynamics of the deposition/dissolution processes at equilibrium, and α ($0 < \alpha < 1$) relates to the symmetry of the energy barrier encountered during electron transfer and it is often approximated to 0.5. Note

that the deposition current density increases exponentially with the overvoltage, and at a certain point the deposition rate becomes limited by the arrival of the ions at the electrode surface, which depends from the hydrodynamic conditions imposed in the cell. It is also important to consider that in aqueous solution it is always possible to induce water reduction when the applied voltage is more negative than the redox potential for water reduction to hydrogen.

Under these conditions the process of interest may not occur with 100 % efficiency, and some hydrogen may be evolved or incorporated in the coating, resulting in possible changes in properties, in particular the embrittlement; this phenomenon depends strongly on the nature of the metal being studied. A typical behaviour of the current density as a function of applied potential is shown in Figure 2.4. The overvoltage determines to a large extent the morphology of the deposits. Electrodeposition in Region 1 (Figure 2.4) occurs at low deposition rates, resulting in the possibility for the adsorbed atoms to sit at low energy sites, thus forming, in most cases, a smooth and layered film. In Region 2 the deposition rate increases, leading to the formation of more nuclei of an approximately hemispherical shape. Finally, in Regions 3 and most importantly 4, the current approaches the diffusion-limiting current, resulting in the possible formation of dendritic films showing incomplete coverage of the substrate. In order to form a continuous film, it is most practical to deposit in Region 2, where the spread of the existing nuclei results in a continuous coating at a relatively low thickness. Film morphology, however, depends also on two more features:

1. The nature of the element being deposited, due mainly to the differences in j_0 generated by the electronic structure and the extent of interaction with water.
2. The effect of additives adsorbing at the growing interface; specifically, adsorbing species inhibit growth, resulting in smaller grains and properties changes due to the possibility for the molecules to be incorporated in the growing film.

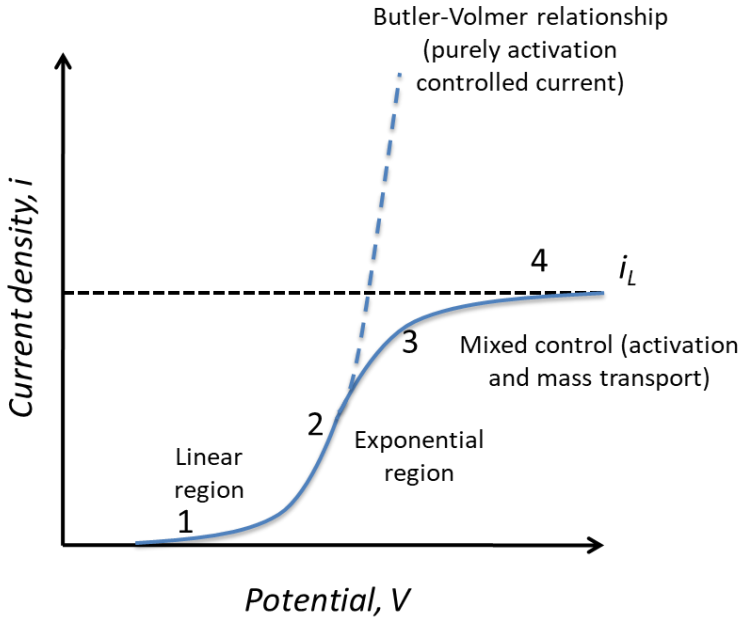

Figure 2.4 – Deposition region dependency from applied potential.

2.2.3 Electrochemical Atomic Layer Deposition

Electrodeposition processes are characterized among others by (i) diffusional transport processes; (ii) the occurrence of electron transfer to reduce a metal ion into an atom in the growing crystal; and (iii) the low energy of the deposition precursors. The latter feature is very important since the free

energy of ions in solution at room temperature is of the order of $3/2k_BT \approx$ 0.075 eV, almost similar to the interaction among atoms in the crystal lattice. This means that, while metal A is deposited on a substrate of the same element at the redox potential predicted by the Nernst equation, the same metal A deposited on a substrate B, where the interaction A-B is stronger than A-A, is deposited at a potential more positive than the value predicted by the Nernst equation giving rise to UPD. The UPD can be estimated by considering that the shift in the redox potential is given by $\Delta E = -\frac{\Delta G}{zF}$ where ΔG is the difference in the adsorption energy of A onto A and the adsorption energy of A onto B. This process enables the formation of sub-monolayers or a full atomic monolayer of A onto B. A second layer cannot be deposited at the same underpotential since the exposed surface is now covered with A, where the deposition potential would be more negative, thus leading to a surface-limited reaction (SLR) that spontaneously generates a single atomic layer.

This behaviour is extremely useful from a technological point of view and, therefore, widely studied by the scientific community. The deposition process itself is called electrochemical atomic layer deposition (E-ALD or ECALD) [81,142,143] and alternating the UPD of A and B ML it is even possible also to obtain three-dimensional layered structures which, due to the nature of the technique, generate homogenous compounds with exact stoichiometry or alloys. In some cases, if the substrate is single crystalline or shows a strong crystallographic orientation, it is possible also to obtain an epitaxial deposition of the coating; this technique is then called ECALE [82,144].

The bonding strength in alloys can be similarly exploited to shift the potential at which an element inside a given alloy can be deposited. The Nernst equation

for the deposition of a metal A into an alloy A-B is modified and given by the formula:

$$E_{\mathrm{eq}}(\mathrm{A})_{\mathrm{alloy}} = E^{\circ}{}_{\mathrm{A}} + \frac{RT}{zF}\ln\left(\frac{C_{\mathrm{A}^{z+}}}{a_{\mathrm{A,alloy}}}\right) \tag{2.14}$$

where $a_{\mathrm{A,alloy}}$ is a measure of the extent of interaction of metal A with the alloy. In a solid solution $a_{\mathrm{A,alloy}} < 1$ (i.e., the free energy of A is lower due to the stronger alloy bonding), raising the redox potential above that calculated in the case of a pure metal. This shows that metal A can be deposited at a potential more positive than the redox potential of A, that is, it can be deposited by underpotential processes, while the metal B continues to be deposited at overpotential [79]. A rigorous calculation using the regular solution approximation allows to predict the conditions (the applied potential) to obtain the target composition, under the assumption that deposition occurs under thermodynamic (equilibrium) conditions. It is important to mention that A and B could also be a metal and a non-metal; in these instances electrodeposition under potential control may form films of semiconductor compounds [145]; at a finer scale, exploiting the E-ALD process it is, thus, possible to alternately deposit one element over the other to artificially synthesise semiconductors [81,146,147].

A multilayer deposition of a single component, with a control on the single monolayer, is possible to be achieved combining the E-ALD with a subsequent selective electrodesorption of the chalcogen layers. In this way the resulting film is constituted by a confined layer of metal which reorganises its shape in ordered crystalline domains. Therefore, the selective desorption of the chalcogen leaves an increasingly higher amount of metals with the number of cycles. The combination of E-ALD with this second stage leads to a

process called Selective Electrodesorption Based Atomic Layer Deposition (SEBALD), which is described in Figure 2.5. SEBALD was successfully used to grow Cd with a control level not achievable in overpotential deposition through the application of Faraday's laws (even when deposition was limited to very low overpotentials) [83] and to obtain Co/Fe catalytic clusters [84].

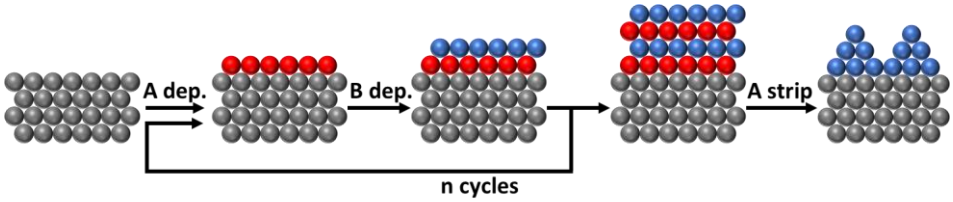

Figure 2.5 – Scheme of the SEBALD process: after a multilayer E-ALD one of the components is selectively desorbed.

2.2.4 Bulk Controlled Deposition

The depositions limited by the surface are not the only choice that allow to obtain a high control on the coating: even charge-controlled or time-controlled depositions can be valid alternatives in the case in which (i) there are no thermodynamic conditions to obtain the UPD; (ii) the deposition of a component is made directly on itself; (iii) the deposition is carried out under different current or potential conditions to obtain different morphologies. In these cases, the control on the process is lower than with SLRs but still very effective.

As it can be guessed from the names, the charge-controlled deposition consists in monitoring the charge, integrating the current that passes through the cell over time, and ending the deposition when the desired quantity has been reached. This method is unable to distinguish the presence of other processes that give rise to faradaic and non-faradaic currents. Instead, the

time-controlled deposition is carried out for a certain predetermined period of time. In both cases the actual quantity deposited can then be verified by performing a stripping and any changes can be made to achieve the desired results. The deposited quantity is evaluated performing a linear sweep voltammetry, with the charge being proportional to the peak area [148–151]:

$$Q = \frac{\int IdE}{v \cdot A} \tag{2.15}$$

Where Q is the charge density, I the current, E the potential, v the scan rate and A the electrode area. The amount of material deposited can be corroborated by the thickness of the deposit or the number of monolayers. The deposited thickness is calculated using the Faraday law and the density of the material:

$$d = \frac{Q \cdot M}{A \cdot \rho \cdot F \cdot z} \tag{2.16}$$

Where M is the molecular mass of the deposited compound, ρ the density, F the Faraday constant and z the number of exchanged electrons. Alternatively, the number, or fractions, of deposited monolayers can be calculated dividing the deposited charge Q by the equivalent charge of a monolayer q Equation (2.17)(2.17.

$$q = \frac{z \cdot n \cdot F}{a \cdot N_A} \tag{2.17}$$

Where n is the number of atoms per unit cell, a is the area of a unit cell and N_A the Avogadro's number. For example, in the case of a monocrystalline Ag(111) electrode: the cell constant is 4.085 Å, the side of the (111) triangular unit cell is 5.777 Å and the area is 14.45 Å^2. The atoms inside this area are $3 \cdot$

$\frac{1}{2} + 3 \cdot \frac{1}{6} = 2$. Therefore, the equivalent charge of a monolayer for a monoelectronic reaction is 222 $\mu C/cm^2$.

3 Characterization of Thin Films

3.1 Analytical Approach

EDS and XRF are techniques that interpret every sample as homogeneous, even if it has a layered structure, since the output information it is a spectrum in which the number of X-ray photons that arrive on the detector are function of the atomic concentration of the elements in the sample. For this reason, there is no direct information on the thicknesses, but the intensity of the peaks in the spectra will be function of thickness. In fact, a sample with a thicker coating will emit more photons from the film and less from the substrate than a thinner one, as represented in Figure 3.1.

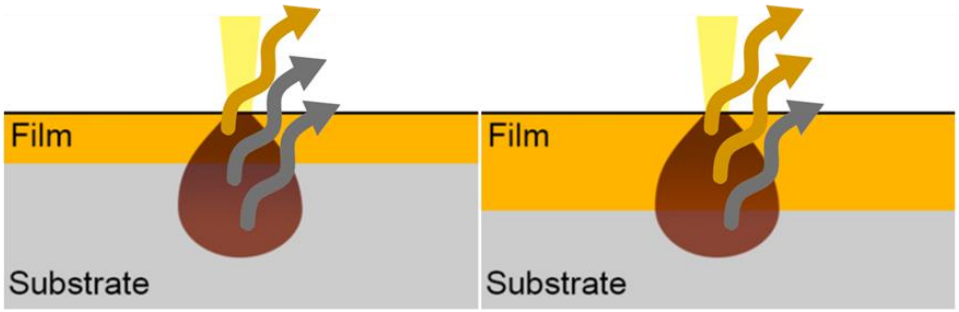

Figure 3.1 – Representation of the X-rays emitted from samples with a coating of different thickness.

For this reason, is possible to build a calibration curve to extrapolate the thickness of the investigated sample. However, the preparation of standards with known thickness is unpractical in many situations for the variability of the materials and the thickness range. An alternative can consist of designing semiquantitative approaches that are based on calibration curves obtained with a simulation software. These features open the possibility of extending the technique for the investigation of the film thickness. During the

simulation, when the materials and the architecture to simulate are chosen, it is also possible to specify the density of the materials; in this way the user can decide to simulate materials that have a porosity different from the nominal one due to the deposition method, as for example happens during electroplating in which the density of the coatings is often lower than that of the bulk material.

In the case of EPMA, there are many works in which the problem has been addressed by choosing different approaches: both in terms of obtaining the calibration curve, using standards of known thickness [16,152] or Monte Carlo simulations [153,154]; regarding the quantification method the K-ratio [98,155–157], the ratio of intensity [158] or atomic ratio [152]; to obtain information about absolute thickness [15,16,159] or mass thickness [160–163]. In the last fifty years many software were written to simulate EDS spectra; many of them are written by researcher and some were commercial: MAGIC [164,165], STRATAGEM [166–168], GMRFILM [93], Electron Flight Simulator [169,170], ThinFilmID [171] and LayerProbe [171,172], pyPENELOPE [173,174], Win X-Ray [175,176] and MC X-Ray [175,177], CASINO [95,178–181], CalcZAF [182,183] and DTSA-II [184–186]. Many of these software exploits the PENEPMA algorithm [174]. PENEPMA is a simplified version dedicated to EPMA, written to perform simulation of X-ray spectra and calculates different quantities of interest, of another algorithm called PENELOPE. PENELOPE (Penetration and ENErgy LOss of Positrons and Electrons) is a general-purpose Monte Carlo code system for the simulation of coupled electron-photon transport in arbitrary materials. PENELOPE covers the energy range from 1 GeV down to, nominally, 50 eV. The physical interaction models implemented in the code are based on the most reliable information available at present, limited only by the required

generality of the code. These models combine results from first-principles calculations, semi-empirical models and evaluated data bases. It should be borne in mind that although PENELOPE can run particles down to 50 eV, the interaction cross sections for energies below 1 keV may be affected by sizeable uncertainties; the results for these energies should be considered as semi-quantitative. PENELOPE incorporates a flexible geometry package called PENGEOM that permits automatic tracking of particles in complex geometries consisting of homogeneous bodies limited by quadratic surfaces. The PENELOPE code system is distributed by the OECD/NEA Data Bank. The distribution package includes a report [187] that provides detailed information on the physical models and random sampling algorithms adopted in PENELOPE, on the PENGEOM geometry package, and on the structure and operation of the simulation routines. PENELOPE is coded as a set of FORTRAN subroutines, which perform the random sampling of interactions and the tracking of particles (either electrons, positrons or photons). In principle, the user should provide a main steering program to follow the particle histories through the material structure and to keep score of quantities of interest. In PENEPMA photon interactions are simulated in chronological succession, allowing the calculation of X-ray fluorescence in complex geometries. PENEPMA makes extensive use of interaction forcing (a variance-reduction technique which artificially increases the probability of occurrence of relevant interactions) to improve the efficiency.

In the case of XRF, the software to simulate the spectra are considerably less, probably because the FP was preferred for many years since it was computationally favourable, but with the last technological development even a personal computer could arrive to obtain a good simulation in relatively small amount of time. The two main software that provide a simulated spectra

with MC approach are: XRMC [188] and XMI-MSIM [189]. Both codes use the Xraylib database [190,191]. XRMC is generally used for complex 3D geometries while XMI-MSIM can only simulate samples composed of parallel layers, but for simple geometries XMI-MSIM is currently superior to XRMC in simulating XRF experiments [192].

Besides the cost of the hardware, the main differences between EDS and XRF is the probe, electrons and X-ray respectively, and consequently the depth that it can be analysed. The spectrum and the emission lines produced are the same for both the techniques and for this reason I have performed the thickness measurements with EDS as well as with XRF. In order to estimate the penetration depth, we can employ the attenuation length (value at which the transmittance falls at 37 %). We have to take into account both the penetration of the probe as well as the emitted photons. I reported an example with the two techniques using two metals with considerably different atomic numbers, copper and gold; a typical acceleration potential used for EDS experiments is of 25 kV while for the XRF it is of 50 kV. To have a qualitative comparison we can assume that the energy of electrons and photons is equal to the acceleration potential. The attenuation length for electrons with 25 keV energy in copper is about 0.87 μm while in gold it is 0.43 μm (Figure 3.2), as obtained through simulations with the CASINO software. In the case of photons with an energy of 50 keV, the attenuation length is 386 μm for copper and 67 μm for gold (Figure 3.3), data from the NIST database [111]. In both cases, however, the photons emitted will have the characteristic energy of the elements: Cu L 930 eV, Au M 2120 eV, Cu K 8050 eV and Au L 9713 eV. The attenuation lengths are reported as following (Figure 3.3): Cu L 0.74 μm and Cu K 22.5 μm in copper and Au M 0.58 μm and Au L 4.3 μm in gold. From these results, which are schematized in Figure 3.4, we can see that the

limiting factor in the depth analysis is the probe in the case of the EDS and the material in the case of the XRF. For this reason, if we want to analyse very thin films, we have to use the EDS, and also to reduce as possible the energy of the beam to minimize the signal of the substrate; in fact, this kind of films are practically transparent to the XRF because their signal it is negligible with respect to the large volume detected. On the other hand, a thicker film needs the deeper penetration of the XRF, in fact the EDS may not penetrate the film which would therefore be interpreted as infinitely thick.

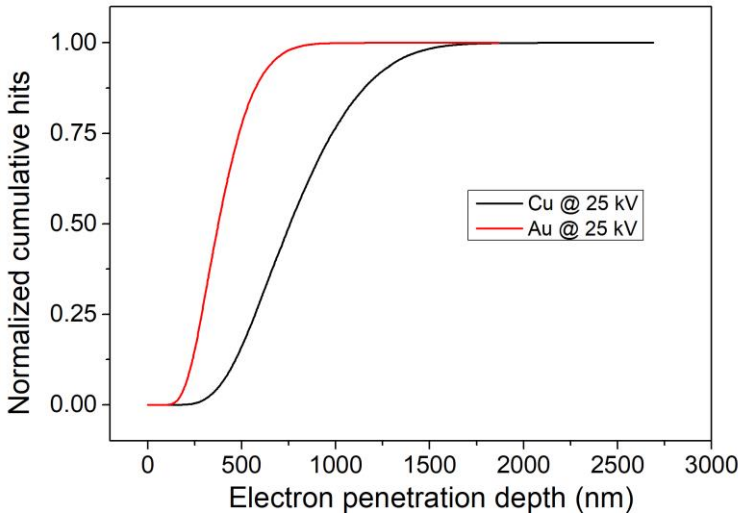

Figure 3.2 – Penetration depth of electrons with an energy of 25 keV in copper and gold.

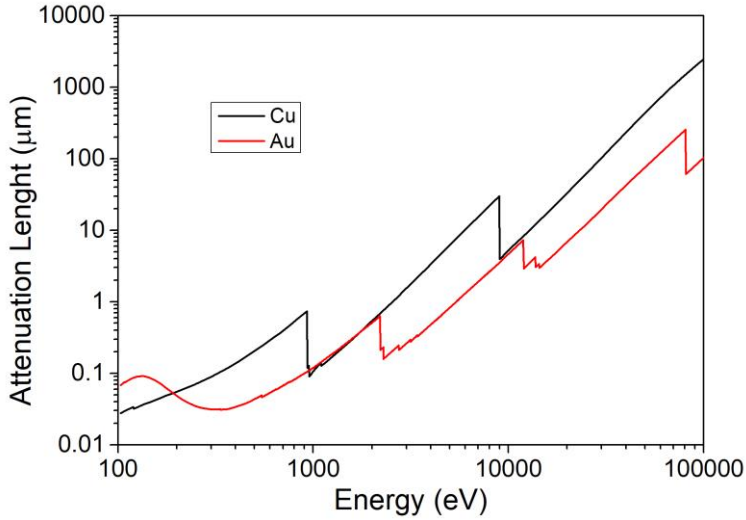

Figure 3.3 – X-ray attenuation length as function of the energy of the photons for copper and gold.

Figure 3.4 – Schematic representation of the different maximum depths for EDS, characteristic X-ray and XRF.

The working method that I would like to develop needs to be applicable to real measurements in industrial environment. For this purpose, simulation software has been used, since the preparation of known standards is a long, expensive and complex process, especially in the industrial field. The method proposed is schematized in Figure 3.5 and described as follows:

1) The experimental conditions (hardware geometry, beam energy, etc.) and the elemental composition of the sample that has to be analysed must be known as best as possible.

2) The simulation of all the pure elements and of the "standards" with variable thickness must be performed.

3) At the same time, the sample is measured, as well as the bulk pure elements (this is the only standard measurement needed, easier to find and cheaper than a certified thin film standard)

4) The intensity of the peaks are calculated from the spectra, both the ones simulated as well as those measured ones, and they are normalized with respect to the corresponding pure element, this value is called K-ratio (EDS) or peak ratio (PR, XRF). In this way differences in the simulation and measurement can be minimized.

5) With the ratios from the simulated spectra a calibration curve can be built and finally, from the ratio obtained from the measured spectra, the thickness can be derived.

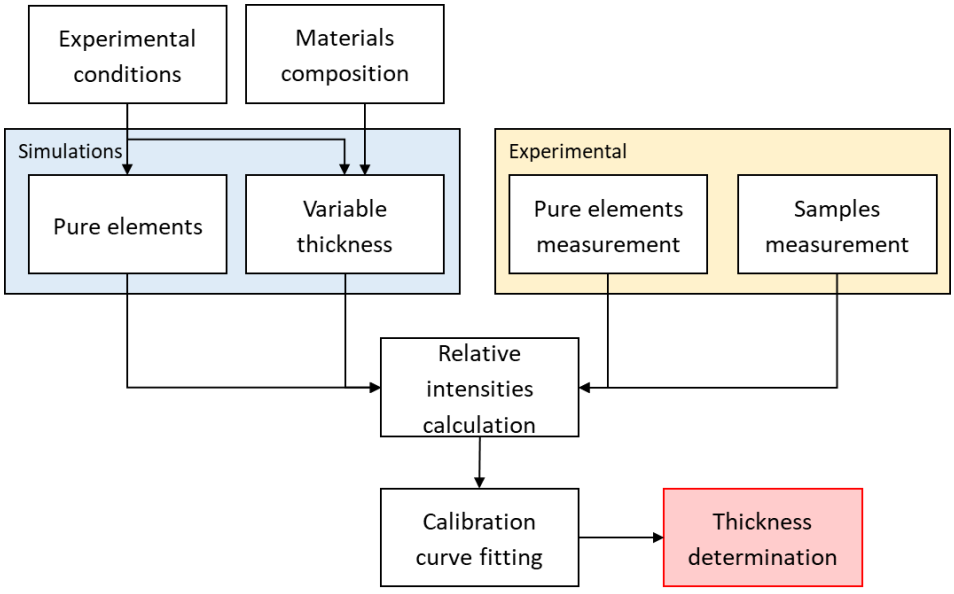

Figure 3.5 – Flowchart of the algorithm used in the analytical method proposed for the standardless determination of the film thickness in coated samples using simulations.

Summarizing, the proposed one is a different approach to the processing of data obtained with traditional, and already consolidated (accuracy, precision, reproducibility, reparability, etc.), techniques. The results that follow are preliminary and serve to prove the qualitative potential of this method, although it has the ultimate aim of providing better quantitative results, and at a lower price, compared to the data interpretation that is currently performed with these techniques.

3.2 EDS for Thickness Determination

EDS applied to galvanic industry is a valuable technique to precisely investigate films of precious metals and finishing colours because they generally range between 50 nm and 1 μm [130]; the deposition of non-precious metals instead ranges approximately from 1 μm to 10 μm, above 10 μm – 20 μm it is called electroforming [193]. The maximum thickness that can be analysed with the EDS method is about some microns: this is determined by the acceleration potential of the electrons together with the atomic number of the elements in the sample. In Figure 3.6 is shown the maximum thickness that can be measured by EPMA for some metals in relation to the electron beam energy; it is to be noticed that both colour deposits and thick deposits are theoretically measurable [6]. On the other hand, the minimum detectable thickness (lower detection limit) is given by the combination of the X-ray energy characteristics of the elements in the sample and the properties of the detector and can be as low as a few monolayer or less [7].

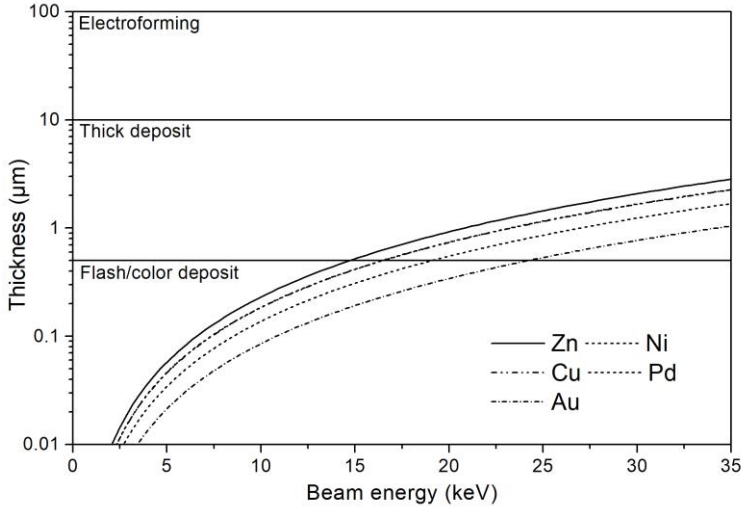

Figure 3.6 - Maximum EPMA measurable thickness as function of beam energy for Zn, Ni, Cu, Pd and Au. The typical classification deposits based on the thickness for decorative applications are also shown.

3.2.1 Spectra Simulation Software

While performing the simulations, it is important to consider that there are some possible sources of error that could produce unexpected and wrong data:

1. The number of electrons simulated, which affects the accuracy.
2. The knowledge of the sample (elemental composition and layers architecture) that must be simulated, together with the hardware (geometrical parameters, detector and source efficiency, etc.).
3. The goodness of the physical model used from the software, which affects the precision of the results.

Different EDS simulation software operate with different algorithm and models, for this reason I have tested some of them to find the best one for

my purpose. The K-ratio parameter was used to build the calibration curves employed for quantification. The software used in this work were NIST DTSA-II Jupiter 2017-07-05 [184] (from now indicated as DTSA2), CASINO 2.4.8.1 [178] and CalcZAF 11.7.4 [182]. The choice fell on these software because, besides the publications which attest to the validity of the models used [95,186,194–196], their development is still active and there is a still active community for technical support.

DTSA2 shares many physical models with PENEPMA but was designed exclusively for simulation of X-ray spectra generated by sub relativistic electrons. DTSA2 uses variance reduction techniques unsuited to general purpose code. These optimizations help the program to be orders of magnitude more computationally efficient while retaining the detector position sensitivity. Simulations are executed in minutes rather than hours and differences that result from varying the detector position can be modelled. It is possible to insert the characteristics and the geometry of the detector in DTSA2, which is capable of handling complex sample geometries. The primary and secondary bremsstrahlung and fluorescence can be calculated. The outputs consist in a real-looking spectrum since it is deconvoluted considering the detector resolution; even the electron trajectories can ben visualized.

The CASINO is a single scattering Monte Carlo simulation software of electron trajectory in solid specifically designed for low beam interaction in a bulk and thin foil. This software can be used to generate many of the recorded signals (X-rays and backscattered electrons) in a scanning electron microscope. This program can also be efficiently used for all the accelerated voltage found on a field emission scanning electron microscope (0.1 to 30

keV). The characteristics and the geometry of the detector are not taken into account and the output is not a spectrum but the characteristic emission lines intensity as function of the depth.

CalcZAF simulation software is based on PENEPMA and is a general-purpose software package for simulation of both relativistic and sub relativistic electron interactions with matter. Even in this case, the characteristics and the geometry of the detector are not taken into account and the output consists in a lines-like unconvoluted spectrum.

3.2.2 Samples Preparation and Methods

Nine samples were fabricated using three different metal coatings and three different thicknesses to have enough variability to be tested (Table 3.1). Copper slabs (10x25x1.2 mm), polished with brushes and cotton by a bijou producer, were chosen as substrate to have the same material to those used in the galvanic industry. The plates were ultrasonically cleaned in acetone for 10 minutes, then rinsed several times in ethanol and finally dried in a stove at 65 °C for 40 minutes. Keeping in mind the theoretical limits in detection showed in Figure 3.6 the deposit are of few hundred nanometres of metal, by physical vapor deposition (PVD) with the sputtering method; this kind of deposition was chosen, instead of electrodeposition from solution, because it this is more reproducible and homogeneous and therefore more suitable for the study of the technique but technically not different from a galvanic deposit. Furthermore, even PVD is used in industrial applications for film deposition. An Emithch K575X coater (Lewes, UK) equipped with a DC sputter was used. Au, Pd and Ni have been chosen for the deposit because they represent the most common metals used in the galvanic accessories and bijou;

moreover, they have very different atomic weights and it would be interesting to evaluate if and how the results will change with this parameter. The argon pressure in the chamber was set to 10^{-2} mbar, and for each metal the following cycles were done: one to three cycles of 4 min in horizontal position at 50 mA for Au and 100 mA for Pd and Ni; the targets have a diameter of 54 mm and are 40 mm away from the deposition stage. To achieve the maximum uniformity, the samples were placed on a rotating plate during the deposition, out of the rotation axe. Furthermore, I marked the centre of the samples to take the spot measurements (EDS, XRF and SEM) approximately in the same place.

Table 3.1 – Scheme of the fabricated samples

Sample	Composition	PVD deposition
Au1	Au/Cu	50 mA, 4 min.
Au2	Au/Cu	50 mA, 8 min.
Au3	Au/Cu	50 mA, 12 min.
Pd1	Pd/Cu	100 mA, 4 min.
Pd2	Pd/Cu	100 mA, 8 min.
Pd3	Pd/Cu	100 mA, 12 min.
Ni1	Ni/Cu	100 mA, 4 min.
Ni2	Ni/Cu	100 mA, 8 min.
Ni3	Ni/Cu	100 mA, 12 min.

The plates were weighed with a scale (Mettler AE240, Columbus, OH, USA, accuracy 0.01 mg) before and after deposition to obtain the amount of deposited metal and, by means of the surface area and the density of the deposited metal, the thickness of the film were calculated. Standardless industrially used XRF and, after the EDS measurement, cross section SEM measurements were also performed to compare the results of different instruments. The XRF used was a Bowman B series (Schaumburg, IL, USA)

and the measurement were performed with 50 kV acceleration voltage, at 12 mm focal distance with 0.3 mm window; the quantification was performed using the FP algorithm of the commercial software of the instrument. The SEM and EDS measurement were performed with a FEI QUANTA 200 (Hillsboro, OR, USA) equipped with EDAX GmbH NEW XL-30 detector (Mahwah, NJ, USA) and analysed with EDAX Genesis software [197] and a Hitachi S-2300 (Tokyo, Japan) equipped with a Thermo Scientific Noran System 7 detector (Waltham, MA, USA) and analysed with Pathfinder software [198]. The EDS measurements of the samples and pure elements were performed at both 20 keV and 30 keV with a 300× magnification by analysing an area of about 0.2 mm^2, a low magnification was chosen to mediate the geometric and deposition heterogeneities. A Dead Time (the time after each event during which the system is not able to record another event) of about 30 % was used and the live time was varied to obtain high resolution spectra with a total of about 10^6 counts. The SEM-EDS system was calibrated before the measurements, obtaining a resolution (FWHM at Mn Kα) of 129.1 eV. Before performing the SEM characterization, to preserve the film integrity, the samples were galvanized with a layer of about 20 μm of copper to obtain a sandwich-like sample and a clear profile after the lapping process. The samples were then cut in the middle, incorporated into epoxy resin and lapped, initially with gradually finer sandpaper and then with diamond suspension up to 0.3 μm. Finally, the SEM measurement were performed using backscattered electrons (BSE) and the images were analysed with ImageJ [199].

To evaluate the applicability of the quantification method proposed and to give it a practical value, a sample was prepared also by a bijou producer using a common industrial galvanic process with commercial baths: a brass

plate was coated galvanically with copper (5 minutes in alkaline copper solution, 0.5 A/dm^2 + 10 minutes in acid copper solution, 2 A/dm^2) and then with gold (10 minutes in gold-nickel 24 karats, 1 A/dm^2).

3.2.3 EDS Simulations and Thickness Determination

The Monte Carlo simulations were performed at 20 keV and 30 keV with the following parameters:

- 80, 110, 150, 200, 270, 340, 390, 450, 520, 600, 700 nm of Au on Cu
- 110, 140, 190, 260, 370, 500, 570, 660, 760, 890, 1090 nm of Pd on Cu
- 45, 60, 80, 110, 150, 200, 250, 300, 350, 400, 460, 540 nm of Ni on Cu
- Au, Pd, Ni thick pure elements

The interaction of 16000 electrons with the standards was simulated using the three software DTSA2, CASINO and CalcZAF (Figure 3.7). The total number of simulations was 222. The time needed for each simulation was approximately 15 minutes with DTSA2, 3 minutes with CalcZAF and 1 minute with CASINO. The simulations were performed using an ordinary personal computer (CPU i5 3.3 GHz, RAM 4 GB).

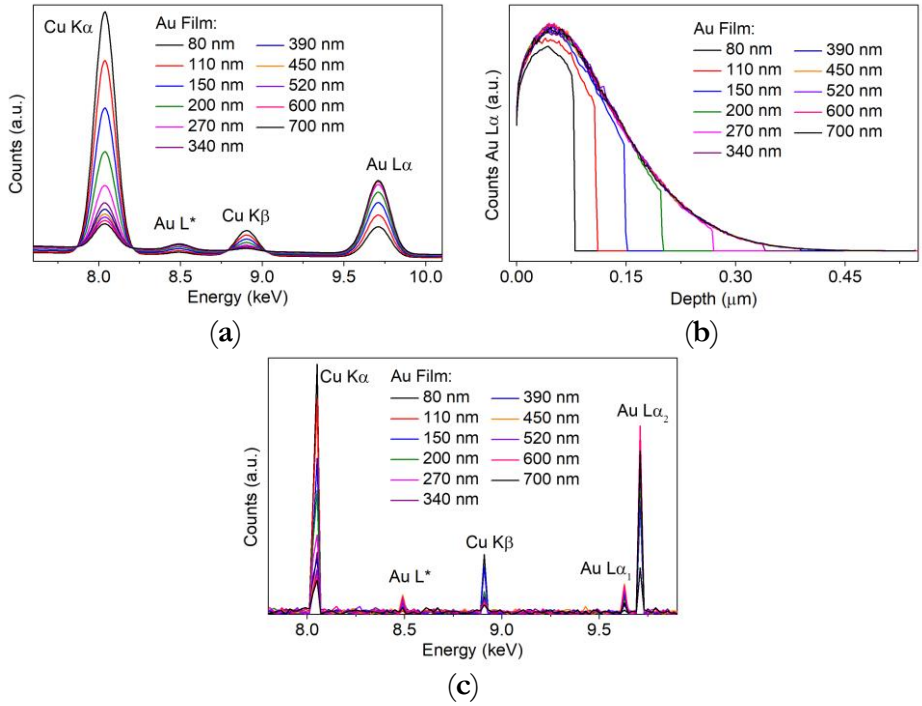

Figure 3.7 – Examples of simulated data for the Au films on Cu substrate performed using a beam energy of 20 keV with (a) DTSA, (b) CASINO and (c) CalcZAF.

After simulating the spectra, the K-ratio were calculated to plot the calibration curves and to obtain the thickness from the measured samples. For the quantification, the lines used was Au Lα, Pd Kα and Ni Kα. The K-ratios were calculated using Equation (2.1) by dividing the background-corrected peak intensity of the simulated standard by the intensity of the same peak in the infinite thick pure element spectra.

The calibration curve was fitted on simulated data with Equation (3.1)

$$y = 1 - e^{-(Ax+Bx^2)} \tag{3.1}$$

This simple analytical function permits the fitting in a wide range of thicknesses [157]. The dependent variable x represents the thickness of the film and the independent variable y the resulting K-ratio. A and B are free

parameters adjustable in the fitting process with values close to 10^{-3} and 10^{-6} respectively. The parameter *A* influences the linear term and could be interpreted as correlated to the attenuation (stopping power) of electrons and photons in the sample while the coefficient of the quadratic term, *B*, includes the electron backscattering and instrumental factors. According to that, the linear parameter tends to decrease by increasing the atomic number, in contrast to the quadratic term which increases with the atomic number. Data have been fitted (Figure 3.8) and the function used appears to be in good agreement with the experimental data.

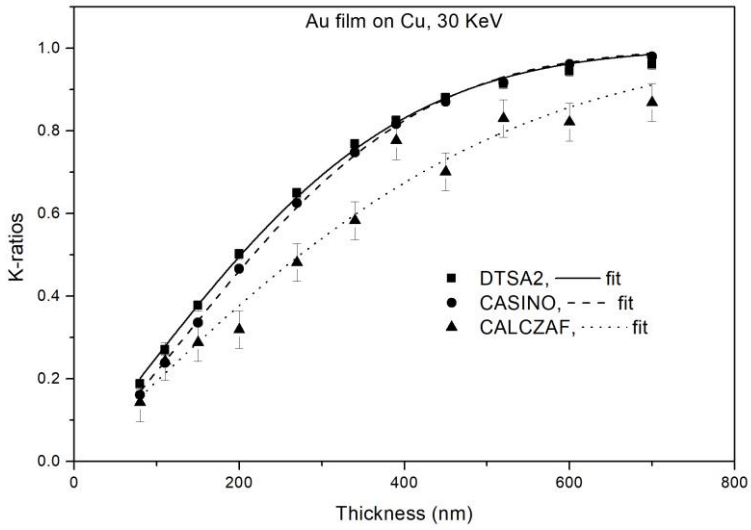

Figure 3.8 – Examples of simulated data and fitted calibration curves of Au film on Cu substrate performed with a beam energy of 30 keV.

Meanwhile, the nine fabricated samples were analysed with a weight scale, XRF, EDS and SEM cross section. Even the pure bulk element (Au, Pd, Ni, and Cu) was gauged with EDS. The K-ratios of measured samples were estimated from the spectra as described for the simulated spectra and the results were used in combination with the corresponding calibration curve to

obtain the thickness of the film. These results, obtained with the MC method, are called from now on EDS.

The film thickness was obtained from the weight scale measurement using Equation (3.2) were Δm is the weight of the film (calculated as the variation of the sample weight before and after the deposition), ρ is the density of the deposited element and S is the exposed surface.

$$t = \frac{\Delta m}{\rho S} \tag{3.2}$$

The XRF spectra were interpreted using the built-in commercial software of the instrument thought the FP method.

Only the samples with gold and palladium coating (Figure 3.9) were analysed with SEM cross section because the Ni film was not visible with our instrument, since the contrast was too low between nickel film and copper substrate, because the two elements are one next to the other in the periodic table and consequently they have similar atomic number. The samples cross section was prepared by hand: the samples were (i) cut with a grinder, (ii) incorporated in a conductive resin and (iii) polished, initially with gradually finer sandpaper, and then with diamond dust suspended in water, up to a mesh of 0.3 μm. The resolution of these images is not very high, due to the instrumentation used, but it is still enough for our purpose to evaluate the thickness of the precious coating (white line) under examination.

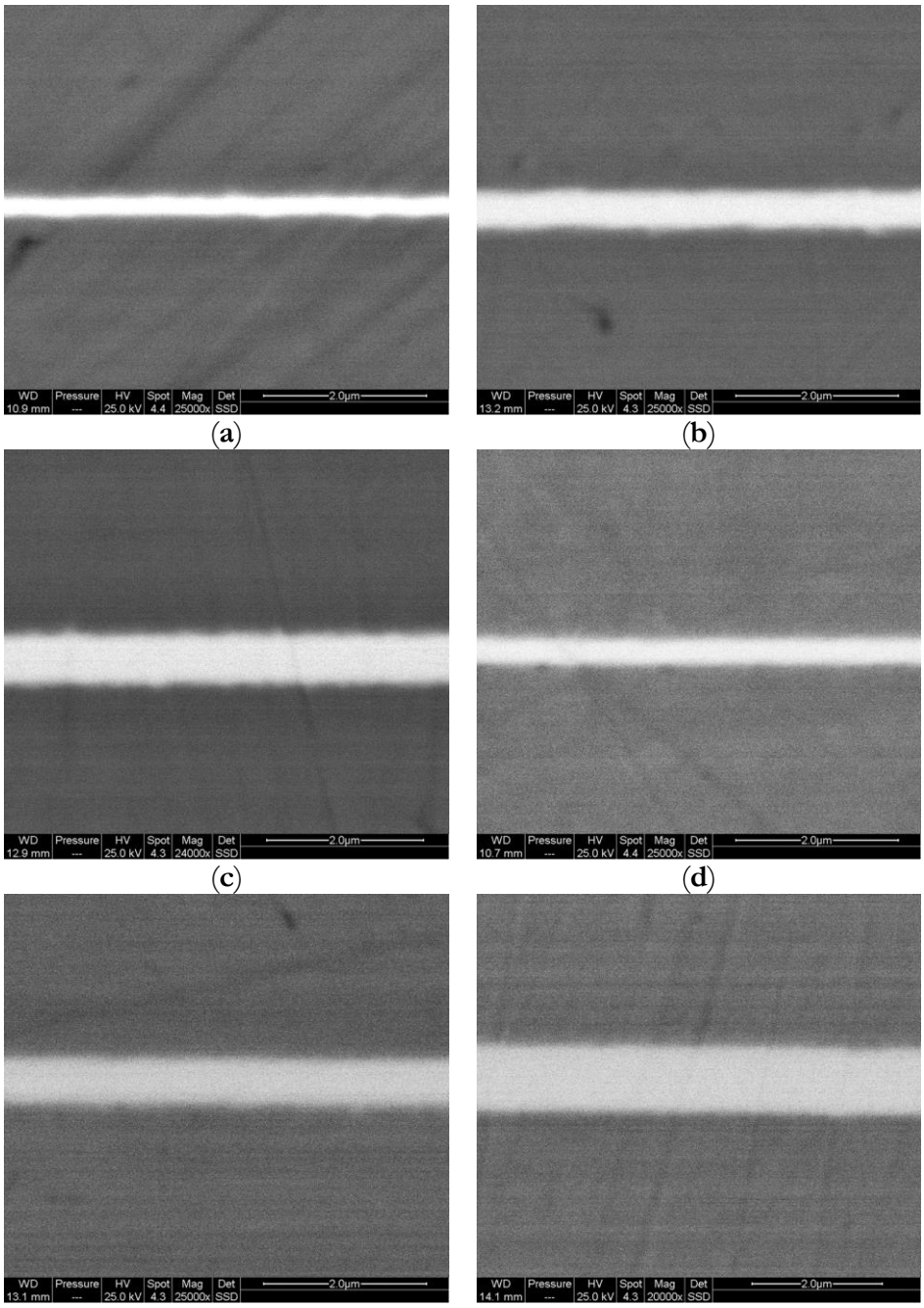

Figure 3.9 – Cross section SEM analysis using backscattered electrons of the samples (a) Au1, (b) Au2, (c) Au3, (d) Pd1, (e) Pd2, (f) Pd3.

To evaluate the best simulation software, the results have been benchmarked against XRF. This because XRF is currently the reference technique for non-destructive measurement of thickness for electrodeposited metal coatings. Moreover, XRF well mediates any local inhomogeneity (contrary to SEM) but the measured area is relatively small, avoiding errors that could come from an inhomogeneous deposition (contrary to weight scale measurement). The mean value of the deviations between EDS and XRF of the nine samples is showed in Table 3.2. The best EDS results, relative to XRF, come from 30 keV measurements. This probably because a higher probe penetration is needed for the thickness investigated. The best software results to be DTSA2 with an average deviation from XRF of 9.6 %, which is consistent with the data from literature obtained from EDS measurement using calibration curves derived by measured standards [158].

Table 3.2 – Mean deviations of the nine samples results between EDS and XRF obtained with the different conditions and software.

Accelerating potential (kV)	**Simulation software**	**EDS – XRF deviation**
20	DTSA2	19.2 %
20	CASINO	23.1 %
20	CalcZAF	15.7 %
30	DTSA2	9.6 %
30	CASINO	9.7 %
30	CalcZAF	20.4 %

In Table 3.3 is shown the comparison between the thickness measurement obtained among the different instruments used; in Figure 3.10 these results are plotted overlapping the calibration curves (inverse function).

The EDS results are comparable to XRF results, instead SEM and weight scale results are in less agreement but this is probably due to the quantification method used: in the case of the weight scale method, inhomogeneities in the deposition and the real density are not considered; in the case of SEM imaging the preparation of the cross sections by hand could have some role in the deviation of the results.

Table 3.3 – Measured thickness values obtained with all the different techniques. In the case EDS the results derived from the measurements performed with an accelerating potential of 30 kV using DTSA2 software are reported since they have the smallest deviation respect to XRF. The deviation between EDS and XRF for all the measurements are also reported.

Sample	Weight scale (nm)	XRF (nm)	SEM cross section (nm)	EDS (nm)	EDS-XRF deviations
Au1	151 ± 31	135 ± 8	207 ± 30	143 ± 14	5 %
Au2	338 ± 30	318 ± 29	329 ± 30	304 ± 29	-5 %
Au3	523 ± 32	488 ± 49	528 ± 30	416 ± 40	-15 %
Pd4	193 ± 30	204 ± 50	234 ± 30	210 ± 20	3 %
Pd5	498 ± 30	437 ± 76	473 ± 30	412 ± 40	-6 %
Pd6	755 ± 32	647 ± 71	785 ± 30	615 ± 59	-5 %
Ni7	83 ± 30	176 ± 22	n.a.	134 ± 13	-24 %
Ni8	251 ± 30	306 ± 42	n.a.	260 ± 22	-15 %
Ni9	401 ± 32	429 ± 72	n.a.	390 ± 38	-9 %

In Table 3.3 it can be observed that the deviation between EDS and XRF increases with the thickness in the case of gold coatings, while there is an opposite trend in the case of nickel films. This is due to the complementarity of the two instruments and the probes they use: with EDS the electrons are not very penetrating, therefore thick films of heavy elements, such as gold, are measured with more difficulty, while thin films of lighter elements, such as

nickel, generate a small signal in XRF measurements due to the strong penetration of X-rays.

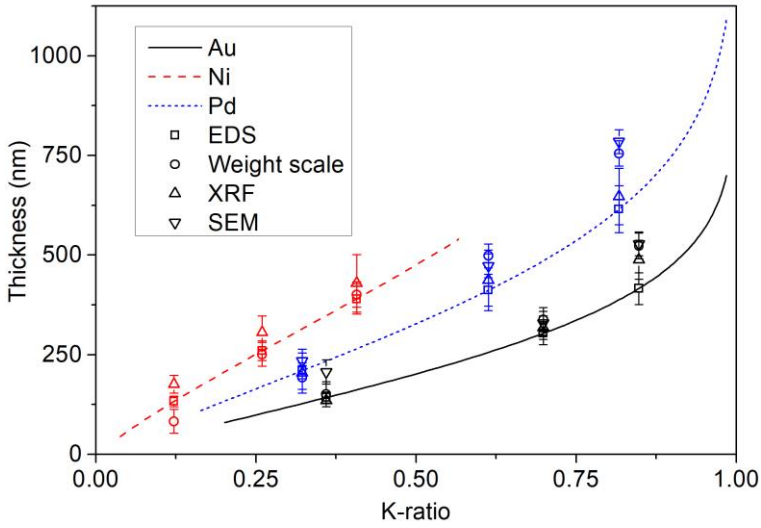

Figure 3.10 – Thicknesses of the metals deposited measured with weight scale, XRF, SEM cross section and EDS (DTSA2 simulations results) with error bars. The calibration curves (inverse function) are overlapped.

3.2.4 Application of the Method to Electroplated Samples

The effectiveness of the method, studied on samples prepared with sputtering, has been then tested in the case of a non-ideal galvanic deposit consisting of a gold layer deposited on a thick copper film on a brass substrate.

With the electron beam energies used in this study, the emitted X-rays come from a maximum depth on about 2 μm; for the deposition time used the copper deposit (under the thinner gold one) is between 6 and 10 μm, so it is reasonable to consider the copper layer as a massive substrate. On the sample an XRF analysis was performed, then the EDS measurement, and

finally, after depositing a further layer of copper as a support, a SEM measure of the cross section.

The gold deposit obtained from a commercial electroplating bath, although marketed as 24 kt, has a minimum percentage of nickel. This is not unusual since small percentages of other metals are often added to gold to improve mechanical properties and change its colour. The actual gold karats of the deposit were obtained through the EDS. Since the film is not thick enough, copper is visible in the spectrum. Applying ZAF correction, the percentage by weight of the three metals was obtained. Since copper is not present in the deposition solution, and consequently in the coating, the sum of the percentages by weight of gold and nickel has been normalized to 1, obtaining a Ni:AuNi fraction of 2.5 % in average, with an actual gold rating of 23.4 kt. This data is already very important itself for the characterization of the coating and it is an information very difficult to obtain through XRF since the volume investigated is bigger, so small fractions of metals are hard to quantify. The use of the karat could hide the presence of small percentages of other metals, therefore the formalism in percentage by weight is more accurate. This type of data extraction has been validated by performing simulations of film thicknesses 200, 400, 600 nm and infinity at 20 keV; calculating the fraction of nickel compared to gold, as described, it always gets a percentage of 2.5% on average, with small oscillations intrinsic in the simulation and which fall into the measurement error and the background assessment. Simulation keeping the same film thickness of 400 nm and varying the beam energy (15, 20 and 25 keV) have also been performed obtaining similar results. This kind of test has been done also on the sample, and the results are shown in Table 3.4.

Table 3.4 – Nickel fractions obtained from simulations (*) and measurements of gold–nickel alloy on copper by varying thickness and energy.

Thickness (nm)	Energy Beam (keV)	Ni (%wt.)	Cu (%wt.)	Au (%wt.)	Ni:AuNi (%wt.)
200*	20	1.79	20.60	77.61	2.25
400*	20	2.28	9.89	87.83	2.53
600*	20	2.28	7.94	89.79	2.48
Bulk*	20	2.60	0.00	97.40	2.60
400*	15	2.16	7.61	90.24	2.34
400*	25	1.90	11.93	86.17	2.16
Sample	15	1.88	4.61	93.50	1.97
Sample	20	2.69	8.08	89.23	2.92
Sample	25	2.15	14.42	83.43	2.52

For the thickness quantification of this sample the DTSA2 software was chosen to use, considering the good results obtained on the previous study on PVD samples.

From a preliminary XRF measurement the thickness of the coating results to be approximately 400 nm. Therefore, 6 standards were simulated in a range of thicknesses from 300 nm to 550 nm, so that in this way the sample was within the calibration curve. For the film simulation, a 97.5 % gold-nickel alloy, with the theoretical density of 18.75 g/cm^3 was used.

Figure 3.11 shows the results obtained from XRF, EDS and SEM measurement. The difference in the EDS measurement from XRF is only 3.9 % exceeding the expectations. The dashed line represents the average of the three measurements that corresponds to 402 nm.

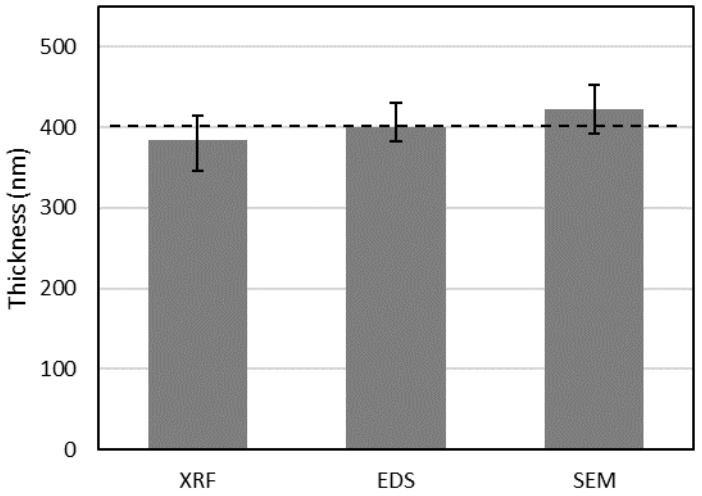

Figure 3.11 – XRF, EDS and SEM thickness measurement of the galvanized sample. The dashed line shows the average thickness of 402 nm.

3.3 XRF for Thickness Determination

Since XRF is less expensive and already widespread in the industries it will be interesting if the quantification method proposed for EDS could be also applied to XRF data. For this reason, I followed the same approach to reduce the measurement uncertainty in the results and their dependence on standards by introducing a new semi-quantitative method (only the pure bulk element spectra will be needed to be measured) based on Monte Carlo (MC) simulations but maintaining the existing instrumental configuration.

The relative intensity of the peak of interest, called the Peak Ratio (PR) henceforth, have been used for the quantification. The PR concept is similar to the K-ratio used in the EDS [86,193] and consists of the ratio between the peak intensity (X-ray counts) for the element of interest in the sample and the

peak intensity at the same energy for the infinite thick, pure element, as reported in Equation (3.3).

$$\mathrm{PR}_i = \frac{I_i^{\mathrm{sample}}}{I_i^{\mathrm{pure}}} \tag{3.3}$$

The MC algorithm simulates the X-ray spectra using a statistical approach that counts the photon interactions in the sample. With this approach, inhomogeneities of the sample, spectral and spatial distribution of the beam, polarization effects, photo-absorption, multiple fluorescence, and scattering effects can be considered more easily with respect to the FP method. Thickness gauging using the MC method with XRF is already reported in the literature; most of the reported works are in the field of cultural heritage applications [200–204]. In these cases, simulations are compared with the experimental measurement to confirm hypotheses based on bulk chemical composition, structural observations, and historical information.

The approach that I undertook differs from the state of the art in the sense that the simulations are used to build a calibration curve to determine the thickness of the coating. The same calibration curve could be used for many samples instead of performing many simulations based on hypotheses. This concept will be particularly interesting for industrial applications in metal deposition factories. The simulations require a fast MC code and for this purpose I decided to use XMI-MSIM for his long history of improvements [205–210].

In this work I examined a single-layer sample of Au, Pd, Sn, and bronze on brass, using both certified single-element coatings and electroplated alloys. The results were compared with other techniques for data validation: FP, FP + single empirical point, and scanning electron microscopy equipped with a

focused ion beam (FIB-SEM). This is expected to provide an analytical method to determine the thickness of coatings that does not make use of standards and whose performance is comparable to or even better than that of XRF analysis with energy-dispersive (ED-XRF) systems on metallic coatings.

3.3.1 Samples Preparation and Methods

The chosen substrate consisted of 3.75 × 5 mm^2 brass (copper–zinc 63:37 alloy) plates, 0.25 mm thick. The substrate was electroplated with palladium and gold using commercial galvanic baths "720 PDFE MPM" and "8693 MUP" from Bluclad srl (Prato, Italy) and bronze bath "SCUDO BIANCO PLUS RACK" from MacDermid (Waterbury, CT, USA). The alloy composition and layer thickness of the coatings were the subject of this study, and thus they will be discussed later. Certified samples with known thickness were also used and were provided by Bowman (Schaumburg, IL, USA).

XRF measurements were performed with a Bowman B Series XRF spectrometer (Schaumburg, IL, USA) using an acquisition time of 60 s, 50 kV tube voltage, 0.8 mA tube current, and a collimator of 0.305 mm in diameter. The same spectra were used to obtain the thickness information with various methods: FP, FP with one empirical point correction (both available with the commercial software of the instrument), and the MC method proposed in this study.

The composition of the substrate and the coatings were measured with energy-dispersive X-ray spectroscopy (EDS) microanalysis, applying an accelerating voltage of 20 kV and scanning an area of approximately 0.1 mm^2

for a live time of 120 s. In order to consider the matrix effect, the ZAF correction algorithm (atomic number, absorption, and fluorescence) was used for quantification. For this purpose, a gold-plated, palladium-plated, and bronze-plated sample were prepared, whose thicknesses were high enough to be considered infinite for the EDS analysis. The EDS analysis was performed with a Hitachi S-2300 (Tokyo, Japan) equipped with a Thermo Scientific Noran System 7 detector (Waltham, MA, USA) and analysed with Pathfinder software (version 2.1) [198].

The SEM images and the FIB ablation were performed with a GAIA 3 equipped with a Triglav electron column and a Gallium FIB Cobra Gallium column manufactured by Tescan (Brno, Czech Republic).

XRF spectra simulations were performed with the open-source software XMI-MSIM v7.0 64-bit by Schoonjan et al. [189], which predicts the spectral response of ED-XRF using MC simulations. The software allows for setting many variables of the system under investigation as well as the hardware geometry: this information was used as an input to simulate the spectra.

3.3.2 Spectra Simulation Software

The applicability of the proposed method is strongly connected to the ability of the simulation software to provide good results; for this reason, the accuracy and the reproducibility of XMI-MSIM were evaluated.

A parameter that affects the accuracy of the simulations is the number of interactions per trajectory: this number determines the maximum number of interactions that a photon can experience during its trajectory. Low values cause truncation errors, but too high values could result in a computationally

expensive simulation without any significant benefits. Simulation of 1 μm of gold coating on brass was performed using values from 1 to 10 as the number of interactions; the PR of each element for all the spectra was compared to the simulation with the highest number of interactions permitted, and the relative deviation was calculated (Figure 3.12a). The results show an exponential improvement for the first four interactions then, by increasing the number of interactions, the deviation remains stable around 0.001 %: for this reason, all the following simulations were performed using four interactions per trajectory. The time needed for each simulation was approximately 6 minutes using an ordinary personal computer (CPU i5 3.3 GHz, RAM 4 GB).

The precision of the simulated spectra was evaluated by repeating the same simulation on samples consisting of 1 μm of gold on brass substrates for 10 times. Then the deviation of the PR of each element from the mean value was calculated (Figure 3.12b) as well as the relative standard deviation, which is around 0.1 %.

After these tests, it can be concluded that the software results are good enough to allow its use in the study and to proceed with the following experiments.

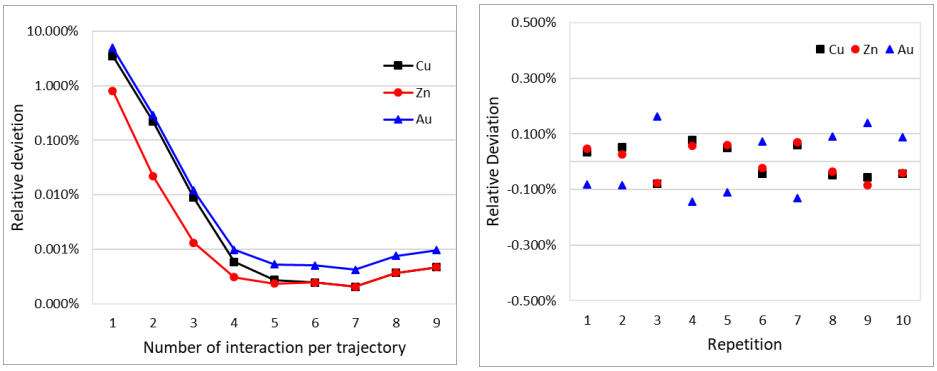

(**a**) (**b**)

Figure 3.12 – PRs of Cu, Zn, and Au of a simulated 1 μm of gold coating on brass substrates: (a) relative deviation of the PRs increasing the number of interactions with respect to the simulation with 10 interactions; (b) relative deviation from the mean value repeating the same simulation for 10 times.

3.3.3 XRF Simulations and Thickness Determination

The quantification method consisted in using the simulated spectra of five different layer thicknesses to build a calibration curve, which was used to extrapolate the unknown thicknesses of the measured samples. Simulations were performed using the exact composition of the coatings and the substrates that were measured with EDS. The spectrum of each pure element of interest (Cu, Zn, Pd, Sn, and Au) was also both measured and simulated to obtain the PRs.

XRF spectra were interpolated through multiple Gaussian [211–214] functions in the proximity of the energy lines of the expected elements to obtain the peak area. The considered peaks were Au Lα, Pd Kα, and Sn Kα; in addition, Cu Kα, Cu Kβ, Zn Kα and Zn Kβ were also fitted to avoid errors due to peak overlaps. The PRs were calculated, and the resulting data were fitted with a second-order curve. This kind of function is commonly implemented in XRF systems for industrial applications since it is in good

agreement with experimental data for a limited range of thicknesses and is also easy to manage. After the preparation of the samples, they were measured with the XRF, then the spectra of certified samples and the pure elements Au and Pd were collected. The FP method considers the all precious coating as pure for the thickness quantification. This method was used both alone and combined with a single empirical point. For the empirical point, the certified calibration standards were used.

A thick deposit of Au and Pd was electroplated separately (approximately 1.1 and 1.9 μm, measured with XRF) and measured with EDS to find the actual composition, reported in Table 3.5 together with the bronze sample, whose thickness was already high enough to be considered infinite with the EDS analysis. The composition of the certified thicknesses standards is known and is reported in Table 3.5 as well. The results are in agreement with the technical sheets of the baths; except the bronze that shows a level of Sn higher (47.2 %) than expected (28 % – 35 %), this information will be useful in the determination of the thickness.

Table 3.5 – The composition of the substrate and the films investigated using EDS analysis and of the certified data.

Samples	Electroplated	Certified
Brass (substrate)	Cu: 63.0 wt % Zn: 37.0 wt %	Cu: 63.0 wt % Zn: 37.0 wt %
Au	Au: 97.9 wt % Fe: 1.6 wt % Ni: 0.5 wt %	Au: 100 wt %
Pd	Pd: 95.2 wt % Fe: 4.8 wt %	Pd: 100 wt %
Bronze/Sn	Cu: 39.9 wt % Zn: 12.9 wt % Sn: 47.2 wt %	Sn: 100 wt %

The Monte Carlo simulations were performed with an accelerating voltage of 50 kV; for the composition of the substrate and the coatings that one provided by the microanalysis was used, the density was calculated considering an ideal mixture; over the sample a layer of 2.3 cm of air (0.0124 % C, 75.5268 % N, 23.1781 % O, 1.2827 % Ar mass fraction and 0.001205 g/cm^3 density) was added to simulate the real condition of measurement. The standards were simulated with the following parameters:

- 0.1, 0.5, 1.0, 1.5, 2.0 μm thick in the case of Au, Au alloy, Pd, Pd alloy and Sn.
- 0.10, 0.75, 1.50, 2.25, 3.00 μm thick in the case of the bronze alloy.
- Au, Pd, Sn thick (1 cm) pure elements.

The total number of simulations was 33 (Figure 3.13). The number of photons per interval was set to 10^4 and the number of photons per discrete

line was 10^5. The same geometry and emission spectra of the instrument used for the measurements were imposed in the simulations.

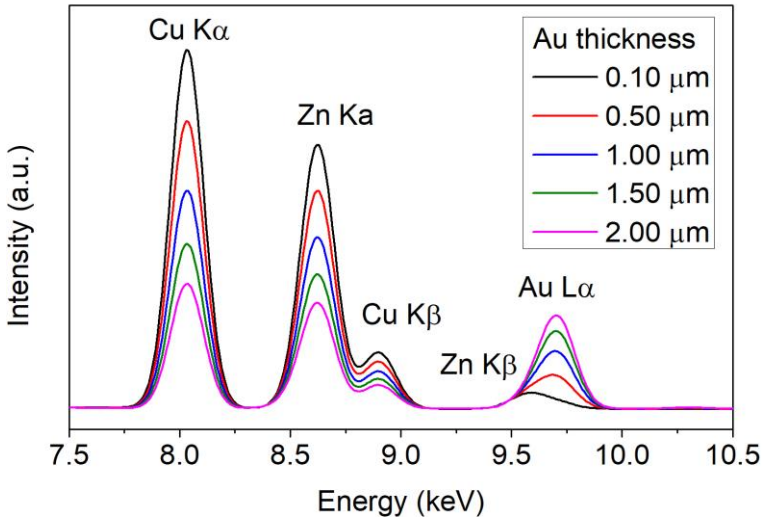

Figure 3.13 – Example of the output spectra obtained for the simulations of Au films on brass substrate.

The intensities of the peaks were integrated using a multiple Gaussian peak fit. The PRs were fitted with a second-order curve obtaining six calibration curves (Figure 3.14) with an $R^2 > 0.9999$. The peak intensities in the measured spectra were fitted with the same multiple Gaussian curves to calculate PR values and find the thickness of the samples.

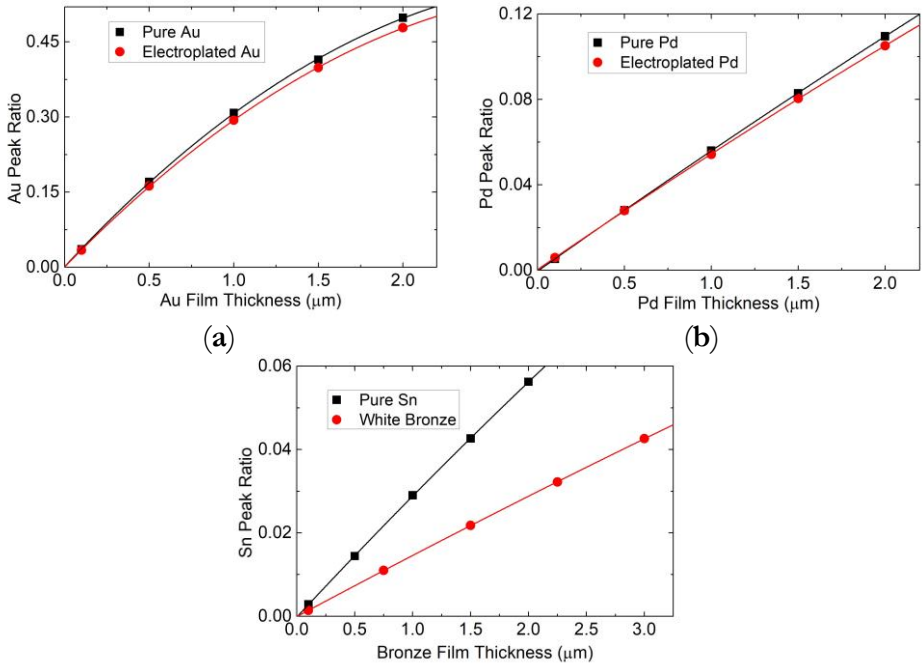

Figure 3.14 – Calibration curves built from the simulations using the pure metals (black) and the composition of the electroplated films (red) of (a) Au, (b) Pd, and (c) Sn.

The thickness of the electroplated sample was measured with FIB-SEM performing a semi-destructive micro-cross section (Figure 3.15). Using this kind of instrumentation, the possible mistakes due to sample preparation have been minimized.

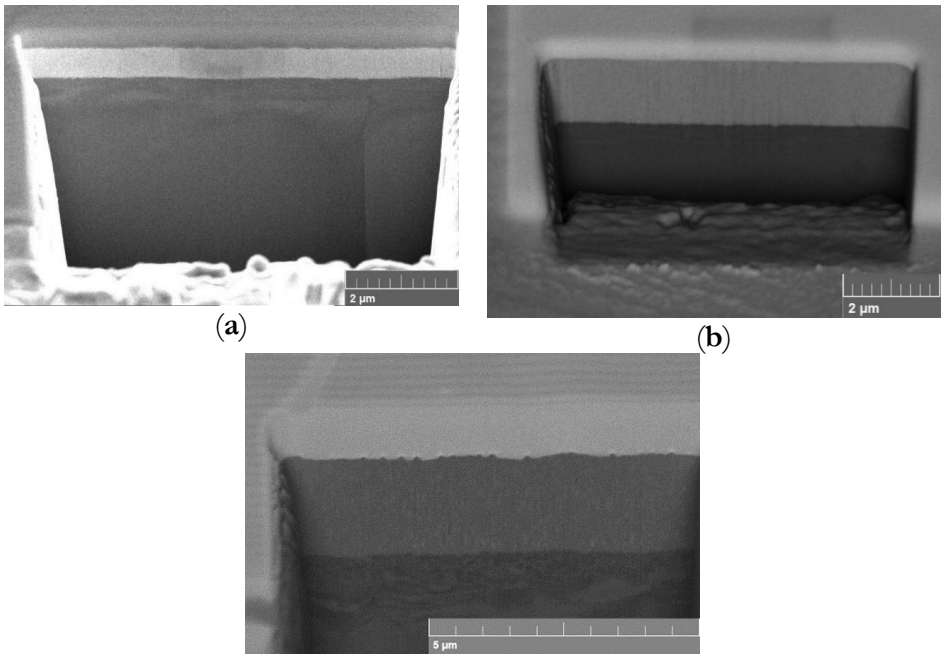

Figure 3.15 – FIB-SEM images of the electroplated samples: (a) gold; (b) palladium; (c) bronze.

The thicknesses obtained with the various techniques are summarized in Table 3.6. A large discrepancy in all the samples between the nominal value and the FP method is evident; this deviation is highly improved with the empirical correction. Keeping in mind that the certified samples were also used as standards for the empirical correction, the good results obtained for the certified samples are not very surprising; moreover, the result in the case of the electroplated samples are improved but still with an high accuracy error. On the other hand, the results obtained with the MC method are very promising: the estimated difference with respect to the nominal value is below 2 % in four out of six cases, and for two samples the difference (0.0 %) is under the precision of the measurements. The mean deviation between the six samples results and the nominal values was 4.3 %. For the cases of electroplated palladium and bronze the deviation is higher, around 5 %, but

they are still better than the FP result. The causes that produce these outliers will be studied more deeply in the future, but we can advance hypotheses based on what we observed during the integration process of the peaks. The Sn and Pd peaks are not very intense, due to the characteristics of the samples and the detector; in these cases, the signal-to-noise ratio was not very high, and for the same reason the matrix effect and the background subtraction are important factors that must be taken into consideration for accurate quantification.

Table 3.6 – Nominal (certified and FIB-SEM) and measured (XRF) thickness calculated with FP and MC methods for the samples.

		Experimental					
Samples	**Nominal**	**FP (µm)**	**Difference (%)**	**FP + Empirical (µm)**	**Difference (%)**	**MC (µm)**	**Difference (%)**
	Certificated (µm)						
Au	1.07	0.77	−28.0	1.07	0.0	1.08	+0.9
Pd	1.02	0.82	−19.6	1.01	−1.0	1.02	0.0
Sn	2.08	1.42	−31.7	2.01	−3.4	2.04	−1.9
	SEM (µm)						
Au alloy	0.53	0.28	−47.2	0.39	−26.4	0.53	0.0
Pd alloy	1.30	1.15	−11.5	1.40	+7.7	1.23	−5.4
Bronze	1.76	1.31	−25.6	2.01	+14.2	1.85	+5.1

The fitting of the calibration curve is good enough that, if repeated by considering only three of the five simulated spectra, the variation will be only

approximately ± 0.3 %, meaning that, in the case in which this variation could be acceptable, the computational cost could be decreased substantially. On the other hand, we found that the film composition strongly influences the results: in Figure 3.14 there is an appreciable divergence, increasing the thickness, when using pure metal coating standards or the electrodeposited alloy, even if the composition varies only by a few percentage points. If pure standards were used for the quantification of the galvanic sample, the results would have a variation of up to 5 %. For instance, the result obtained from FP for the electroplated bronze with the expected Sn concentration in the alloy (35 %) it would have been 2.71 μm (54 % deviation from the real value); for this reason the EDS analysis was performed to obtain the exact compositions. Unfortunately, in the industries it is often assumed that the composition of the deposit does not change much over time, leading to gross errors.

3.3.4 Prediction of Critical Parameters in the Measurement

In the previous section, it has been proved the power of the MC method for thickness determination. Then, more simulations were performed to predict the critical parameters that are important to be taken into account when a sample is measured, regardless of the measurement method used.

The first variable to be considered was the thickness of the substrate: on too thin samples, the X-rays could pass through, giving a PR different from what expected. To investigate this phenomenon, sandwich-like samples were simulated: the samples consisted in 0.5 μm pure gold coating on both sides (to mimic a real galvanic sample) and a brass layer in between, whose thickness ranged from only 1 μm up to 1 cm, one simulation per order of magnitude

was performed. The results are shown in Figure 3.16a, where the thickness was calculated considering an infinite substrate and the relative deviation was plotted. The influence of the thickness of brass substrates is evident only for very thin dimensions: over 0.1 mm, the difference with an infinite bulk substrate is negligible, and the same calibration curve can be used for different samples.

Later, the influence of the alloy composition was investigated, both in the case of the coating and the substrate. The typical deposits of common thickness used in the galvanic industry were examined: a 0.5 μm gold coating alloy, a 3 μm bronze coating alloy and brass alloys. The expected variation in the PR, when varying the composition of the alloys in a different layer, depends on the secondary fluorescence and self-absorption of the sample, which depend on the composition, meaning that for different elements the trend could be different.

A pure gold coating 0.5 μm thick on 1 cm brass substrate was simulated. Typical brasses are alloys of Cu and Zn in ratios ranging from 62:38 (UNS alloy number C27200) to 70:30 (C26130) [215]. The following concentrations of Cu were simulated: 63 %, 65 %, 67 %, and 69 %. In this range of concentrations, the resulting calculated thickness does not change significantly remaining in the error of the simulation (Figure 3.16b); the influence of the substrate could be more remarkable for higher differences in the composition or for different elements [216].

Then, the effect of the alloy composition of the coating was studied. First, it was investigated the Au–Cu alloy from pure gold to 18 kt (75 wt % Au) every 2 kt. The thickness was calculated considering the film as pure gold and then the result was corrected for the composition. In Figure 3.16c is evident

that the variation in thickness is bigger than the variation of gold concentration. These findings indicate that the results obtained with a not appropriated calibration curve cannot be corrected simply by using a multiplicative factor even if the composition is known; unfortunately, this practice is still mistakenly used in industrial quality control. For example, if an 18 kt gold sample is measured and the thickness is estimated with a 24 kt curve to be 0.5 μm, we cannot affirm that the actual thickness is 0.5 μm × 24 kt/18 kt = 0.67 μm since this would significantly underestimate the value.

The same study was carried out with a bronze alloy on brass. The typical galvanic bronze composition is 50 – 55 wt % Cu, 28 – 32 wt % Sn, and 14 – 20 wt % Zn. The calibration curve is typically built using a standard of pure Sn, and the results are multiplied by 3.33 (assuming 30 wt % of Sn in the alloy). In the simulated alloy the concentrations of Cu and Sn was varied, using Sn concentrations from 28 to 32 wt % every 1 %, keeping fixed the amount of Zn at 17%. The simulated sample consists of a 3 μm bronze top layer, a 5 μm Cu layer, and 1 cm of brass substrate: these thicknesses and layer combinations are typical of nickel-free electrodeposition for wearable accessories. The resulting deviation between estimated and effective thickness is reported in Figure 3.16d. Even in this case, similar to what we found for different alloys of gold, the composition plays a crucial role in the thickness determination, the variation over an interval of only four percentage points is not significative, but the absolute deviation is close to 12 %.

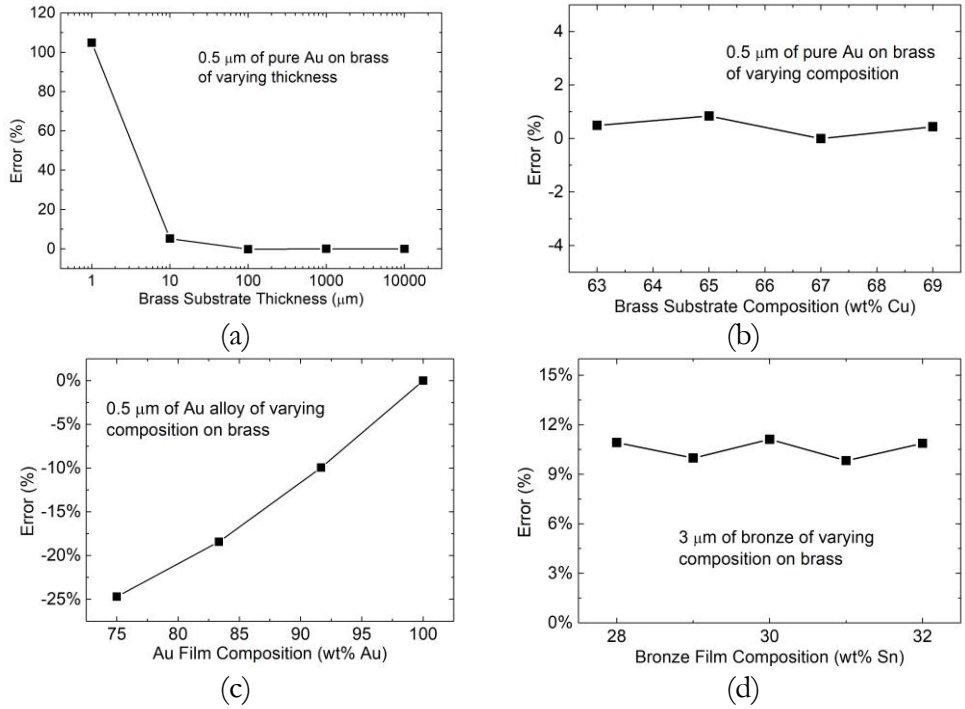

Figure 3.16 – Deviation in calculated thickness with respect to the real value of 0.5 μm gold film on brass simulation: (a) changing the thickness of the substrate; (b) changing the composition of the substrate (expressed in percentage of Cu); (c) changing the composition of the film, increasing the amount of Cu. (d) Deviation in calculated thickness with respect to the real value of 3 μm bronze film on brass, changing the composition of the film, increasing the amount of Cu.

4 Electrodeposition of Bi and Bi_2Se_3

In order to obtain an uniform deposit of bismuth and bismuth selenide on silver I initially studied the UPD conditions of bismuth on the silver substrate and on a layer of selenium; moreover, due to the nature of these materials, even the deposition of just a single ML could be technologically interesting. Then I moved to multiple cyclic depositions of MLs to achieve 3D structures, both maintaining the SLR deposition as well as exploring time-controlled and charge-controlled overpotential depositions.

4.1 UPD Investigations and Monolayer Depositions

4.1.1 Reagents and Characterization Techniques

The source of bismuth was a 0.5 mM solution of $Bi(NO_3)_3$ (Alfa Aesar, Haverhill, MA, USA) and 1 mM ethylenediaminetetraacetic acid disodium salt dihydrate ($EDTANa_2{\cdot}2H_2O$) (Alfa Aesar, Haverhill, MA, USA). EDTA was used as a ligand to form the complex with bismuth, increasing its solubility and prevent the precipitation of bismuth oxides [217,218]. The solution was prepared with MilliQ water (18 MΩ, Merck Millipore, Burlington, MA, USA) using a 0.1 M ammonium buffer pH = 9.13, obtained by mixing a NH_3 28% (Merck Millipore, Burlington, MA, USA) solution and a $HClO_4$ 65% (Carlo Erba, Cornaredo, Italy) solution. A 1 mM $EDTANa_2$ solution in ammonium buffer was also used as washing and stripping solution for bismuth. In the case of selenium stripping studies, a 0.1 M NaOH (Merck Millipore, Burlington, MA, USA) solution was used. The solutions were stored in Pyrex jars filled with nitrogen and connected to a cell through a circuit regulated by electro-valves. In order to flow the desired solutions inside the cell, an homemade automated deposition system [219], connected to a computer that

controls the dedicated electro-valves, has been used. The pressure in the jars was adjusted to achieve a solution flow rate of 1.5 mL/s. The electrolytic cell consisted in a Kel-F cylinder with a capacity of 1.88 mL. The working electrode was a silver (Ag)(111) monocrystalline electrode (0.785 cm^2) prepared and polished according to literature procedures [220–222]. The roughness of this electrode was investigated in previous studies from our group and measured as the root mean square (RMS): the surface can be considered as smooth, as the RMS roughness was found to be less than 3 nm [60,223]. Polycrystalline gold was used as a counter electrode and Ag/AgCl sat. KCl as a reference electrode.

XPS analysis was used to evaluate the composition of the deposit obtained under different electrochemical conditions. The instrument used for regular analysis makes use of a non-monochromatic X-ray source (VSW Scientific Instrument Limited model TA10, Manchester, United Kingdom), Mg Kα radiation (1253.6 eV), operating base at 120 W (12 kV and 10 mA) and a hemispherical analyser (VSW Scientific Instrument Limited model HA100, Manchester, UK). The analyser was equipped with a 16 channels detector and a dedicated differential pumping system that allows to work during the acquisition of pressure in the main chamber up to the 10^{-8} mbar range. The pass energy was set to 22 eV. XPS depth profiling analysis was performed on a PHI Versaprobe II spectrometer equipped with a monochromatized Al Kα source (1486.6 eV). Dual-beam charge neutralization was constantly applied during the analysis. A micro-spot size of 100 μm was used. XP spectra were recorded before sputtering and at different etching times (every 6 s) for a total time of 2 minutes for the complete process. Sputtering depth profile was performed with an Ar^+ gun (acceleration voltage = 1 KV, current = 1 μA) on a sample area equal to 2 x 2 mm^2. Binding energy

(BE) was referred to the $Ag3d_{5/2}$ component at 368.2 eV ascribed to Ag(111) substrate. The measured spectra were analysed using CasaXPS software [224] (version 2.3.19, Casa Software Ltd, Teignmouth, UK). The inelastic background was subtracted using Shirley's method [225] and a mixed Gaussian and Lorentzian contributions were used for each component. Calibration of the spectra was obtained by shifting to 284.8 eV, the lowest component relative to the 1s transition of carbon for adventitious carbon [226].

The morphology of the samples was investigated through a Hitachi S-2300 (Tokyo, Japan) and a Tescan (Brno, Czech Republic) GAIA 3 SEM equipped with EDS and BSE modules. AFM measurements were performed in contact mode with a Si_3N_4 triangular cantilever (Veeco, NP-S10) on a Molecular Imaging PicoSPM (Tempe, AZ).

The crystallinity of the deposit was characterized using the Cu K radiation of a Bruker (Billerica, MA) New D8 Da Vinci diffractometer, equipped with Ni filter, fast multichannel energy-discriminator detector, flat holder and Bragg-Brentano configuration to perform X-ray diffraction spectroscopy (XRD).

Optical anisotropy was evaluated using an optical microscope, equipped with a manual circular stage to rotate the sample under polychromatic light in the cross polarized light (CPL) configuration.

4.1.2 UPD of Bi on Ag

In order to find the UPD conditions of bismuth on silver the first step involved in performing a cyclic voltammetry (CV) of the bismuth solution on

the silver electrode from 0.00 V to -0.55 V with 2 mV/s scan rate. From the voltammogram (Figure 4.1) a well-defined peak at -0.36 V is evident, before the bulk deposition of bismuth which occurs at much higher potential, over -0.47 V. Even if the UPD is typical of metal/non-metal compounds in this case the best hypothesis is that the formation of an Ag/Bi alloy [227–229] is expressed with the presence of an underpotential deposition.

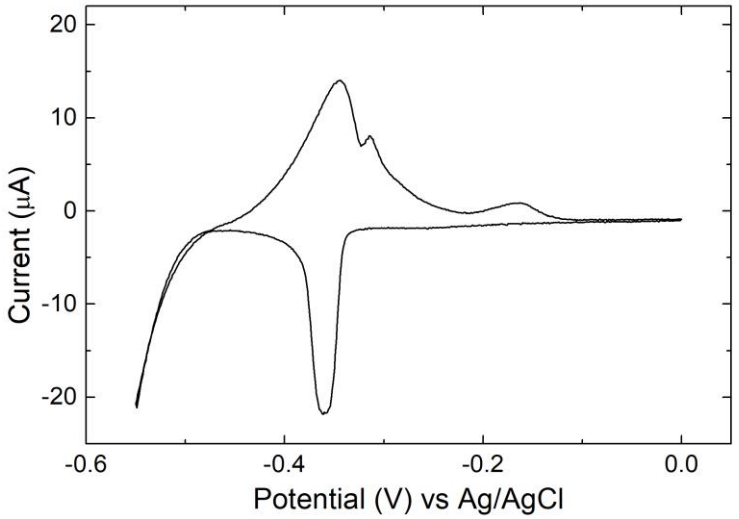

Figure 4.1 – CV of the bismuth solution on Ag(111) electrode between 0.00 V and -0.55 V, 2 mV/s scan rate.

The SLR study proceeded quantifying the amount of bismuth deposited in one minute as a function of the potential in proximity of the UPD peak, between -0.30 V and -0.55 V. After washing the electrode with EDTA, the bismuth deposit was stripped in the EDTA solution by a LSV from -0.50 V up to 0.00 V with a speed of 10 mV/s (Figure 4.2a). From the peaks obtained with the LSV, the deposited charge density was extrapolated (Figure 4.2b) by means of Equation (2.15). The voltammetries are reported "as measured" showing the current intensity, while the calculated charges have been

normalized for the electrode surface (0.785 cm^2) and reported as charge density.

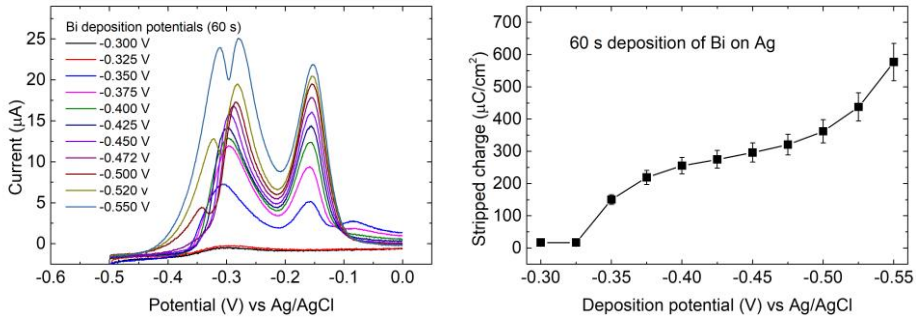

(**a**) (**b**)

Figure 4.2 – (a) LSV stripping (from -0.50 to 0.00 V, 10 mV/s scan rate) of bismuth deposited on Ag(111) at various potentials for 60 s; (b) Deposited charge density calculated from the stripping peaks.

The presence of a plateau at intermediate potentials confirms that what is shown in the CV was actually a SLR peak. Holding the potential fixed at -0.45 V, various depositions were performed by changing the deposition time followed by the LSV stripping (Figure 4.3a). Then the amount of charge deposited as a function of the deposition time was calculated (Figure 4.3b). The charge tends to grow in the first three minutes, confirming that the monolayer is formed relatively slowly (generally a few tens of seconds are enough) and, by applying a less negative potential, the growth is even slower. Over three minutes of deposition the amount of bismuth remains stable and reaches a plateau which indicates that bulk bismuth is not deposited.

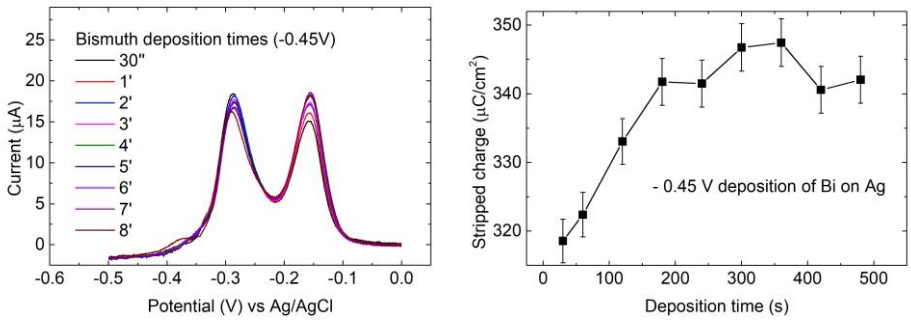

(**a**) (**b**)

Figure 4.3 – (a) Stripping LSV (from -0.50 to 0.00 V, 10 mV/s scan rate) of bismuth deposited on Ag(111) at -0.45 V for various times; (b) Deposited charge density calculated from the stripping peaks.

4.1.3 UPD of Bi on Se

In order to study the SLR deposition conditions of bismuth on selenium the Ag(111) electrode was initially covered with a monolayer of the non-metal [146]. Consecutive CV of selenium on Ag(111) are reported in Figure 4.4. The deposition of Ag/Se_{ad} (adlayer of selenium) consists in biasing the potential at −0.90 V for one minute in the presence of the selenite solution and then carrying out an ammonia buffer wash while maintaining the same potential for another minute. After covering the surface of the single crystal silver electrode with a selenium monolayer, a cyclic voltammetry of the $Bi(NO_3)_3$ solution is carried out (Figure 4.4). The presence of a reductive peak, even if small, that anticipates the massive deposition of the metal suggests the occurrence of a SLR.

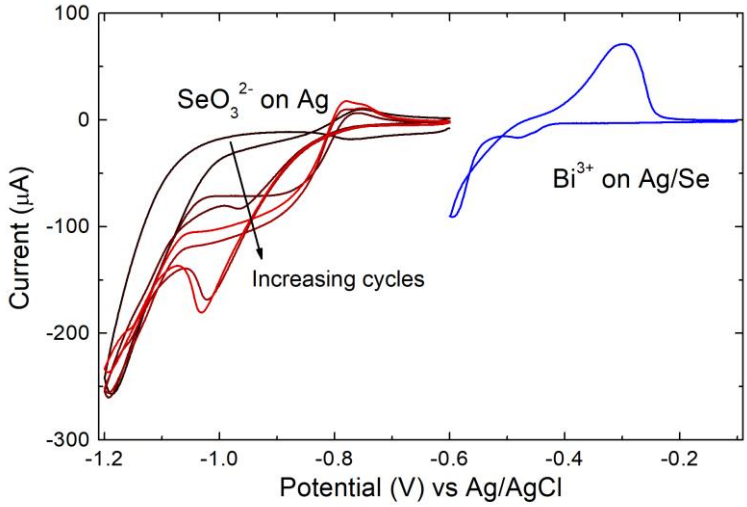

Figure 4.4 – On the left: 4 consecutive CVs of selenite (1st black – 4th red) between -0.60 V and -1.20 V, scan rate 50 mV/s. On the right: CV of the bismuth solution on Ag/Se_{ad} between -0.10 V and -0.55 V at 10 mV/s.

Successively, a systematic study was performed to find the best conditions for the SLR deposition of the metal. Bismuth depositions were carried out for one minute by varying the potential between -0.35 V and -0.48 V and then the deposit was anodically stripped in an EDTA solution to evaluate the actual deposited amount (Figure 4.5a). With increasingly negative stripping potentials, the charge increases, since the deposition time is not enough to deposit an entire monolayer of the metal, down to -0.42 V. However, at a potential more negative than -0.45 V, the charge grows very quickly indicating the onset of massive deposition. The optimal conditions for SLR deposition are most likely within the plateau between -0.42 V and -0.45 V. For further confirmation, the depositions were repeated at -0.43 V and -0.45 V by varying the deposition time (Figure 4.5b). While at -0.43 V the charge remained essentially constant after a deposition performed between 60 s and 120 s, at -0.45 V the deposit tended to grow, indicating a slow deposition

of massive bismuth. For this reason, -0.43 V represents the optimal potential for the SLR deposition of bismuth on selenium [230].

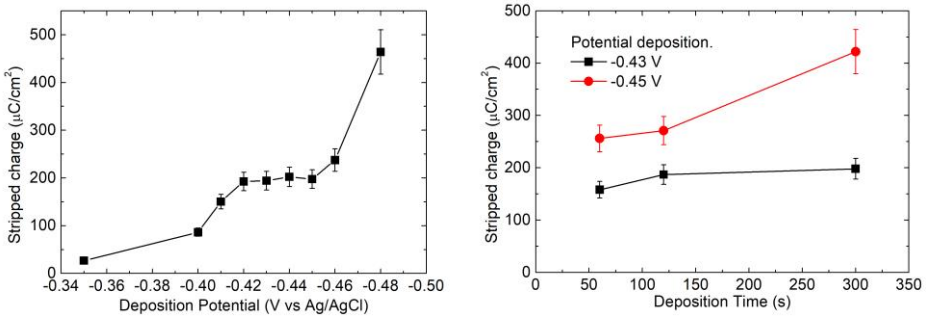

(**a**) (**b**)

Figure 4.5 – (a) Calculated charge growth of bismuth deposited in one minute on Ag/Se_{ad} as a function of the deposition potential; (b) amount of deposited bismuth with the potential fixed at −0.43 V (black) and −0.45 V (red) as a function of the deposition time.

4.2 Multilayer depositions

After the best deposition conditions of a ML of bismuth on silver and a ML of bismuth on selenium were achieved, a multilayer deposition with the E-ALD technique was tested, alternatively depositing bismuth and selenium to form bismuth selenide. Successively, in order to obtain a deposit of bismuth alone, SEBALD method, selenium electrodesorption from bismuth selenide, and overpotential charge-controlled deposition of bismuth were explored.

4.2.1 Multilayer Deposition of Bi/Se on Ag

Once the SLR conditions have been verified for both selenium and bismuth, several cycles were performed to obtain a deposit thicker than a single monolayer, following the procedure below:

- Se solution at -0.90 V for 60 s (growth of Se)
- Buffer solution at -0.90 V for 60 s (excess Se removal and rinse)
- Bi solution at -0.43 V for 60 s (growth of Bi)
- Washing with buffer solution (rinse)

A sample was prepared by performing 20 deposition cycles and then analysed by XPS (Figure 4.6). The peak related to the 4p transition of the silver substrate overlaps the Se 3d peak impairing the use of the latter to determine the amount of selenium in the sample. For this reason, both the regions of the 3d transition and 3s transition of selenium was acquired. The first feature was used to evaluate the chemical shift for the evaluation of the chemical state of this element and the second was used for its quantification. The quantification and evaluation of the chemical shift of bismuth was obtained using the 4f transition. In Figure 4.6a the absence of selenium was confirmed from XPS analysis in the region from 80 to 30 eV (Se 3d transition region). Only the Ag 4p transition was observed. In order to confirm this datum, no signal was observed in the region from 236 to 222 eV (Figure 4.6b Se 3s transition region). The 4f transition of bismuth was observed at 159 eV (Figure 4.6c), and this position is compatible with bismuth oxide (Bi_2O_3) [231,232]. The $Bi4f_{7/2}$ and $Bi4f_{5/2}$ peaks appear asymmetrical and for this reason two components (Bi and Bi ox) have been introduced to fit each peak [232]. These results show that the desired compound had not been formed and that the deposit had not grown as desired. This is not new, indeed there are other literature examples (e.g. InAs [144] and SnS_x [233]) in which, even if the precursors show a SLR, after a few cycles the growth spontaneously stops, impairing the formation of thin films. In such cases, this experimental evidence has been related to the intrinsic semiconductor nature, resulting in a

material with limited conductivity (increased ohmic drop) and therefore hindering electron transfer, or due to displacement by the applied deposition potential.

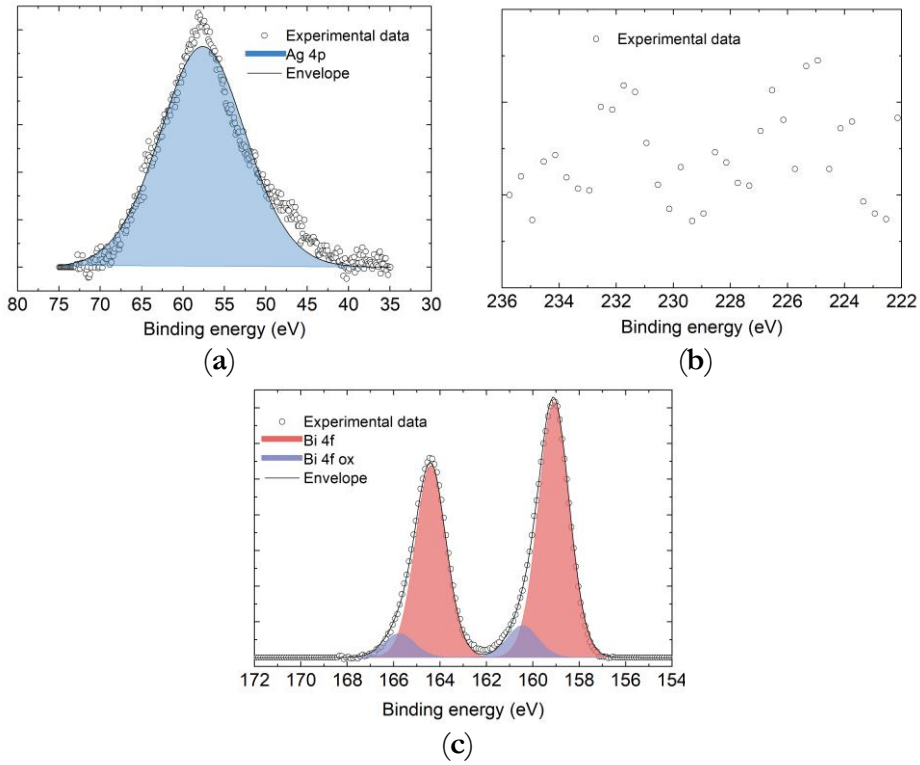

Figure 4.6 – XPS peaks of (a) 3d transition region of selenium (not present) and Ag 4p; (b) 3s transition region of selenium (not present) and (c) 4f transition region of bismuth in the sample prepared performing 20 deposition cycles.

To understand how the deposition process varies as a function of the number of cycles and why the expected quantity of selenium in the 20 cycles sample was not obtained, the stripping of multiple layers was performed (Figure 4.7a). It was found that after the first Se/Bi cycle, not only the quantity of selenium stopped growing, but it even decreased by a few fractions of monolayers (Figure 4.7b). On the other hand, the bismuth charge continued to grow, as if the limited presence of selenium was still enough to induce the

SLR of bismuth and enable formation of the subsequent layers, otherwise prevented due to the nature of SLR deposition.

This observation suggests a Selective Electrodesorption Based Atomic Layer Deposition (SEBALD)-like [79,83–85] mechanism. SEBALD is a method that allows the deposition of metal clusters or alloys under high morphological control. This technique consists of the E-ALD deposition of multiple layers of one or more metals alternated with an anion. The anion is then reduced and stripped out from the solid, leaving the metal deposit with shapes and/or composition not achievable with a conventional overpotential deposition. In this case, it seems that the SEBALD process occurs even if we want to avoid the chalcogenide electrodesorption. The morphology of this kind of deposit is crystalline, ordered and oriented as we demonstrated, with Atomic Force Microscope (AFM) and Scanning Electron Microscope (SEM) images, in a previous study [85].

The trend of the CVs of selenium on bulk bismuth (Figure 4.7c) is similar to that one observed on silver (Figure 4.4) but the current is much less and a broader peak is observed, suggesting sluggish deposition rate or disorder in the substrate. Assuming that the deposition conditions used for the deposition of the first selenium layer affect the subsequent layers, a potential of −0.90 V was applied to the deposit obtained after a single Se/Bi cycle in the presence of an ammonia buffer and then a stripping was carried out. Instead of obtaining the typical quantity of Se_{ad}, a much lower quantity was observed; it appears, thus, that it is the same deposition potential (−0.90 V) of the first selenium layer which, in the presence of Bi, selectively electrodesorbs the deposited Se, probably in the form of selenide (Figure 4.7a). A further

confirmation comes from the trial of depositing selenium on Ag/Bi_{ad} layer since there was no evidence of any SLR.

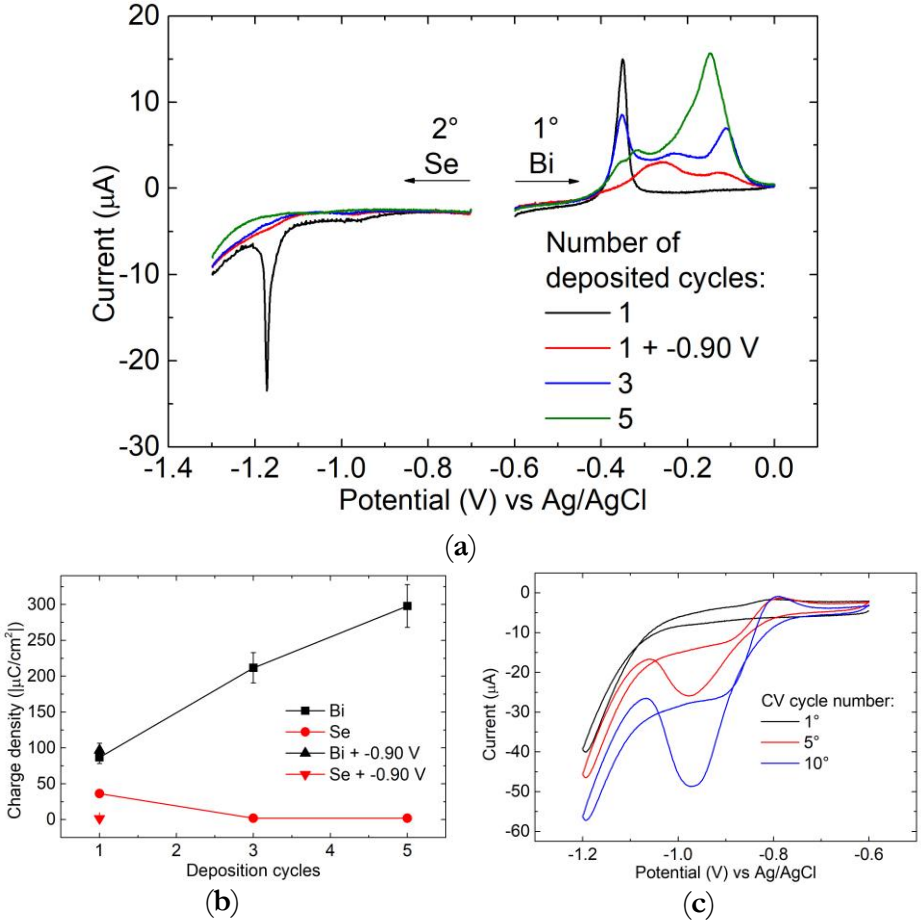

Figure 4.7 – (a) Stripping of the Se/Bi_n, with n equal to the number of the cycles performed (from 1 to 5), first removing the metal and then the non-metal element, 10 mV/s scan rate; (b) charge calculated by integrating the stripping curves; (c) consecutive CVs cycles of selenite on bulk Bi: 1st black, 5th red, 10th blue, 50 mV/s scan rate.

After performing further experiments, it emerged that, although it was not possible to deposit SLR layers of selenium on bismuth, the deposition of massive selenium remained unaltered and did not interfere with the already deposited underlying Se. This behaviour is probably due to the fact that bulk

selenium is deposited at a lower potential (-0.8 V), without occurring in the reduction and desorption of the underlying layers. In order to deposit an amount of massive selenium equivalent to the amount of a Se_{ad} it was found that the potential should be kept at -0.8 V for 3 min (time-controlled deposition) (Figure 4.8).

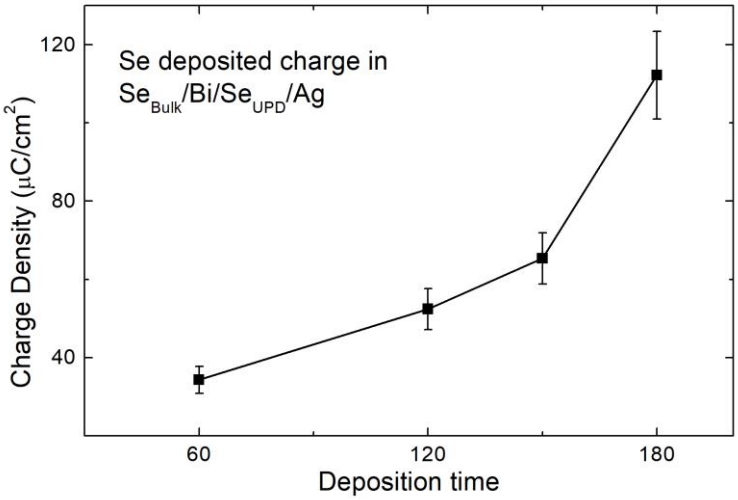

Figure 4.8 – Selenium stripped charge from Se_{Bulk}/Bi/Se_{UPD}/Ag. The Se_{Bulk} layer of selenium deposited at -0.80 V with various deposition times.

Deposits up to 10 cycles were thus performed and subsequent stripping confirms the presence of both elements (Figure 4.9a). From these measurements it was also calculated the Se:Bi ratio which is close to the stoichiometric value of 3:2 (Figure 4.9b). Slight variations are reasonably due to the uncontrolled nature of the time-controlled bulk deposition.

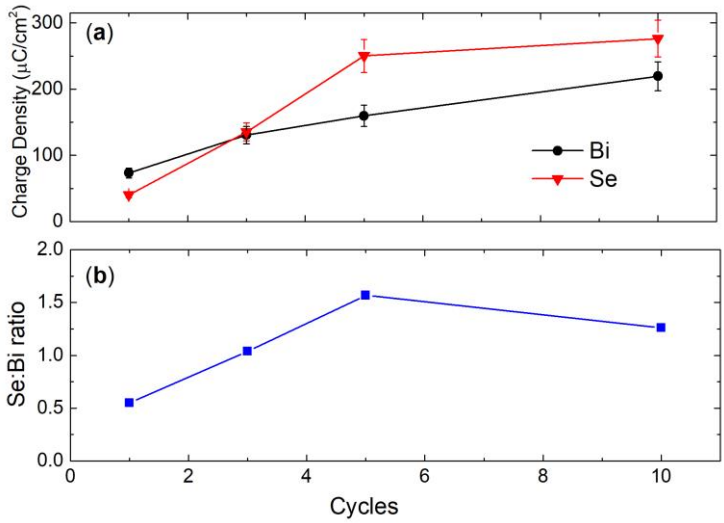

Figure 4.9 – (a) Stripped charge, from samples up to 10 layers, before of the bismuth (black) and then of the selenium (red); (b) ratio between the quantity of selenium and the bismuth (ideal: 1.5).

XPS measurements were also performed on a sample on which 20 cycles have been grown using the bulk selenium deposition method. In Figure 6 the presence of selenium is confirmed in both the regions. In particular, the peak relative to the 3d transition is well defined over the Ag 4p transition peak (Figure 4.10a), as well as in the 3s region (Figure 4.10b), and the position was determined at 53.6 eV, compatibly with the expected value for this element in selenide form [231,234]. The position of the 4f transition peak of bismuth was unchanged (Figure 4.10c) and was located at 159.3 eV, the energy is compatible also in this case with Bi_2O_3 [231,232] but is not excluded that it could be assigned to Bi_2Se_3 since the peak position of this two compound is similar [231,235,236]. The amount of bismuth and selenium in the sample was calculated from the XPS areas taking into account the atomic sensitivity factors [237] resulting in 42 % of bismuth and 58 % of selenium, compatibly with the stoichiometry (2:3) of the desired compound, and thus confirming the electrochemical results.

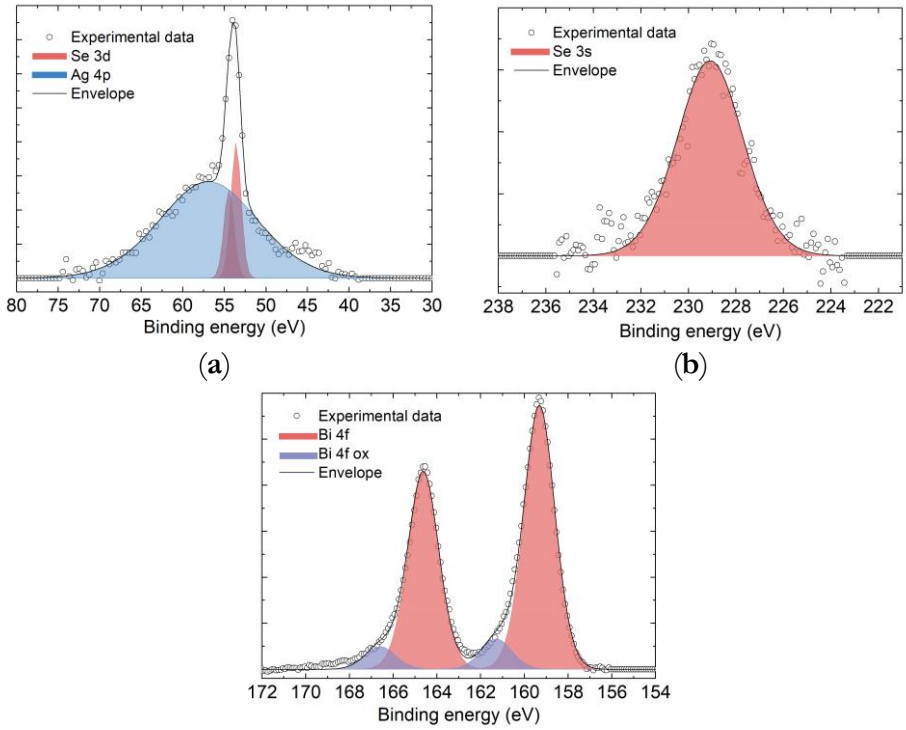

Figure 4.10 – XPS peaks of (a) 3d transition region of selenium and Ag 4p; (b) 3s transition region of selenium and (c) 4f transition region of bismuth in the sample prepared performing 20 deposition cycles with the time-controlled bulk selenium deposition method.

4.2.2 Multilayer Deposition of Bi on Ag Exploiting SEBALD

After having optimized the UPD conditions of bismuth and selenium a controlled multilayer deposition of bismuth was performed through the SEBALD procedure consisting in the sequential automatic alternate deposition of multiple cycles, obtaining a deposit of increasing thickness. After the deposition process, SEBALD was completed by setting the working electrode potential at -2.0 V and washing the cell in the buffer solution, in order to remove all the selenium previously deposited.

The deposition procedure was the same as previously used in the case of Bi_2Se_3, with the addition of the desorption step. Even if it was demonstrated that this process didn't work to form the compound, because selenium was not properly deposited, it was evident the growth of bismuth probably due to the limited presence of selenium.

- Se solution at -0.90 V for 60 s (growth of Se)
- Buffer solution at -0.90 V for 60 s (excess Se removal and rinse)
- Bi solution at -0.43 V for 60 s (growth of Bi)
- Buffer solution at -2 V (Se removal)
- Washing with buffer solution (rinse)

Anodic stripping of the remaining bismuth confirmed its growth over the number of cycles performed (Figure 4.11). For the very first cycles, a typical rapid growth, due to interaction phenomena confined to the nanoscale, is present. After the fifth deposition cycle, the trend becomes linear.

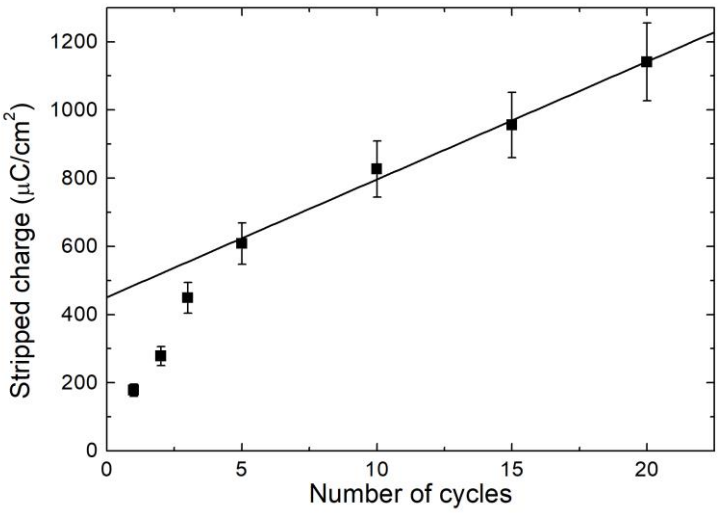

Figure 4.11 – Deposit growth according to the number of deposition cycles. After the first five cycles, the deposition rate becomes linear. Inset shows the cyclic voltammetry of bismuth solution on Ag/Se in which is evident the cathodic UPD peak of the metal.

A sample obtained with the deposition of 50 cycles was morphologically characterized, revealing that this simple SEBALD process, performed at room conditions, allows to obtain a highly ordered and crystalline deposit, difficult to obtain with other techniques. From the SEM analysis (Figure 4.12a), it was possible to appreciate how the bismuth deposit obtained by SEBALD has reorganized into its typical crystalline shape [238], hard to obtain with direct bulk deposition. The EDS (Figure 4.12b) data confirmed the presence of bismuth metal on the silver electrode without any traces of selenium, diagnostic of a proper SEBALD. The AFM measurement confirmed the morphology (Figure 4.12c) and gave useful information on the surface topology: the estimated RMS roughness was of 5.06 nm only.

Finally, the quality of the bismuth thin film was quantified by XRD. In the scan reported in Figure 4.12d it is possible to notice the peak of the substrate (Ag(111)) and, more importantly, the peaks of bismuth thin film

corresponding only to (102) and (204) crystalline planes. This observation points out that bismuth grew with a preferential orientation and the samples behave like pseudo-single crystal. Moreover Bi(012) have interesting electronic properties and it is studied for the application in quantum computing [73,239], since small-thickness films exhibit a reduced density of states near the Fermi level, making it act less as a metal and more like an insulator.

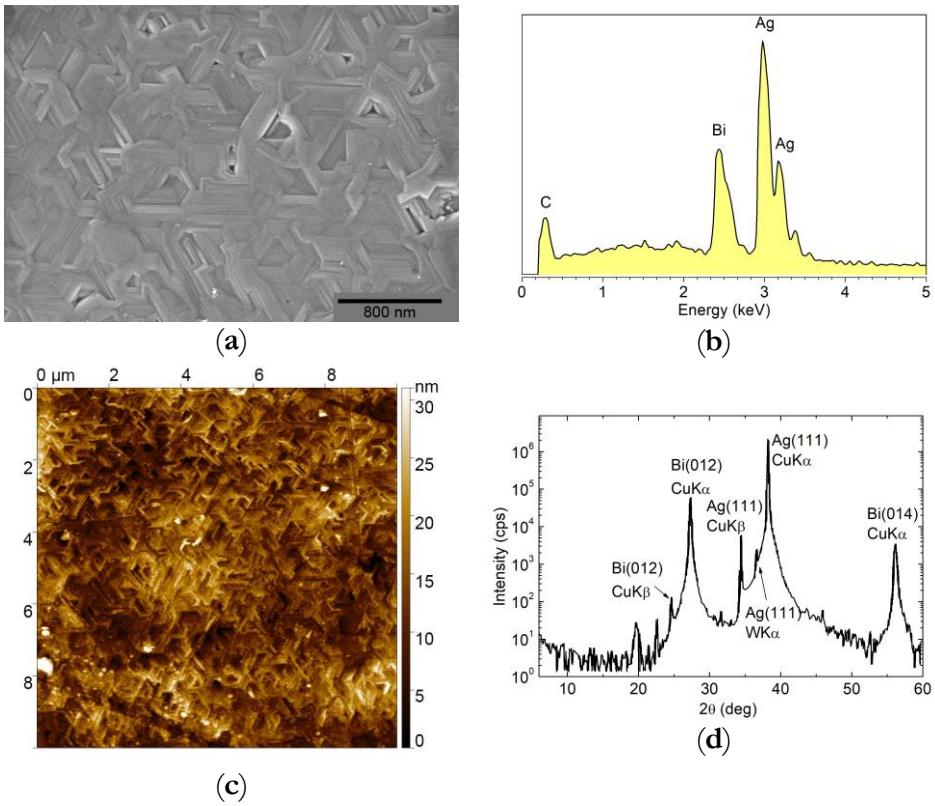

Figure 4.12 – (a) Secondary electrons SEM analysis of the 50 layers bismuth sample, showing the shape and morphology of the deposit. (b) EDS spectrum, with an accelerating voltage of 10 kV, that confirms the absence of selenium. (c) AFM image of the sample confirmed the morphology; (d) XRD measurement of the sample proved the crystallinity of the deposit.

4.2.3 Multilayer Deposition of Standalone Bi on Ag

The electrodeposition of multilayer bismuth was achieved with success through the SEBALD procedure, but it involved the presence of selenium to assist the deposition making it long and wasting a lot of solution. For this reason, the electrodeposition of standalone bismuth was investigated by means of charge-controlled deposition. The deposition of bismuth has been performed both in presence and in absence of an underlying UPD layer, which was obtained by applying a potential of -0.45 V for 3 minutes [130]. The atomic surface density of Ag(111) (cell constant 4.08 Å) is $1.39 \cdot 10^{19}$ atm/m^2, then the deposition of one ML on the electrode surface involves 665 μC/cm^2. The electrodeposited charge, estimated from the anodic peak, performing the UPD is 345 μC/cm^2 (Figure 4.3b), corresponding to a coverage of 0.52 ML when referred to a monolayer of Ag(111). The samples were prepared using a charge-controlled deposition by applying potential values from -0.45 V to -0.55 V in steps of 20 mV. The deposition charge was set to 400 μC for each deposition cycle and 30 cycles were performed for each sample, with a fresh $Bi(NO_3)_3$ solution injected into the cell at each cycle. The deposition charge value was set slightly over its nominal value to take into account the background current; moreover, the charge starts to be measured after 5 s to compensate the current of non-faradaic processes due to the switching of the potential or change of the solution, like capacitive effects. The deposition was faster for higher applied potentials (in absolute value), as the time needed to conclude the cycles decreases by increasing the potential value (Figure 4.13).

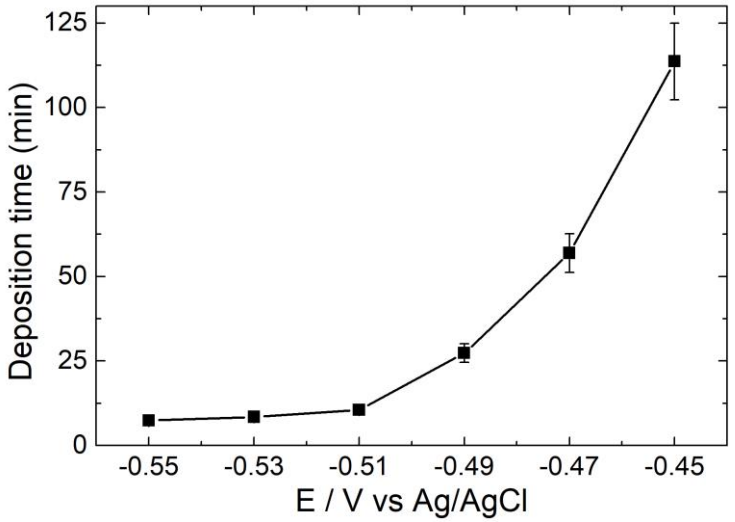

Figure 4.13 – Deposition time required to deposit 30 cycles of 400 μC of bismuth as function of the deposition potential.

After the deposition, the washing solution was fluxed in the cell and a potential of -0.7 V was applied to prevent the oxidation of the metal. The washing process was repeated five times, then the instrument was turned off, the sample extracted quickly and rinsed with MilliQ water; finally, it was dried under a nitrogen flow. The samples were stored in a desiccator for the subsequent analysis.

AFM analysis was performed at first, the 10 μm x 10 μm measured area of the samples is reported in Table 4.1. The samples growths under the lowest potentials (from -0.47 to -0.51 V), and subsequently the slowest ones, appear to be very similar to each other; moreover, the absence of the UPD layer does not seem to affect the morphology. The deposit shows a peculiar geometric and ordered structure, while the morphology is that typical of the hopper crystal of bismuth and appears very similar to those observed in a previous study by using the SEBALD method [85]. The nanocrystals are few tens of nanometres in height and 1 - 1.5 μm in length. The advantage of this method

over the SEBALD one is a faster deposition speed and the absence of the chalcogenide (selenium). For higher deposition potentials, -0.53 V and -0.55 V, the absence of the UPD layer is much more evident: the shapes mentioned before are completely lost and the deposit appears very messy and rough. On the other hand, the sample prepared by applying -0.53 V with the presence of the UPD layer is very similar to the previous ones as well as the sample prepared at -0.55 V, even if the edges of the nanocrystals are more elongated and sharper.

Table 4.1 – AFM images of the bismuth film growth in presence (left) of absence (right) of a previously deposited bismuth UPD layer on Ag(111) substrate. The deposition was performed by increasing the deposition potential, reported on the left, and by depositing the same total charge.

	Bi growth on UPD Bi layer	Bi growth directly on Ag
-0.47 V deposition	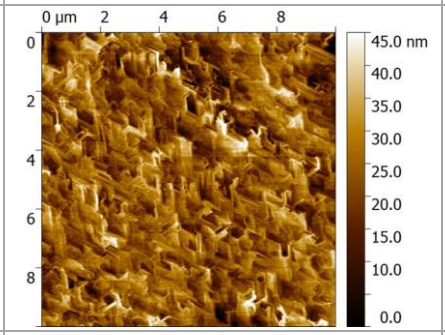	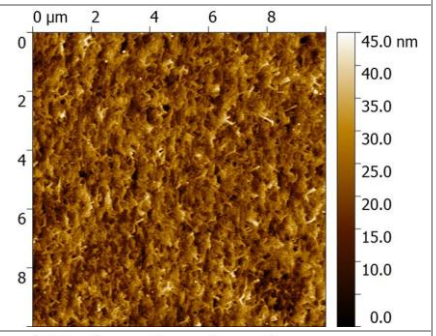
-0.49 V deposition	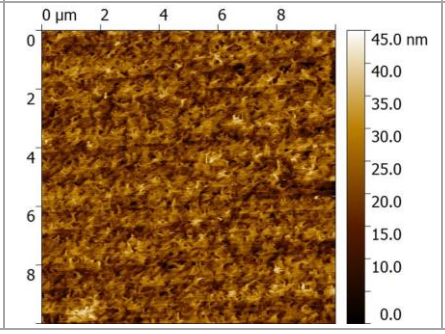	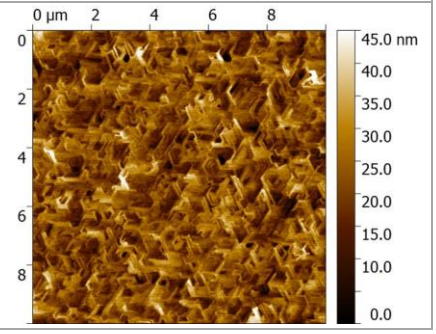

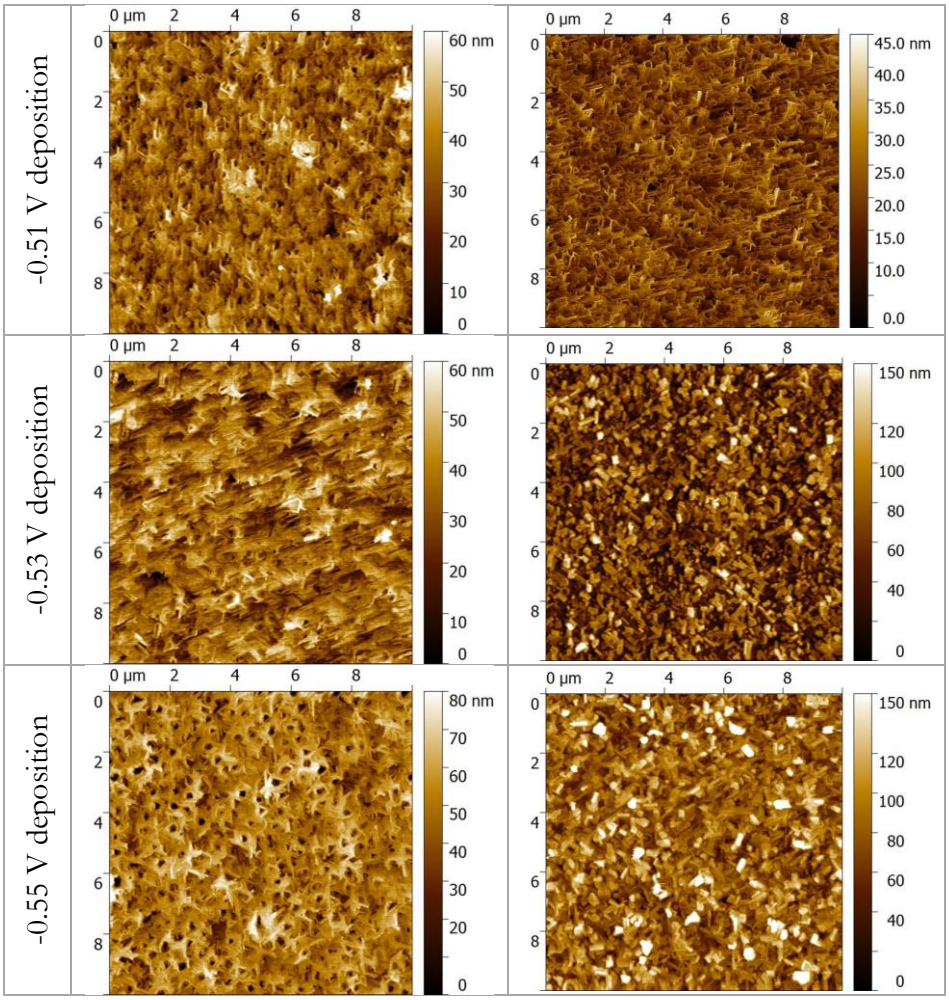

The smoothness of the samples was quantified by calculating the root mean square roughness (RMS), whose values are reported in Figure 4.14. The RMS of uncoated silver was also measured for comparison. For the sample prepared at -0.45 V, there was no difference in considering an underlying UPD layer or not, since this potential value corresponds to that of the UPD growth. The RMS values follow the trend already described above, since the samples with the UPD layer are quite similar one to each other with a low

RMS (i.e. a smooth deposit) that tends to increase slowly by increasing the absolute value of the growth potential; otherwise, in the absence of an UPD layer, there is a discontinuity on the RMS over -0.51 V, meaning that the deposit grows more randomly.

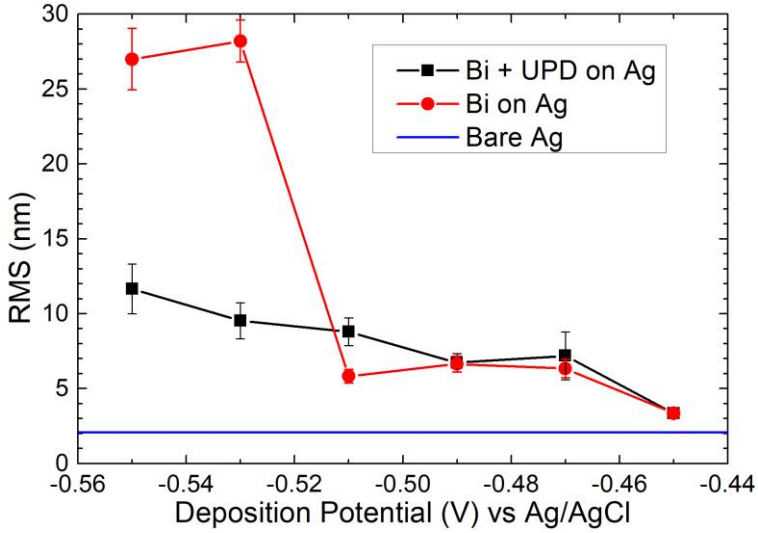

Figure 4.14 – Roughness, expressed as RMS, of the samples in presence (black) or absence (red) of a previously deposited bismuth UPD layer. The RMS value of the uncoated Ag(111) substrate (blue line) was reported for comparison.

The best deposit, considering the compromise between smoothness and deposition speed, turns out to be the one prepared at -0.55 V with the UPD layer, from now on named sample A. A further characterization was made with XRD; the sample prepared at -0.55 V without the UPD layer, named sample B, was also measured for comparison. The XRD analysis (Figure 4.15) did not highlight differences between the two samples. Both the spectra showed the presence of only three peaks, which have been associated to the monocrystalline Ag(111) substrate (38.12°), to Bi(012) (27.17°) and to Bi(024) (56.03°), respectively. This result points out that, like in the case of the deposit with the SEBALD method, the nanocrystals grew with a preferential orientation and the samples behave like pseudo-single crystal (012) which

owns interesting electronic properties for its intermediate behaviour between a metal and more like an insulator [73,239]. To evaluate if the crystallinity of the bismuth film was influenced by the crystallinity of the substrate, a sample was prepared according to the procedure of sample A but using Ag(100) as substrate (sample C). Even changing the crystallinity of the substrate, the bismuth deposit maintains the same crystallinity. The XRD analysis on sample C shows also that no other peaks of bismuth were hidden under the strong peak of Ag(111).

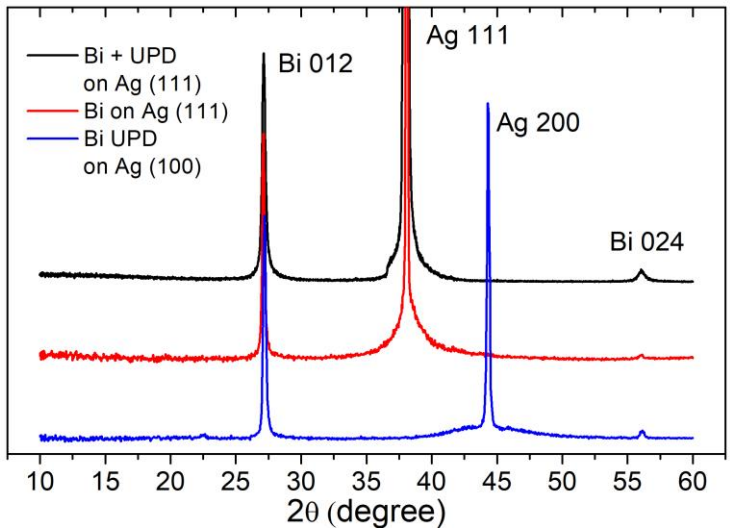

Figure 4.15 – XRD diffractograms of sample A (bulk bismuth deposited on bismuth UPD on Ag(111), in black), sample B (bulk bismuth deposited directly on Ag(111), red), sample C (bulk bismuth deposited on bismuth UPD on Ag(100),

The thickness of the sample A was evaluated as (55 ± 6) nm from the measured EDS spectra, assuming the surface as flat, through Monte Carlo simulations [193,240]. This result is coherent with the order of magnitude of the peak-to valley values given by the AFM analysis.

XPS destructive depth profiling was also performed to evaluate the composition of sample A. Survey and high-resolution spectra were acquired

at pass energy values of 117.4 and 58.7 eV and energy steps of 1.0 and 0.125 eV, respectively. High resolution regions relevant to C1s, O1s, Ag3d, Bi4f were investigated. As it was expected, carbon, oxygen, silver and bismuth were detected on the surface, before starting the sputtering protocol. The chemical composition of the analysed film was evaluated at different etching times and is reported in Figure 4.16a. Adventitious carbon is rapidly removed after 6 s sputtering, whereas bismuth content starts increasing monotonically and reaches its maximum after 42 s etching; the bismuth layer is eroded almost completely in about 100 s. Bi4f signal can be deconvoluted with two distinct doublets associated to elemental bismuth and its oxide (Bi_2O_3); the main $Bi4f_{7/2}$ signal falls at 156.8 ± 0.2 eV for the metal and at 159.0 ± 0.3 eV for the oxide species [231,232,234] (Figure 4.16b). After the first sputtering cycle, the Bi(oxide)/Bi(metal) content ratio was 2.2, whereas it falls at 0.12 after 42 s. It can be inferred then that the inner layers are mainly composed (about 90 %) by bismuth in its elemental state and that the oxide is essentially due to the partial oxidation of the outer layer, which is directly exposed to air. In fact, no special storage conditions were adopted to preserve the sample in a controlled environment.

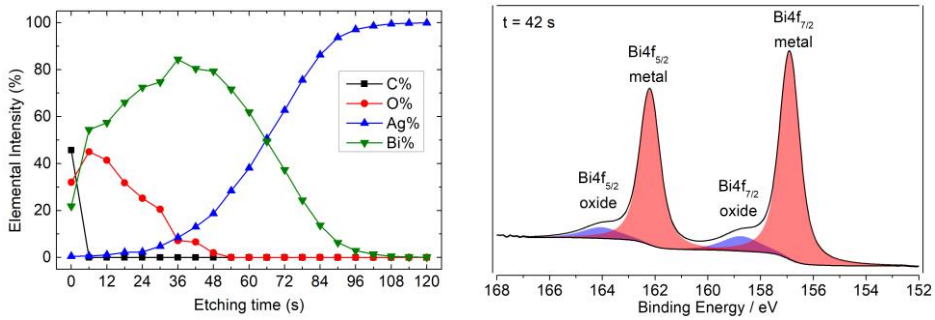

(**a**) (**b**)

Figure 4.16 – XPS depth analysis of sample A (bulk bismuth deposited on bismuth UPD on Ag(111)): (a) elemental composition reported as a function of the etching time; (b) Bi4f XP relevant region acquired after 42 s of sputtering time. The positions for the two oxidation states of bismuth are indicated.

Finally, CPL microscopy analysis was performed and it underlined an unexpected weak optical anisotropy [241–245] on all over the sample, which becomes strong in a couple of regions, whose size is of approximately a hundred microns and whose shape recalls a grain boundary (Figure 4.17a). The optical anisotropy was evaluated by using a rotating circular stage and acquiring photos of the sample every 10°, then, the mean grey value in the identified areas was measured. The results were normalized between the minimum and the maximum measured values and plotted in polar coordinates (Figure 4.17b). The polarization angles are relative to an arbitrary direction, while the maximum intensity was set to 0°. The intensities were fitted with good agreement with the Equation (4.1) [241].

$$I = a\sin^2(\theta+\varphi)\cos^2(\theta+\varphi) + b\cos^4(\theta+\varphi) \tag{4.1}$$

Where I is the light intensity, θ the relative rotation of the sample around the z axis, φ the phase and a and b are the weight coefficients for the two polarization components.

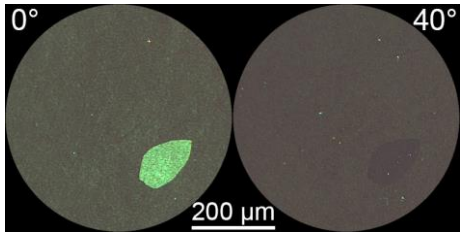

(**a**)

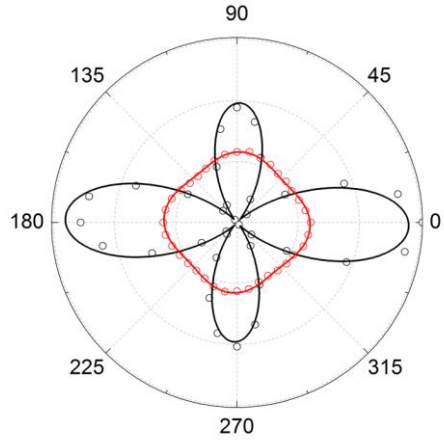

(**b**)

Figure 4.17 – (a) CPL image of the sample at 0° (left) and 40° (right) rotation respect to the normal axis; (b) polar plots of the normalized intensity measured with the CPL microscope of a bright zone (black) and the continuous bismuth film (red). The dots correspond to the measured data while the continuous lines represent the fitting curves.

To investigate more in deep the reason of this phenomenon, a SEM image was acquired right on the edge of a brighter zone (Figure 4.18). It is clear that the crystals in that region grew with a different orientation: for this reason it can be concluded that what it was observed was a form birefringence phenomenon [246–248], where the polarization of light is due to the shape of the nanocrystals and the anisotropy in the intensity is a consequence of the anisotropy in the morphology of the crystals in that specific region.

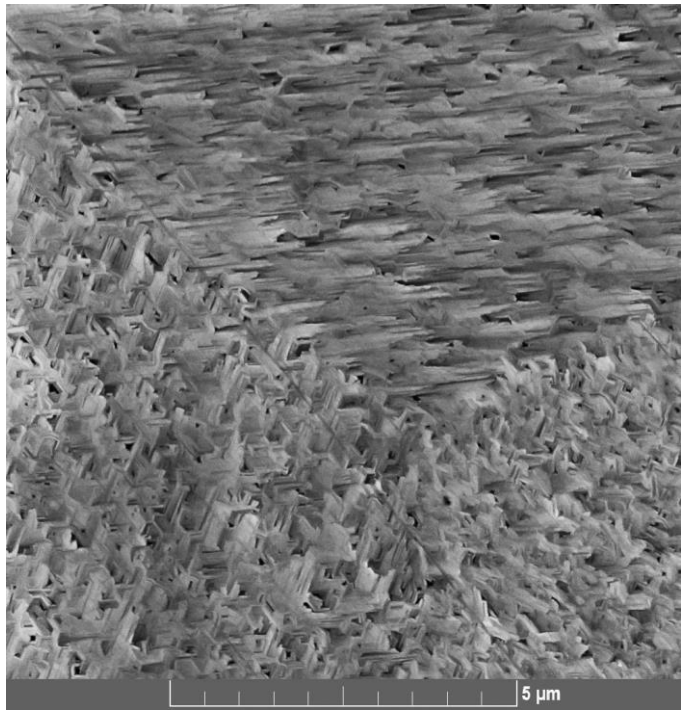

Figure 4.18 – SEM image of sample A. The upper part of the image corresponds to a bright zone and the lower part to the continuous bismuth film.

The form birefringence behaviour was confirmed by performing a punctual XRD analysis (Figure 4.19) in two zones with a different birefringence behaviour: the stronger birefringence in the small spots are produced by (110) crystals, probably formed because of defects in the substrate, which have a stronger anisotropy whit respect to the rotation on the vertical axis (Figure 4.19 insets).

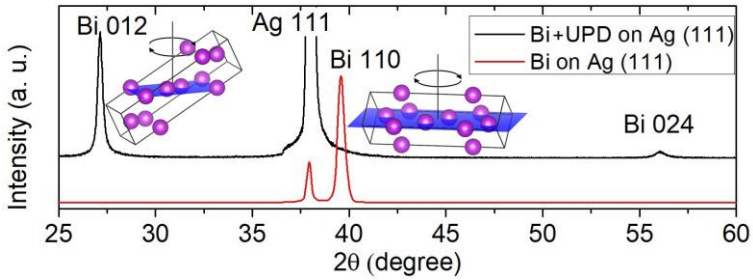

Figure 4.19 – punctual XRD analysis performed on the continuous film (black) and on a bright spot (red), the insets represent the unit cell and the relative plane of the measured peaks.

A similar phenomenon (changes in intensity due to the rotation of the sample on the z axis) was observed also by analysing the sample with SEM by means of the BSE analyser. There is no evidence of an angular anisotropy with the BSE imaging in literature. Even in this case, the phenomenon can be probably due to the shape of the nanocrystals, but more studies are to be done in this way.

5 Final Remarks

In this PhD thesis, I focalized my efforts on two distinct aspect of electrodeposited thin films: (i) an innovative standardless quantification method for the thickness determination of the films by means of MC simulations and (ii) the controlled deposition of bismuth and bismuth selenide exploiting low cost electrochemical methods. In both cases, the scientific and industrial interest is considerable since the promise of these techniques of characterization and deposition is to lower the production and analysis costs and at the same time to fabricate new technologically affable materials. At the end of this research I can assert that the obtained results were remarkable and could have interesting applications in the next future.

5.1 Monte Carlo Thickness Determination

A new quantification method for the determination of the thickness and the composition of electrodeposited precious metal thin films was presented. The first investigations were performed using EDS since this technique has better lateral resolution than XRF and allows reliable measurement on thin precious metal films with the capability to determine metals in the 1 % concentration range and thickness lower than 200 nm. The calibration curve was built entirely by using simulated spectra with low computational and instrumental cost. The time consumed to obtain a simulated standard it is lower than that employed for a real standard, the material costs are non-existent and it does not degrade over time. The approach was validated thereby with the analysis of three common electroplated metals (Au, Pd and Ni) with known thickness using various approaches and software. The results

were compared with other investigation techniques to evaluate its accuracy. Thickness results have an uncertainty of about 9 % which is consistent with the data from literature obtained from calibration curves using measured standards. The three metals chosen for the coating had largely different characteristic X-ray emissions as they had different atomic numbers. This shows that the method has a good versatility and can work properly for most of the coatings consisting of transition metals. The method has been proved to be effective by the analysis of a coating architecture consisting of a 24 kt topmost layer of gold, containing a tiny amount of nickel, deposited on a copper interlayer on brass substrate. The thickness result was in excellent agreement with the control measurement methods, with a deviation of 3.9 %. In addition, it was possible to determine the concentration of Ni in the gold top layer which was undetectable with the benchtop XRF thickness analyser. The final gold title was found to be 23.4 kt.

Then, the same quantification approach was adapted to XRF measurements, since XRF instrument is much more widespread and cheaper than EDS. Even in this case, the power of standardless MC calibration for measuring the thickness of metallic coatings was demonstrated. The proposed method was benchmarked with the use of certified standards and SEM imaging of FIB cross sections. The possibility of using this setup has considerably improved the quality of the measurements, compared to the previous study, in which the section was made with a hand polishing. The results indicate that the MC approach competes well with the FP method, which is the state of the art for the measurement of the thickness of metallic coatings in industry. The mean deviation between the results and the nominal values was approximately 4 %, below the typical accuracy of 5 % that a benchtop XRF provides using the standard-corrected FP method.

Remarkably, this result was achieved without the use of standards of known thickness and composition. The MC method has two major advantages: (i) the lack of standards allows for an easy switch between materials and coating architectures and (ii) it can easily adapt to existing XRF commercial systems as it only requires changes in the software. After proving that the simulations give reliable results, a few critical situations that may lead to major errors in the measurement both with the FP and MC methods was explored. It was found that in the investigated cases, small variations in the composition and the thickness of the substrate, or other eventual layers in multilayer architectures, do not play a substantial role in the thickness determination of the element on the top. Conversely, the composition of the substrate alloy must be known exactly, because even a small deviation from the known composition can lead to big errors in thickness quantification.

The proposed quantification method can be easily extended to any type of stratified sample, conductive or insulating; the only requirements are those typical of the techniques used: for EDS, the sample must not be electrically charged when submitted to the electronic beam and must be stable in vacuum conditions; for XRF, the lateral resolution must be in the order of millimetres. In this work the MC method has been used to investigate the thickness limited to a single layer on a substrate. The investigation of multilayer structures, introducing a multivariable approach, was already evaluated and it is currently in progress.

5.2 Bismuth Compounds Electrodeposition

The possibility to perform the controlled electrodeposition of one to multiple layer of bismuth and bismuth selenide was taken into consideration.

Initially, the possibility of depositing the metal under controlled conditions on bare silver single crystal and selenium coated Ag(111) was investigated, achieving a single Bi and Bi/Se monolayer. The SLR deposition of bismuth directly on silver was possible probably to the favourable formation of an alloy at a potential of −0.45 V, with the maximum charge deposited after 180 s. The UPD of bismuth on selenium occurs at -0.43 after 120 s.

Then I proceeded to synthesize the successive layers of the Bi_2Se_3 compound, but it has been observed that its growth was limited to the first monolayer applying the same conditions of UPD since there is not an UPD condition for the deposition of selenium on bismuth. For this reason, a time-controlled deposition was performed for selenium at its bulk potential (-0.80 V for 180 s) to achieve a 3D deposition of the compound. In this way, the deposition of both elements was obtained in the final sample, with the right 2:3 stoichiometry ratio.

A SEBALD-like behaviour was observed during the attempts of UPD of selenium on Bi/Se, for this reason an actual SEBALD was performed, stripping any residual selenium. In this way it was possible to grow an extremely ordered bismuth multilayers film with exquisite control on film thickness, as proven by the morphology of the resulting ultrathin films. Applying these results, it is possible to obtain ordered bismuth ultra-thin films, moreover the deposit was highly crystalline preferentially on the (012) plane, oriented and characterized by low roughness.

Finally, the deposition of bismuth films on an Ag(111) electrode was studied in absence of selenium by using a charge-controlled deposition and by applying an overpotential. The deposition was conducted both directly on the substrate as well as in presence of a UPD layer of bismuth before the bulk

deposition of the thin film, then the morphology of the samples was characterized. As expected for low overpotential values, and consequently slow deposition speeds, there are no significant changes of the morphology in presence or in absence of the UPD layer; nevertheless, for higher overpotential values and deposition rates, the UPD helps to maintain an ordered structure of the nanocrystals because the first layers are neatly deposited with fine control. Even with this kind of deposition, the film behaves as an oriented (012) single crystal, independently from the crystallinity of the substrate. The optical and electron microscopic characterizations highlight the anisotropy of the sample to polarized light and backscattered electrons with respect to the rotation on the normal axis: this phenomenon can be ascribed to the dimension and shapes of the crystals. These characteristics are suitable for the application of this compounds in electronic devices and for this reason it will be important in the future to better understand their electrical properties.

References

1. Wilkinson, A.D.; McNaught, A. *IUPAC. Compendium of Chemical Terminology, 2nd ed. (the "Gold Book")*; Blackwell Scientific Publications: Oxford, 1997; ISBN 0-9678550-9-8.

2. Union, I.; Pure, O.F.; Chemistry, A. Thin films including layers : terminology in relation to their preparation and characterization. *Electrochemistry* **1994**, *66*, 1667–1738.

3. Hasan, M.Z.; Kane, C.L. Colloquium: Topological insulators. *Rev. Mod. Phys.* **2010**, *82*, 3045–3067.

4. Th., L.; H., S.; M., Z.; S., S.; B., W. Status quo und Trends der Galvanotechnik. *Materwiss. Werksttech. 39*, 52–57.

5. Future Market Insights Electroplating Market: Global Industry Analysis and Opportunity Assessment, 2016–2026 Available online: https://www.futuremarketinsights.com/reports/electroplating-market.

6. Katz, L.; Penfold, A.S. Range-energy relations for electrons and the determination of beta-ray end-point energies by absorption. *Rev. Mod. Phys.* **1952**, *24*, 28–44.

7. Cockett, G.H.; Davis, C.D. Coating thickness measurement by electron probe microanalysis. *Br. J. Appl. Phys.* **1963**, *14*, 813–816.

8. Takahara, H. *Thickness and composition analysis of thin film samples using FP method by XRF analysis*; 2017; Vol. 33;.

9. Boehm, S.; Bügler, M.J.L. Layer Thickness Analysis of Thin Metal Coatings with micro-XRF on SEM. In Proceedings of the Bruker Nano Analytics, Berlin, Germany; 2017.

10. AXIC, I. *Non-Destructive Composition and Thickness Analysis of Metal Films Using Combination EDS/WDS X-Ray Fluorescence Spectrometry*;

11. Brouwer, P. *Theory of XRF - Getting acquainted with the principles*; 2010; ISBN 9090167587.

12. Malarde, D.; Powell, M.J.; Quesada-Cabrera, R.; Wilson, R.L.; Carmalt, C.J.; Sankar, G.; Parkin, I.P.; Palgrave, R.G. Optimized Atmospheric-Pressure Chemical Vapor Deposition Thermochromic VO2 Thin Films for Intelligent Window Applications. *ACS Omega* **2017**, *2*, 1040–1046.

13. Krumrey, M.; Gleber, G.; Scholze, F.; Wernecke, J. Synchrotron radiation-based x-ray reflection and scattering techniques for dimensional nanometrology. *Meas. Sci. Technol.* **2011**, *22*.

14. Serafińczuk, J.; Pietrucha, J.; Schroeder, G.; Gotszalk, T.P. Thin film thickness determination using X-ray reflectivity and Savitzky-Golay algorithm. *Opt. Appl.* **2011**, *41*, 315–322.

15. Osada, Y. Electron probe microanalysis (EPMA) measurement of aluminum oxide film thickness in the nanometer range on aluminum sheets. *X-Ray Spectrom.* **2005**, *34*, 92–95.

16. Bastin, G.F.; Heijligers, H.J.M. A systematic database of thin-film measurements by EPMA: Part I - Aluminum films. *X-Ray Spectrom.* **2000**, *29*.

17. Jablonski, A. Evaluation of procedures for overlayer thickness determination from XPS intensities. *Surf. Sci.* **2019**, *688*, 14–24.

18. Walton, J.; Alexander, M.R.; Fairley, N.; Roach, P.; Shard, A.G. Film thickness measurement and contamination layer correction for quantitative XPS. *Surf. Interface Anal.* **2016**, *48*, 164–172.

19. Demas, N.G.; Lorenzo-Martin, C.; Ajayi, O.O.; Erck, R.A.; Shareef, I. Measurement of Thin-film Coating Hardness in the Presence of Contamination and Roughness: Implications for Tribology. *Metall. Mater. Trans. A Phys. Metall. Mater. Sci.* **2016**, *47*, 1629–1640.

20. Anton; Paar Coating Thickness Testers Quick and Simple Determination of Coating Thicknesses.

21. ISO 26423:2009 Fine ceramics (advanced ceramics, advanced technical ceramics) — Determination of coating thickness by crater-grinding method. **2009**.

22. Nash, C.R.; Fenton, J.C.; Constantino, N.G.N.; Warburton, P.A. Compact chromium oxide thin film resistors for use in nanoscale quantum circuits. *J. Appl. Phys.* **2014**, *116*.

23. Lobo, R.F.M.; Pereira-da-Silva, M.A.; Raposo, M.; Faria, R.M.; Oliveira, O.N. In situ thickness measurements of ultra-thin multilayer polymer films by atomic force microscopy. *Nanotechnology* **1999**, *10*, 389–393.

24. Bardi, U.; Caporali, S.; Chenakin, S.P.; Lavacchi, A.; Miorin, E.; Pagura, C.; Tolstogouzov, A. Characterization of electrodeposited metal coatings by secondary ion mass spectrometry. *Surf. Coatings Technol.* **2006**, *200*, 2870–2874.

25. Bardi, U.; Chenakin, S.P.; Ghezzi, F.; Giolli, C.; Goruppa, A.; Lavacchi, A.; Miorin, E.; Pagura, C.; Tolstogouzov, A. High-temperature oxidation of

CrN/AlN multilayer coatings. *Appl. Surf. Sci.* **2005**, *252*, 1339–1349.

26. Hofmann, S.; Zhou, G.; Kovac, J.; Drev, S.; Lian, S.Y.; Lin, B.; Liu, Y.; Wang, J.Y. Preferential sputtering effects in depth profiling of multilayers with SIMS, XPS and AES. *Appl. Surf. Sci.* **2019**, *483*, 140–155.

27. Kalina, L.; Bílek, V.; Bušo, M.; Koplík, J.; Másilko, J. Thickness determination of corrosion layers on iron using XPS depth profiling. *Mater. Tehnol.* **2018**, *52*, 537–540.

28. Dange, S.N.; Saha, R.; Patade, A.M.; Mahadkar, A.; Pujara, D.T.; Vansutre, S. V.; Radha, S. Magnetoresistance of bismuth in bulk and thin film forms. In Proceedings of the AIP Conference Proceedings; 2014; Vol. 1591, pp. 1400–1402.

29. Tolutis, R.A.; Balevičius, S. Study of large magnetoresistance of thin polycrystalline Bi films annealed at critical temperatures. *Phys. status solidi* **2006**, *203*, 600–607.

30. Jiang, S.; Huang, Y.-H.; Luo, F.; Du, N.; Yan, C.-H. Synthesis of bismuth with various morphologies by electrodeposition. *Inorg. Chem. Commun.* **2003**, *6*, 781–785.

31. Cho, S.; Kim, Y.; Olafsen, L.J.; Vurgaftman, I.; Freeman, A.J.; Wong, G.K.L.; Meyer, J.R.; Hoffman, C.A.; Ketterson, J.B. Large magnetoresistance in post-annealed polycrystalline and epitaxial Bi thin films. *J. Magn. Magn. Mater.* **2002**, *239*, 201–203.

32. Yang, F.Y. Large Magnetoresistance of Electrodeposited Single-Crystal Bismuth Thin Films. *Science (80-.).* **1999**, *284*, 1335–1337.

33. Prakash, O.; Kumar, A.; Thamizhavel, A.; Ramakrishnan, S. Evidence for bulk superconductivity in pure bismuth single crystals at ambient pressure. *Science (80-.).* **2017**, *355*, 52–55.

34. Heremans, J.P.; Thrush, C.M.; Morelli, D.T.; Wu, M.-C. Thermoelectric Power of Bismuth Nanocomposites. *Phys. Rev. Lett.* **2002**, *88*, 216801.

35. Heremans, J.; Thrush, C.M. Thermoelectric power of bismuth nanowires. *Phys. Rev. B - Condens. Matter Mater. Phys.* **1999**.

36. Roberts, G.J.; Baird, P.E.G.; Brimicombe, M.W.S.M.; Sandars, P.G.H.; Selby, D.R.; Stacey, D.N. The Faraday effect and magnetic circular dichroism in atomic bismuth. *J. Phys. B At. Mol. Phys.* **1980**, *13*, 1389–1402.

37. Lenham, A.P.; Treherne, D.M.; Metcalfe, R.J. Optical Properties of Antimony and Bismuth Crystals. *J. Opt. Soc. Am.* **1965**, *55*, 1072.

38. Liao, A.D.; Yao, M.; Katmis, F.; Li, M.; Tang, S.; Moodera, J.S.; Opeil, C.;

Dresselhaus, M.S. Induced electronic anisotropy in bismuth thin films. *Appl. Phys. Lett.* **2014**, *105*, 063114.

39. Du, H.; Sun, X.; Liu, X.; Wu, X.; Wang, J.; Tian, M.; Zhao, A.; Luo, Y.; Yang, J.; Wang, B.; et al. Surface Landau levels and spin states in bismuth (111) ultrathin films. *Nat. Commun.* **2016**, *7*, 10814.

40. Hirahara, T.; Miyamoto, K.; Kimura, A.; Niinuma, Y.; Bihlmayer, G.; Chulkov, E. V.; Nagao, T.; Matsuda, I.; Qiao, S.; Shimada, K.; et al. Origin of the surface-state band-splitting in ultrathin Bi films: from a Rashba effect to a parity effect. *New J. Phys.* **2008**, *10*, 083038.

41. Meriuts, A.; Rogacheva, E.; Dresselhaus, M. On semimetal-semiconductor transition in thin Bi films. In Proceedings of the AIP Conference Proceedings; 2012; pp. 29–32.

42. Khvalkovskiy, A. V.; Cros, V.; Apalkov, D.; Nikitin, V.; Krounbi, M.; Zvezdin, K.A.; Anane, A.; Grollier, J.; Fert, A. Matching domain-wall configuration and spin-orbit torques for efficient domain-wall motion. *Phys. Rev. B* **2013**, *87*, 020402.

43. Hirahara, T.; Miyamoto, K.; Matsuda, I.; Kadono, T.; Kimura, A.; Nagao, T.; Bihlmayer, G.; Chulkov, E. V.; Qiao, S.; Shimada, K.; et al. Direct observation of spin splitting in bismuth surface states. *Phys. Rev. B* **2007**, *76*, 153305.

44. Kim, S.; Dong, W.J.; Gim, S.; Sohn, W.; Park, J.Y.; Yoo, C.J.; Jang, H.W.; Lee, J.-L. Shape-controlled bismuth nanoflakes as highly selective catalysts for electrochemical carbon dioxide reduction to formate. *Nano Energy* **2017**, *39*, 44–52.

45. Pierini, G.D.; Pistonesi, M.F.; Di Nezio, M.S.; Centurión, M.E. A pencil-lead bismuth film electrode and chemometric tools for simultaneous determination of heavy metals in propolis samples. *Microchem. J.* **2016**, *125*, 266–272.

46. Rehacek, V.; Hotovy, I.; Vojs, M. Bismuth Film Voltammetric Sensor on Pyrolyzed Photoresist/Alumina Support for Determination of Heavy Metals. *Electroanalysis* **2014**, *26*, 898–903.

47. Ping, J.; Wang, Y.; Wu, J.; Ying, Y. Development of an electrochemically reduced graphene oxide modified disposable bismuth film electrode and its application for stripping analysis of heavy metals in milk. *Food Chem.* **2014**, *151*, 65–71.

48. He, B.; Tian, G.; Gou, J.; Liu, B.; Shen, K.; Tian, Q.; Yu, Z.; Song, F.; Xie, H.; Gao, Y.; et al. Structural and electronic properties of atomically thin Bismuth on Au(111). *Surf. Sci.* **2019**, *679*, 147–153.

49. Kawakami, N.; Lin, C.-L.; Kawahara, K.; Kawai, M.; Arafune, R.; Takagi, N. Structural evolution of Bi thin films on Au(111) revealed by scanning tunneling microscopy. *Phys. Rev. B* **2017**, *96*, 205402.

50. Song, F.; Wells, J.W.; Jiang, Z.; Saxegaard, M.; Wahlström, E. Low-Temperature Growth of Bismuth Thin Films with (111) Facet on Highly Oriented Pyrolytic Graphite. *ACS Appl. Mater. Interfaces* **2015**, *7*, 8525–8532.

51. Yamada, K.; Souma, S.; Yamauchi, K.; Shimamura, N.; Sugawara, K.; Trang, C.X.; Oguchi, T.; Ueno, K.; Takahashi, T.; Sato, T. Ultrathin Bismuth Film on 1T-TaS 2 : Structural Transition and Charge-Density-Wave Proximity Effect. *Nano Lett.* **2018**, *18*, 3235–3240.

52. Camps, E.; Rodil, S.E.; Salas, J.A.; Estrada, H. V. A Detailed Study of the Synthesis of Bismuth Thin Films by PVD-Methods and their Structural Characterization. *MRS Proc.* **2012**, *1477*, imrc12-1477-s1a-o007.

53. Prados, A.; Ranchal, R. Electrodeposition of Bi Thin Films on n-GaAs(111)B. I. Correlation between the Overpotential and the Nucleation Process. *J. Phys. Chem. C* **2018**, *122*, 8874–8885.

54. Bilican, D.; Fornell, J.; Sort, J.; Pellicer, E. Electrochemical Synthesis of Bismuth Particles: Tuning Particle Shape through Substrate Type within a Narrow Potential Window. *Materials (Basel).* **2017**, *10*, 43.

55. Yang, M.; Hu, Z. Electrodeposition of bismuth onto glassy carbon electrodes from nitrate solutions. *J. Electroanal. Chem.* **2005**, *583*, 46–55.

56. Huang, X.; Plaza, M.; Ko, J.Y.P.; Abruña, H.D.; Brock, J.D. Relaxation of asymmetric crystallographic tilt: In situ x-ray diffraction studies of epitaxial electrodeposition of bismuth on GaAs (110). *J. Appl. Phys.* **2018**, *124*, 035301.

57. Loglio, F.; Innocenti, M.; D'Acapito, F.; Felici, R.; Pezzatini, G.; Salvietti, E.; Foresti, M.L. Cadmium selenide electrodeposited by ECALE: electrochemical characterization and preliminary results by EXAFS. *J. Electroanal. Chem.* **2005**, *575*, 161–167.

58. Cecconi, T.; Atrei, A.; Bardi, U.; Forni, F.; Innocenti, M.; Loglio, F.; Foresti, M.L.; Rovida, G. X-ray photoelectron diffraction (XPD) study of the atomic structure of the ultrathin CdS phase deposited on Ag(111) by electrochemical atomic layer epitaxy (ECALE). *J. Electron Spectros. Relat. Phenomena* **2001**, *114–116*, 563–568.

59. Cavallini, M.; Facchini, M.; Albonetti, C.; Biscarini, F.; Innocenti, M.; Loglio, F.; Salvietti, E.; Pezzatini, G.; Foresti, M.L. Two-Dimensional Self-Organization of CdS Ultra Thin Films by Confined Electrochemical Atomic Layer Epitaxy Growth. *J. Phys. Chem. C* **2007**, *111*, 1061–1064.

60. Innocenti, M.; Cattarin, S.; Cavallini, M.; Loglio, F.; Foresti, M.L. Characterisation of thin films of CdS deposited on Ag(111) by ECALE. A morphological and photoelectrochemical investigation. *J. Electroanal. Chem.* **2002**, *532*, 219–225.

61. Tishkevich, D.I.; Grabchikov, S.S.; Tsybulskaya, L.S.; Shendyukov, V.S.; Perevoznikov, S.S.; Trukhanov, S.V.; Trukhanova, E.L.; Trukhanov, A.V.; Vinnik, D.A. Electrochemical deposition regimes and critical influence of organic additives on the structure of Bi films. *J. Alloys Compd.* **2018**, *735*, 1943–1948.

62. Sandnes, E.; Williams, M.E.; Bertocci, U.; Vaudin, M.D.; Stafford, G.R. Electrodeposition of bismuth from nitric acid electrolyte. *Electrochim. Acta* **2007**, *52*, 6221–6228.

63. Jeffrey, C.A.; Harrington, D.A.; Morin, S. In situ scanning tunneling microscopy of bismuth electrodeposition on Au() surfaces. *Surf. Sci.* **2002**, *512*, L367–L372.

64. Wood, C. Materials for thermoelectric energy conversion. *Inst. Phys.* **1988**, *51*, 459–539.

65. Tumelero, M.A.; Faccio, R.; Pasa, A.A. Unraveling the native conduction of trichalcogenides and its ideal band alignment for new photovoltaic interfaces. *J. Phys. Chem. C* **2016**, *120*, 1390–1399.

66. Tumelero, M.A.; Benetti, L.C.; Isoppo, E.; Faccio, R.; Zangari, G.; Pasa, A.A. Electrodeposition and ab Initio Studies of Metastable Orthorhombic Bi2Se3: A Novel Semiconductor with Bandgap for Photovoltaic Applications. *J. Phys. Chem. C* **2016**, *120*, 11797–11806.

67. Ahmed, R.; Xu, Y.; Sales, M.G.; Lin, Q.; McDonnell, S.J.; Zangari, G. Synthesis and Material Properties of Bi2Se3 Nanostructures Deposited by SILAR. *J. Phys. Chem. C* **2018**, *122*, 12052–12060.

68. Chiatti, O.; Riha, C.; Lawrenz, D.; Busch, M.; Dusari, S.; Sánchez-Barriga, J.; Mogilatenko, A.; Yashina, L. V.; Valencia, S.; Ünal, A.A.; et al. 2D layered transport properties from topological insulator Bi 2 Se 3 single crystals and micro flakes. *Sci. Rep.* **2016**, *6*, 1–11.

69. Laforge, A.D.; Frenzel, A.; Pursley, B.C.; Lin, T.; Liu, X.; Shi, J.; Basov, D.N. Optical characterization of Bi2Se3 in a magnetic field: Infrared evidence for magnetoelectric coupling in a topological insulator material. *Phys. Rev. B - Condens. Matter Mater. Phys.* **2010**, *81*, 1–8.

70. Hor, Y.S.; Richardella, A.; Roushan, P.; Xia, Y.; Checkelsky, J.G.; Yazdani, A.; Hasan, M.Z.; Ong, N.P.; Cava, R.J. P -type Bi2 Se3 for topological insulator and low-temperature thermoelectric applications. *Phys. Rev. B -*

Condens. Matter Mater. Phys. **2009**, *79*, 2–6.

71. Zhang, H.; Liu, C.-X.; Qi, X.-L.; Dai, X.; Fang, Z.; Zhang, S.-C. Topological insulators in Bi2Se3, Bi2Te3 and Sb2Te3 with a single Dirac cone on the surface. *Nat. Phys.* **2009**, *5*, 438–442.

72. Yao, M.-Y.; Zhu, F.; Han, C.Q.; Guan, D.D.; Liu, C.; Qian, D.; Jia, J. Topologically nontrivial bismuth(111) thin films. *Sci. Rep.* **2016**, *6*, 21326.

73. Wada, M.; Murakami, S.; Freimuth, F.; Bihlmayer, G. Localized edge states in two-dimensional topological insulators: Ultrathin Bi films. *Phys. Rev. B* **2011**, *83*, 121310.

74. Drozdov, I.K.; Alexandradinata, A.; Jeon, S.; Nadj-Perge, S.; Ji, H.; Cava, R.J.; Bernevig, B.A.; Yazdani, A. One-dimensional topological edge states of bismuth bilayers. *Nat. Phys.* **2014**, *10*, 664–669.

75. Moore, J.E. The birth of topological insulators. *Nature* **2010**, *464*, 194–198.

76. Claro, M.S.; Levy, I.; Gangopadhyay, A.; Smith, D.J.; Tamargo, M.C. Self-assembled Bismuth Selenide (Bi 2 Se 3) quantum dots grown by molecular beam epitaxy. *Sci. Rep.* **2019**, *9*, 1–7.

77. Ginley, T.P.; Wang, Y.; Law, S. Topological insulator film growth by molecular beam epitaxy: A review. *Crystals* **2016**, *6*, 1–26.

78. Xiao, C.; Yang, J.; Zhu, W.; Peng, J.; Zhang, J. Electrodeposition and characterization of Bi2Se3 thin films by electrochemical atomic layer epitaxy (ECALE). *Electrochim. Acta* **2009**, *54*, 6821–6826.

79. Brankovic, S.R.; Zangari, G. Electrochemical Surface Processes and Opportunities for Material Synthesis. In *Advances in Electrochemical Science and Engineering*; Wiley-Blackwell, 2015; pp. 59–106 ISBN 9783527690633.

80. Innocenti, M.; Benedetto, F. Di; Giaccherini, A.; Salvietti, E.; Gambinossi, F.; Passaponti, M.; Foresti, M.L. E-ALD: Tailoring the Optoeletronic Properties of Metal Chalcogenides on Ag Single Crystals. In *Semiconductors*; Inguanta, R., Ed.; InTech: Rijeka, 2018.

81. Innocenti, M.; Bencistà, I.; Bellandi, S.; Bianchini, C.; Di Benedetto, F.; Lavacchi, A.; Vizza, F.; Foresti, M.L. Electrochemical layer by layer growth and characterization of copper sulfur thin films on Ag(1 1 1). *Electrochim. Acta* **2011**, *58*, 599–605.

82. Gregory, B.W.; Stickney, J.L. Electrochemical atomic layer epitaxy (ECALE). *J. Electroanal. Chem. Interfacial Electrochem.* **1991**, *300*, 543–561.

83. Innocenti, M.; Bellandi, S.; Lastraioli, E.; Loglio, F.; Foresti, M.L. Selective Electrodesorption Based Atomic Layer Deposition (SEBALD): a Novel

Electrochemical Route to Deposit Metal Clusters on Ag(111). *Langmuir* **2011**, *27*, 11704–11709.

84. Innocenti, M.; Zangari, G.; Zafferoni, C.; Bencistà, I.; Becucci, L.; Lavacchi, A. Selective electrodesorption based atomic layer deposition (SEBALD) modifications of silver surfaces for enhancing oxygen reduction reaction activity. *J. Power Sources* **2013**, *241*, 80–86.

85. Giurlani, W.; Giaccherini, A.; Salvietti, E.; Passaponti, M.; Comparini, A.; Morandi, V.; Liscio, F.; Cavallini, M.; Innocenti, M. Selective Electrodesorption-Based Atomic Layer Deposition (SEBALD) of Bismuth under Morphological Control. *Electrochem. Soc. Interface* **2018**, *27*, 77–81.

86. Castaing, R. Application of Electron Probes to Local Chemical and Crystallographic Analysis, Ph.D. Thesis, University of Paris, Paris, France, 1951.

87. Richter, S.; Pinard, P.T. Combined EPMA, FIB and Monte Carlo simulation: a versatile tool for quantitative analysis of multilayered structures. *IOP Conf. Ser. Mater. Sci. Eng.* **2016**, *109*, 012014.

88. Ortel, E.; Hertwig, A.; Berger, D.; Esposito, P.; Rossi, A.M.; Kraehnert, R.; Hodoroaba, V.-D. New Approach on Quantification of Porosity of Thin Films via Electron-Excited X-ray Spectra. *Anal. Chem.* **2016**, *88*.

89. Eggert, F. EDX-spectra simulation in electron probe microanalysis. Optimization of excitation conditions and detection limits. *Microchim. Acta* **2006**, *155*, 129–136.

90. Armigliato, A. Thin film X-ray microanalysis with the analytical electron microscope. *J. Anal. At. Spectrom.* **1999**, *14*.

91. Christien, F.; Pierson, J.F.; Hassini, A.; Capon, F.; Le Gall, R.; Brousse, T. EPMA-EDS surface measurements of interdiffusion coefficients between miscible metals in thin films. *Appl. Surf. Sci.* **2010**, *256*.

92. Pascual, R.; Cruz, L.R.; Ferreira, C.L.; Gomes, D.T. Thin film thickness measurement using the energy-dispersive spectroscopy technique in a scanning electron microscope. *Thin Solid Films* **1990**, *185*, 279–286.

93. Waldo, R.A.; Militello, M.C.; Gaarenstroom, S.W. Quantitative thin-film analysis with an energy-dispersive x-ray detector. *Surf. Interface Anal.* **1993**, *20*.

94. Gauvin, R. Quantitative X-ray microanalysis of heterogeneous materials using Monte Carlo simulations. *Microchim. Acta* **2006**, *155*.

95. Sokolov, S.A.; Kelm, E.A.; Milovanov, R.A.; Abdullaev, D.A.; Sidorov, L.N. Non-destructive determination of thickness of the dielectric layers using

EDX. In Proceedings of the Proceedings of SPIE - The International Society for Optical Engineering; 2016; Vol. 10224.

96. Stenberg, G.; Boman, M. Thickness measurement of light elemental films. *Diam. Relat. Mater.* **1996**, *5*, 1444–1449.

97. Willich, P.; Obertop, D. Composition and thickness of submicron metal coatings and multilayers on Si determined by EPMA. *Surf. Interface Anal.* **1988**, *13*, 20–24.

98. Hunger, H. -J. -J; Baumann, W.; Schulze, S. A new method for determining the thickness and composition of thin layers by electron probe microanalysis. *Cryst. Res. Technol.* **1985**, *20*, 1427–1433.

99. Ares, J.R.; Pascual, A.; Ferrer, I.J.; Sánchez, C. A methodology to reduce error sources in the determination of thin film chemical composition by EDAX. *Thin Solid Films* **2004**, *450*.

100. Sempf, K.; Herrmann, M.; Bauer, F. First results in thin film analysis based on a new EDS software to determine composition and/or thickness of thin layers on substrates. In Proceedings of the EMC 2008 14th European Microscopy Congress 1–5 September 2008, Aachen, Germany; Springer, 2008; pp. 751–752.

101. Hodoroaba, V.-D.; Kim, K.J.; Unger, W.E.S. Energy dispersive electron probe microanalysis (ED-EPMA) of elemental composition and thickness of Fe-Ni alloy films. *Surf. Interface Anal.* **2012**, *44*.

102. Criss, J.W.; Birks, L.S. Calculation Methods for Fluorescent X-Ray Spectrometry: Empirical Coefficients vs. Fundamental Parameters. *Anal. Chem.* **1968**, *40*, 1080–1086.

103. Kataoka, Y. Standardless x-ray fluorescence spectrometry (Fundamental Parameter Method using Sensitivity Library). *Rigaku J.* **1989**, *6*, 33–40.

104. Thomsen, V. Basic Fundamental Parameters in X-Ray Fluorescence. *Spectroscopy* **2007**, *22*, 46–50.

105. Han, X.Y.; Zhuo, S.J.; Shen, R.X.; Wang, P.L.; Ji, A. Comparison of the quantitative results corrected by fundamental parameter method and difference calibration specimens in X-ray fluorescence spectrometry. *J. Quant. Spectrosc. Radiat. Transf.* **2006**, *97*, 68–74.

106. Pessanha, S.; Fonseca, C.; Santos, J.P.; Carvalho, M.L.; Dias, A.A. Comparison of standard-based and standardless methods of quantification used in X-ray fluorescence analysis: Application to the exoskeleton of clams. *X-Ray Spectrom.* **2018**, *47*, 108–115.

107. Nygård, K.; Hämäläinen, K.; Manninen, S.; Jalas, P.; Ruottinen, J.P. Quantitative thickness determination using x-ray fluorescence: Application to multiple layers. *X-Ray Spectrom.* **2004**, *33*, 354–359.

108. Vrielink, J.A.M.; Tiggelaar, R.M.; Gardeniers, J.G.E.; Lefferts, L. Applicability of X-ray fluorescence spectroscopy as method to determine thickness and composition of stacks of metal thin films: A comparison with imaging and profilometry. *Thin Solid Films* **2012**, *520*, 1740–1744.

109. Elam, W.T.T.; Shen, R.B.; Scruggs, B.; Nicolosi, J. Accuracy of Standardless FP Analysis of Bulk and Thin Film Samples Using a New Atomic Database. *Adv. X-ray Anal.* **2004**, *47*, 104–109.

110. Ager, F.J.; Ferretti, M.; Grilli, M.L.; Juanes, D.; Ortega-Feliu, I.; Respaldiza, M.A.; Roldán, C.; Scrivano, S. Reconsidering the accuracy of X-ray fluorescence and ion beam based methods when used to measure the thickness of ancient gildings. *Spectrochim. Acta - Part B At. Spectrosc.* **2017**, *135*, 42–47.

111. NIST X-Ray Form Factor, Attenuation, and Scattering Tables Available online: https://www.nist.gov/pml/x-ray-form-factor-attenuation-and-scattering-tables.

112. NIST X-Ray Mass Attenuation Coefficients Available online: https://www.nist.gov/pml/x-ray-mass-attenuation-coefficients.

113. NIST XCOM: Photon Cross Sections Database Available online: https://www.nist.gov/pml/xcom-photon-cross-sections-database.

114. Innocenti, M.; Giurlani, W.; Passaponti, M.; Luca, D.; Salvietti, E. Electrodeposition and innovative characterization of precious metal alloys for the Galvanic and Jewel industry. *Substantia* **2019**, *3*, 29–37.

115. Greene, J.E. Tracing the 5000-year recorded history of inorganic thin films from ~3000 BC to the early 1900s AD. *Appl. Phys. Rev.* **2014**, *1*, 41302.

116. Hunt, L.B. The early history of gold plating. *Gold Bull.* **1973**, *6*, 16–27.

117. Jacobi, M.H. *Die Galvanoplastik, Oder das Verfahren coharentes Kupfer in Flatten Oder nach sonst gegebenen Formen unmittelbar aus Kupferauflosungen auf galvanischem Wege zu produciren*; Eggers und Co.: St. Petersburg, 1840;

118. Elkington, G.; Elkington, H. Improvements in Coating, Covering, or Plating certain Metals 1840.

119. Abner, B.; Riddell, G.E. Nickel plating by chemical reduction 1947.

120. Antuña-Jiménez, D.; Díaz-Díaz, G.; Blanco-López, M.C.; Lobo-Castañón, M.J.; Miranda-Ordieres, A.J.; Tuñón-Blanco, P. Chapter 1 - Molecularly

Imprinted Electrochemical Sensors: Past, Present, and Future. In *Molecularly Imprinted Sensors*; 2012; pp. 1–34 ISBN 978-0-444-56331-6.

121. Horwitz, C.P.; Suhu, N.Y.; Dailey, G.C. Synthesis, characterization and electropolymerization of ferrocene monomers with aniline and phenol substituents. *J. Electroanal. Chem.* **1992**, *324*, 79–91.

122. Sharma, P.S.; Pietrzyk-Le, A.; D'Souza, F.; Kutner, W. Electrochemically synthesized polymers in molecular imprinting for chemical sensing. *Anal. Bioanal. Chem.* **2012**, *402*, 3177–3204.

123. Yoshida, T.; Zhang, J.; Komatsu, D.; Sawatani, S.; Minoura, H.; Pauporté, T.; Lincot, D.; Oekermann, T.; Schlettwein, D.; Tada, H.; et al. Electrodeposition of inorganic/organic hybrid thin films. *Adv. Funct. Mater.* **2009**, *19*, 17–43.

124. Abbott, A.P.; Dalrymple, I.; Endres, F.; Macfarlane, D.R. Why use Ionic Liquids for Electrodeposition? In *Electrodeposition from Ionic Liquids*; 2008; Vol. 01, pp. 1–13 ISBN 9783527315659.

125. Zhang, Q.; Wang, Q.; Zhang, S.; Lu, X.; Zhang, X. Electrodeposition in Ionic Liquids. *ChemPhysChem* 2016, *17*, 335–351.

126. Armand, M.; Endres, F.; MacFarlane, D.R.; Ohno, H.; Scrosati, B. Ionic-liquid materials for the electrochemical challenges of the future. *Nat. Mater.* 2009, *8*, 621–629.

127. Tench, D.; White, J. Enhanced tensile strength for electrodeposited nickel-copper multilayer composites. *Metall. Trans. A* **1984**, *15*, 2039–2040.

128. Yahalom, J.; Zadok, O. Formation of composition-modulated alloys by electrodeposition. *J. Mater. Sci.* **1987**, *22*, 499–503.

129. Kang, H.S.; Lee, J.Y.; Choi, S.; Kim, H.; Park, J.H.; Son, J.Y.; Kim, B.H.; Noh, S. Do Smart manufacturing: Past research, present findings, and future directions. *Int. J. Precis. Eng. Manuf. Technol.* **2016**, *3*, 111–128.

130. Giurlani, W.; Zangari, G.; Gambinossi, F.; Passaponti, M.; Salvietti, E.; Di Benedetto, F.; Caporali, S.; Innocenti, M. Electroplating for Decorative Applications: Recent Trends in Research and Development. *Coatings* **2018**, *8*, 260.

131. Cavaciocchi, L.; Banchelli, E.; Canelli, V.D.; Innocenti, M. Galvanic baths for obtaining a low-carat gold alloy, and galvanic process that uses said baths 2013.

132. Gross, O.; Eisenbart, M.; Schmitt, L.Y.; Neuber, N.; Ciftci, L.; Klotz, U.E.; Busch, R.; Gallino, I. Development of novel 18-karat, premium-white gold bulk metallic glasses with improved tarnishing resistance. *Mater. Des.* **2018**,

140, 495–504.

133. Pezzato, L.; Magnabosco, G.; Brunelli, K.; Breda, M.; Dabalà, M. Microstructure and Mechanical Properties of a 18Kt 5N Gold Alloy After Different Heat Treatments. *Metallogr. Microstruct. Anal.* **2016**, *5*, 116–123.

134. Jaszczak, E.; Polkowska, Ż.; Narkowicz, S.; Namieśnik, J. Cyanides in the environment—analysis—problems and challenges. *Environ. Sci. Pollut. Res.* **2017**, *24*, 15929–15948.

135. Salles, F.J.; Sato, A.P.S.; Luz, M.S.; Fávaro, D.I.T.; Ferreira, F.J.; da Silva Paganini, W.; Olympio, K.P.K. *The environmental impact of informal and home productive arrangement in the jewelry and fashion jewelry chain on sanitary sewer system*; 2018; Vol. 25;.

136. Marcus, M.I.; Vlad, M.; Mitiu, M.A.; Anghel, A.M.; Marinescu, F.; Laslo, L.; Ilie, M.; Szep, R.; Ghita, G.; Matei, M.; et al. Recovery of galvanic sludge by physicochemical mechanisms. *J. Environ. Prot. Ecol.* **2017**, *18*, 1117–1126.

137. Sulimova, M.A.; Litvinova, T.E. Metallurgical production waste treatment efficiency increase. In Proceedings of the International Multidisciplinary Scientific GeoConference Surveying Geology and Mining Ecology Management, SGEM; 2016; Vol. 2.

138. Sofińska-Chmiel, W.; Kołodyńska, D. Application of ion exchangers for the purification of galvanic wastewater from heavy metals. *Sep. Sci. Technol.* **2018**, *53*, 1097–1106.

139. Puippe, J.C. *QUALITATIVE APPROACH TO PULSE PLATING.*; 1986; ISBN 0936569026.

140. Zanella, C.; Leisner, P. 6th European pulse plating seminar. *Trans. Inst. Met. Finish.* **2014**, *92*.

141. Chandrasekar, M.S.; Pushpavanam, M. Pulse and pulse reverse plating-Conceptual, advantages and applications. *Electrochim. Acta* 2008, *53*, 3313–3322.

142. Sharan, T.T.; Maarit, K. Atomic Layer Deposition of p-Type Semiconducting Thin Films: a Review. *Adv. Mater. Interfaces* **2017**, *4*, 1700300.

143. Bencistà, I.; Di Benedetto, F.; Innocenti, M.; De Luca, A.; Fornaciai, G.; Lavacchi, A.; Montegrossi, G.; Oberhauser, W.; Pardi, L.A.; Romanelli, M.; et al. Phase composition of CuxS thin films: spectroscopic evidence of covellite formation. *Eur. J. Mineral.* **2012**, *24*, 879–884.

144. Innocenti, M.; Forni, F.; Pezzatini, G.; Raiteri, R.; Loglio, F.; Foresti, M.L. Electrochemical behavior of As on silver single crystals and experimental

conditions for InAs growth by ECALE. *J. Electroanal. Chem.* **2001**, *514*, 75–82.

145. Lincot, D. Electrodeposition of semiconductors. *Thin Solid Films* **2005**, *487*, 40–48.

146. Pezzatini, G.; Loglio, F.; Innocenti, M.; Foresti, M.L. Selenium(IV) Electrochemistry on Silver: A Combined Electrochemical Quartz-Crystal Microbalance and Cyclic Voltammetric Investigation. *Collect. Czechoslov. Chem. Commun.* **2003**, *68*, 1579–1595.

147. Innocenti, M.; Bencistà, I.; Di Benedetto, F.; Cinotti, S.; De Luca, A.; Bellandi, S.; Lavacchi, A.; Muniz Miranda, M.; Vizza, F.; Marinelli, F.; et al. Underpotential Deposition of Sn on S-Covered Ag(111). *ECS Trans.* **2013**, *50*, 1–7.

148. Giurlani, W.; Dell'Aquila, V.; Vizza, M.; Calisi, N.; Lavacchi, A.; Irrera, A.; Lo Faro, M.J.; Leonardi, A.A.; Morganti, D.; Innocenti, M. Electrodeposition of Nanoparticles and Continuous Film of CdSe on n-Si (100). *Nanomaterials* **2019**, *9*, 1504.

149. Singh, A.; Chowdhury, D.R.; Paul, A. A kinetic study of ferrocenium cation decomposition utilizing an integrated electrochemical methodology composed of cyclic voltammetry and amperometry. *Analyst* **2014**, *139*, 5747–5754.

150. Bard, A.J.; Faulkner, L.R. *ELECTROCHEMICAL METHODS Fundamentals and Applications*; John Wiley & Sons Inc: Hoboken, 2000; ISBN 0-471-04372-9.

151. Jones, D.A.; Walker, R. *Principles and Prevention of Corrosion: Pearson New International Edition*; Pearson Higher Ed USA: New York City, 1995; ISBN 0-13-359993-0.

152. Canli, S. Thickness Analysis of Thin Films By Energy Dispersive X-Ray Spectroscopy, 2010.

153. Roming AD, Plimpton SJ, Michael JR, Myklebust RL, N. DE *Microbeam Analysis*; 1990;

154. Kyser, D.F.; Murata, K. Quantitative Electron Microprobe Analysis of Thin Films on Substrates. *IBM J. RES. Dev.* **1974**, *92*, 352–363.

155. Moller, A.; Weinbruch, S.; Stadermann, F.J.; Ortner, H.M.; Neubeck, K.; Balogh, A.G.; Hahn, H. Accuracy of film thickness determination in electron-probe microanalysis. *Mikrochim. Acta* **1995**, *119*, 41–47.

156. Procop, M.; Radtke, M.; Krumrey, M.; Hasche, K.; Schädlich, S.; Frank, W.

Electron probe microanalysis (EPMA) measurement of thin-film thickness in the nanometre range. *Anal. Bioanal. Chem.* **2002**, *374*, 631–634.

157. Campos, C.S.; Coleoni, E.A.; Trincavelli, J.C.; Kaschny, J.; Hubbler, R.; Soares, M.R.F.; Vasconcellos, M.A.Z. Metallic thin film thickness determination using electron probe microanalysis. *X-Ray Spectrom.* **2001**, *30*, 253–259.

158. Zhuang, L.; Bao, S.; Wang, R.; Li, S.; Ma, L.; Lv, D. Thin film thickness measurement using electron probe microanalyzer. In Proceedings of the 2009 International Conference on Applied Superconductivity and Electromagnetic Devices; 2009; pp. 142–144.

159. Merlet, C. Thin film quantification by EPMA: Accuracy of analytical procedure. *Microsc. Microanal.* **2006**, *12*.

160. August, H.; Wernisch, J. A Method for Determining the Mass Thickness of Thin Films Using Electron Probe Microanalysis. *Scanning* **1987**, *9*.

161. Shang, Y.; Guo, Y.; Liu, Z.; Xu, L. An EPMA software for determination of thin metal film thickness and it's application. *Jinshu Xuebao/Acta Metall. Sin.* **1997**, *33*.

162. Watanabe, M.; Horita, Z.; Nemoto, M. Absorption correction and thickness determination using the zeta factor in quantitative X-ray microanalysis. *Ultramicroscopy* **1996**, *65*, 187–198.

163. Bishop, H.E.; Poole, D.M. A simple method of thin film analysis in the electron probe microanalyser. *J. Phys. D. Appl. Phys.* **1973**, *6*, 1142–1158.

164. Colby, J.W. Quantitative Microprobe Analysis of Thin Insulating Films. *Adv. X-ray Anal.* **1967**, *11*, 287–305.

165. HUNGER, H.J. Thin Film Analysis by X-Ray Microanalysis Using Gaussian f (p z) Curves. *Scanning* **1988**, *10*, 65–72.

166. STRATAGem - SAMx Available online: http://www.samx.com/index.html.en.

167. Kühn, J.; Hodoroaba, V.-D.; Linke, S.; Moritz, W.; Unger, W.E.S. Characterization of Pd-Ni-Co alloy thin films by ED-EPMA with application of the STRATAGEM software. *Surf. Interface Anal.* **2012**, *44*.

168. Dumelié, N.; Benhayoune, H.; Balossier, G. *TF_Quantif: A quantification procedure for electron probe microanalysis of thin films on heterogeneous substrates*; 2007; ISBN 9781600214554.

169. Small World Available online: http://www.small-world.net/efs.htm.

170. Batanova, V.G.; Sobolev, A. V.; Kuzmin, D. V. Trace element analysis of olivine: High precision analytical method for JEOL JXA-8230 electron probe microanalyser. *Chem. Geol.* **2015**, *419*, 149–157.

171. ThinFilmID - Oxford Instruments Available online: http://www.oxford-instruments.cn/OxfordInstruments/media/nanoanalysis/brochures and thumbs/ThinFilmID_Brochure.pdf.

172. LayerProbe - Oxford Instruments Available online: https://www.oxford-instruments.com/products/microanalysis/solutions/layerprobe.

173. pyPENELOPE Available online: http://pypenelope.sourceforge.net/.

174. Llovet, X.; Salvat, F. PENEPMA: A Monte Carlo Program for the Simulation of X-Ray Emission in Electron Probe Microanalysis. *Microsc. Microanal.* **2017**, *23*, 634–646.

175. Electron Beam Scattering Modeling Available online: http://montecarlomodeling.mcgill.ca/.

176. Gauvin, R.; Lifshin, E.; Demers, H.; Horny, P.; Campbell, H. Win X-ray: A new Monte Carlo program that computes X-ray spectra obtained with a scanning electron microscope. *Microsc. Microanal.* **2006**, *12*, 49–64.

177. Gauvin, R.; Michaud, P. MC X-Ray, a new monte carlo program for quantitative X-ray microanalysis of real materials. *Microsc. Microanal.* **2009**, *15*, 488–489.

178. CASINO Available online: https://www.gel.usherbrooke.ca/casino/index.html.

179. Demers, H.; Poirier-Demers, N.; Couture, A.R.; Joly, D.; Guilmain, M.; De Jonge, N.; Drouin, D. Three-dimensional electron microscopy simulation with the CASINO Monte Carlo software. *Scanning* **2011**, *33*, 135–146.

180. Hovington, P.; Drouin, D.; Gauvin, R. CASINO: A new Monte Carlo code in C language for electron beam interaction - Part I: Description of the program. *Scanning* **1997**, *19*, 1–14.

181. Drouin, D.; Couture, A.R.; Joly, D.; Tastet, X.; Aimez, V.; Gauvin, R. CASINO V2.42—A Fast and Easy-to-use Modeling Tool for Scanning Electron Microscopy and Microanalysis Users. *Scanning* **2007**, *29*, 92–101.

182. CalcZAF Available online: http://www.probesoftware.com/Technical.html.

183. Armstrong, J.T.; Donovan, J.; Carpenter, P. CALCZAF, TRYZAF and CITZAF: The Use of Multi-Correction-Algorithm Programs for Estimating Uncertainties and Improving Quantitative X-ray Analysis of Difficult Specimens. *Microsc. Microanal.* **2013**, *19*, 812–813.

184. Ritchie, N.W.M. NIST DTSA-II Available online: http://www.cstl.nist.gov/div837/837.02/epq/dtsa2/.

185. Ritchie, N.W. m. M. Spectrum Simulation in DTSA-II. *Microsc. Microanal.* **2009**, *15*, 454–468.

186. Ritchie, N.W.M. Efficient Simulation of Secondary Fluorescence Via NIST DTSA-II Monte Carlo. *Microsc. Microanal.* **2017**, *23*, 618–633.

187. Salvat, F.; Fernández-Varea, J.M.; Sempau, J. *PENELOPE - 2006 : A Code System for Monte Carlo Simulation of Electron and Photon Transport*; OECD/NEA Data Bank, 2006; ISBN 9264023011.

188. XRMC Available online: https://github.com/golosio/xrmc/wiki.

189. XMI-MSIM Available online: https://github.com/tschoonj/xmimsim/wiki.

190. Xraylib Available online: https://github.com/tschoonj/xraylib/wiki.

191. Schoonjans, T.; Brunetti, A.; Golosio, B.; Sanchez Del Rio, M.; Solé, V.A.; Ferrero, C.; Vincze, L. The xraylib library for X-ray-matter interactions. Recent developments. *Spectrochim. Acta - Part B At. Spectrosc.* **2011**, *66*, 776–784.

192. Golosio, B.; Schoonjans, T.; Brunetti, A.; Oliva, P.; Masala, G.L. Monte Carlo simulation of X-ray imaging and spectroscopy experiments using quadric geometry and variance reduction techniques. *Comput. Phys. Commun.* **2014**, *185*, 1044–1052.

193. Giurlani, W.; Innocenti, M.; Lavacchi, A. X-ray Microanalysis of Precious Metal Thin Films: Thickness and Composition Determination. *Coatings* **2018**, *8*, 84.

194. Goldstein, J.I.; Newbury, D.E.; Michael, J.R.; Ritchie, N.W.M.; Scott, J.H.J.; Joy, D.C. *Scanning Electron Microscopy and X-Ray Microanalysis*; Springer Publishing: New York City, 2018; ISBN 978-1-4939-6674-5.

195. Wang, D.; Sun, A. Quantitative Determination of Low Contents of Manganese in Steels by EPMA. *Microsc. Microanal.* **2019**, 625–629.

196. Kenny, K.; Sandercock, M.; Webster, J. Case report: identification of elemental mercury. *J. Can. Soc. Forensic Sci.* **2019**, *52*, 122–128.

197. EDAX Genesis Available online: http://www.edax.com/support/software-licensing.

198. Pathfinder Available online: https://www.thermofisher.com/order/catalog/product/IQLAADGABKFAQOMBJE (accessed on Dec 20, 2018).

199. ImageJ Available online: https://imagej.nih.gov/ij/.

200. Schiavon, N.; de Palmas, A.; Bulla, C.; Piga, G.; Brunetti, A. An Energy-Dispersive X-Ray Fluorescence Spectrometry and Monte Carlo simulation study of Iron-Age Nuragic small bronzes ("Navicelle") from Sardinia, Italy. *Spectrochim. Acta - Part B At. Spectrosc.* **2016**, *123*, 42–46.

201. Bottaini, C.E.; Brunetti, A.; Montero-Ruiz, I.; Valera, A.; Candeias, A.; Mirão, J. Use of Monte Carlo Simulation as a Tool for the Nondestructive Energy Dispersive X-ray Fluorescence (ED-XRF) Spectroscopy Analysis of Archaeological Copper-Based Artifacts from the Chalcolithic Site of Perdigões, Southern Portugal. *Appl. Spectrosc.* **2018**, *72*, 17–27.

202. West, M.; Ellis, A.T.; Streli, C.; Vanhoof, C.; Wobrauschek, P. 2017 atomic spectrometry update-a review of advances in X-ray fluorescence spectrometry and its special applications. *J. Anal. At. Spectrom.* **2017**, *32*, 1629–1649.

203. Brunetti, A.; Fabian, J.; La Torre, C.W.; Schiavon, N. A combined XRF/Monte Carlo simulation study of multilayered Peruvian metal artifacts from the tomb of the Priestess of Chornancap. *Appl. Phys. A Mater. Sci. Process.* **2016**, *122*.

204. Barrea, R.A.; Bengió, S.; Derosa, P.A.; Mainardi, R.T. Absolute mass thickness determination of thin samples by X-ray fluorescence analysis. *Nucl. Instruments Methods Phys. Res. Sect. B Beam Interact. with Mater. Atoms* **1998**, *143*, 561–568.

205. Vincze, L.; Janssens, K.; Adams, F.; Jones, K.W. A general Monte Carlo simulation of energy-dispersive X-ray fluorescence spectrometers-I. Unpolarized radiation, homogeneous samples. *Spectrochim. Acta Part B At. Spectrosc.* **1993**, *48*, 553–573.

206. Vincze, L.; Janssens, K.; Adams, F.; Rivers, M.L.; Jones, K.W. A general Monte Carlo simulation of ED-XRF spectrometers. II: Polarized monochromatic radiation, homogeneous samples. *Spectrochim. Acta Part B At. Spectrosc.* **1995**, *50*, 127–147.

207. Vincze, L.; Janssens, K.; Adams, F.; Jones, K.W. A general Monte Carlo simulation of energy-dispersive X-ray fluorescence spectrometers. Part 3. Polarized polychromatic radiation, homogeneous samples. *Spectrochim. Acta Part B At. Spectrosc.* **1995**, *50*, 1481–1500.

208. Vincze, L.; Janssens, K.; Vekemans, B.; Adams, F. Monte Carlo simulation of X-ray fluorescence spectra: Part 4. Photon scattering at high X-ray energies. *Spectrochim. Acta Part B At. Spectrosc.* **1999**, *54*, 1711–1722.

209. Schoonjans, T.; Vincze, L.; Solé, V.A.; Sanchez Del Rio, M.; Brondeel, P.;

Silversmit, G.; Appel, K.; Ferrero, C. A general Monte Carlo simulation of energy dispersive X-ray fluorescence spectrometers - Part 5: Polarized radiation, stratified samples, cascade effects, M-lines. *Spectrochim. Acta - Part B At. Spectrosc.* **2012**, *70*, 10–23.

210. Schoonjans, T.; Solé, V.A.; Vincze, L.; Sanchez Del Rio, M.; Appel, K.; Ferrero, C. A general Monte Carlo simulation of energy-dispersive X-ray fluorescence spectrometers - Part 6. Quantification through iterative simulations. *Spectrochim. Acta - Part B At. Spectrosc.* **2013**, *82*, 36–41.

211. Watanabe, Y.; Kubozoe, T.; Mukoyama, T. Analytical functions for fitting K X-ray doublet peaks from Si(Li) detectors. *Nucl. Inst. Methods Phys. Res. B* **1986**, *17*, 81–85.

212. McNelles, L.A.; Campbell, J.L. Analytic approximations to peak shapes produced by Ge(Li) and Si(Li) spectrometers. *Nucl. Instruments Methods* **1975**, *127*, 73–81.

213. Van Espen, P.; Lemberge, P. ED-XRF Spectrum Evaluation and Quantitative Analysis Using Multivariate and Nonlinear Techniques. *Adv. X-ray Anal.* **2000**, *43*, 560–569.

214. Kikongi, P.; Salvas, J.; Gosselin, R. Curve-fitting regression: improving light element quantification with XRF. *X-Ray Spectrom.* **2017**, *46*, 347–355.

215. Oberg, E.; Jones, F.; Horton, H.; Ryffel, H.; McCauley, C. *Machinery's Handbook*; 30th ed.; Industrial Press, Inc.: New York, NY, USA, 2016; ISBN 9780831130923.

216. Fan, Q. Simulation of relationships between substrate XRF intensities and film thicknesses. *X-Ray Spectrom.* **1993**, *22*, 11–12.

217. Murata, T. Bismuth solubility through binding by various organic compounds and naturally occurring soil organic matter. *J. Environ. Sci. Heal. Part A* **2010**, *45*, 746–753.

218. Stavila, V.; Davidovich, R.L.; Gulea, A.; Whitmire, K.H. Bismuth(III) complexes with aminopolycarboxylate and polyaminopolycarboxylate ligands: Chemistry and structure. *Coord. Chem. Rev.* **2006**, *250*, 2782–2810.

219. Forni, F.; Innocenti, M.; Pezzatini, G.; Foresti, M.. Electrochemical aspects of CdTe growth on the face (111) of silver by ECALE. *Electrochim. Acta* **2000**, *45*, 3225–3231.

220. Foresti, M.L.; Capolupo, F.; Innocenti, M.; Loglio, F. Visual Detection of Crystallographic Orientations of Face-Centered Cubic Single Crystals. *Cryst. Growth Des.* **2002**, *2*, 73–77.

221. Guidelli, R.; Foresti, M.L.; Innocenti, M. Two-Dimensional Phase Transitions of Chemisorbed Uracil on Ag(111): Modeling of Short- and Long-Time Behavior. *J. Phys. Chem.* **1996**, *100*, 18491–18501.

222. Becucci, L.; Innocenti, M.; Salvietti, E.; Rindi, A.; Pasquini, I.; Vassalli, M.; Foresti, M.L.; Guidelli, R. Potassium ion transport by gramicidin and valinomycin across a Ag(111)-supported tethered bilayer lipid membrane. *Electrochim. Acta* **2008**, *53*, 6372–6379.

223. Innocenti, M.; Loglio, F.; Pigani, L.; Seeber, R.; Terzi, F.; Udisti, R. In situ atomic force microscopy in the study of electrogeneration of polybithiophene on Pt electrode. *Electrochim. Acta* **2005**, *50*, 1497–1503.

224. CasaXPS Available online: http://www.casaxps.com/.

225. Shirley, D.A. High-resolution x-ray photoemission spectrum of the valence bands of gold. *Phys. Rev. B* **1972**, *5*, 4709–4714.

226. Susi, T.; Pichler, T.; Ayala, P. X-ray photoelectron spectroscopy of graphitic carbon nanomaterials doped with heteroatoms. *Beilstein J. Nanotechnol.* **2015**, *6*, 177–192.

227. He, B.; Ghosh, G.; Chung, Y.W.; Wang, Q. Effect of melting and microstructure on the microscale friction of silver-bismuth alloys. *Tribol. Lett.* **2010**, *38*, 275–282.

228. Taylor, M.R.; Fidler, R.S.; Smith, R.W. Broken lamellar eutectic growth; Structure of the silver-bismuth eutectic. *J. Cryst. Growth* **1968**, *3–4*, 666–673.

229. Nathans, M.W.; Leider, M. Studies on bismuth alloys. I. Liquidus curves of the bismuth-copper, bismuth-silver, and bismuth-gold systems. *J. Phys. Chem.* **1962**, *66*, 2012–2015.

230. Giurlani, W.; Giaccherini, A.; Calisi, N.; Zangari, G.; Salvietti, E.; Passaponti, M.; Caporali, S.; Innocenti, M. Investigations on the Electrochemical Atomic Layer Growth of Bi2Se3 and the Surface Limited Deposition of Bismuth at the Silver Electrode. *Materials (Basel).* **2018**, *11*, 1426.

231. NIST X-ray Photoelectron Spectroscopy Database Available online: https://srdata.nist.gov/xps.

232. Dharmadhikari, V.S.; Sainkar, S.R.; Badrinarayan, S.; Goswami, A. Characterisation of thin films of bismuth oxide by X-ray photoelectron spectroscopy. *J. Electron Spectros. Relat. Phenomena* **1982**, *25*, 181–189.

233. Hatchett, D.W.; Gao, X.; Catron, S.W.; White, H.S. Electrochemistry of sulfur adlayers on Ag(111). Evidence for a concentration- and potential-dependent surface-phase transition. *J. Phys. Chem.* **1996**, *100*, 331–338.

234. Nascimento, V..; de Carvalho, V..; Paniago, R.; Soares, E..; Ladeira, L..; Pfannes, H.. XPS and EELS study of the bismuth selenide. *J. Electron Spectros. Relat. Phenomena* **1999**, *104*, 99–107.

235. Ambrosi, A.; Sofer, Z.; Luxa, J.; Pumera, M. Exfoliation of Layered Topological Insulators Bi2Se3 and Bi2Te3 via Electrochemistry. *ACS Nano* **2016**, *10*, 11442–11448.

236. Irfan, B.; Chatterjee, R. Characterization and synthesis of Bi2Se3 topological insulator thin film using thermal evaporation. *Adv. Mater. Lett.* **2016**, *7*, 100–150.

237. Moulder, J.F.; Stickle, W.F.; Sobol, P.E.; Bomben, K.D. Handbook of Photoelectron Spectroscopy. *Phys. Electron. Inc., Eden Prairie, Minnesota* **1992**.

238. Wyckoff, R.W.G. *Crystal Structures*; Second edi.; Interscience Publishers: New York, 1963; Vol. 1;.

239. Yaginuma, S.; Nagaoka, K.; Nagao, T.; Bihlmayer, G.; M. Koroteev, Y.; V. Chulkov, E.; Nakayama, T. Electronic Structure of Ultrathin Bismuth Films with A7 and Black-Phosphorus-like Structures. *J. Phys. Soc. Japan* **2008**, *77*, 014701.

240. Giurlani, W.; Berretti, E.; Innocenti, M.; Lavacchi, A. Coating Thickness Determination Using X-ray Fluorescence Spectroscopy: Monte Carlo Simulations as an Alternative to the Use of Standards. *Coatings* **2019**, *9*, 79.

241. Baghban, M.A.; Gallo, K. Impact of longitudinal fields on second harmonic generation in lithium niobate nanopillars. *APL Photonics* **2016**, *1*, 061302.

242. Zhao, G.; Wang, L.; Yang, S.; Li, H.; Wei, H.; Han, D.; Wang, Z. Anisotropic structural and optical properties of semi-polar (11–22) GaN grown on m-plane sapphire using double AlN buffer layers. *Sci. Rep.* **2016**, *6*, 20787.

243. Ohno, S.; Adachi, S.; Kaji, R.; Muto, S.; Sasakura, H. Optical anisotropy and photoluminescence polarization in single InAlAs quantum dots. *Appl. Phys. Lett.* **2011**, *98*, 161912.

244. Park, Y.; Chan, C.C.S.; Nuttall, L.; Puchtler, T.J.; Taylor, R.A.; Kim, N.; Jo, Y.; Im, H. Linearly polarized photoluminescence of InGaN quantum disks embedded in GaN nanorods. *Sci. Rep.* **2018**, *8*, 8124.

245. Kakko, J.-P.; Matikainen, A.; Anttu, N.; Kujala, S.; Mäntynen, H.; Khayrudinov, V.; Autere, A.; Sun, Z.; Lipsanen, H. Measurement of Nanowire Optical Modes Using Cross-Polarization Microscopy. *Sci. Rep.* **2017**, *7*, 17790.

246. Feng, L.; Liu, Z.; Lomakin, V.; Fainman, Y. Form birefringence metal and its

plasmonic anisotropy. *Appl. Phys. Lett.* **2010**, *96*, 041112.

247. Richter, I.; Sun, P.-C.; Xu, F.; Fainman, Y. Design considerations of form birefringent microstructures. *Appl. Opt.* **1995**, *34*, 2421.

248. Tyan, R.-C.; Salvekar, A.A.; Chou, H.-P.; Cheng, C.-C.; Scherer, A.; Sun, P.-C.; Xu, F.; Fainman, Y. Design, fabrication, and characterization of form-birefringent multilayer polarizing beam splitter. *J. Opt. Soc. Am. A* **1997**, *14*, 1627.